

OPTICAL SPECTROSCOPY OF
GRAPHENE AND GOLD NANOSTRUCTURES

Von der Fakultät für Mathematik, Physik und Informatik
der Universität Bayreuth zur Erlangung des Grades
eines Doktors der Naturwissenschaften (Dr. rer. nat.)
genehmigte Abhandlung

vorgelegt von

DANIELA CHRISTIANE WOLF

geb. Ullrich

aus Nürtingen

Universität Bayreuth

2016

PRÜFUNGSAUSSCHUSS:

Prof. Dr. Markus Lippitz (Erstgutachter)

Prof. Dr. Jürgen Köhler (Zweitgutachter)

Prof. Dr. Stephan Kümmel (Prüfungsvorsitz)

Apl. Prof. Dr. Lothar Kador

TAG DER EINREICHUNG: 02. März 2016

TAG DES KOLLOQUIUMS: 29. Juni 2016

ABSTRACT

This thesis covers two prominent material systems in the still emerging field of nano-optics. On the one hand, we study the optical properties of graphene, from a general point of view as well as under symmetry breaking induced by strain. On the other hand, we make use of the plasmonic properties of gold nanostructures and investigate the generated nonlinear signals on a local scale. With both systems being promising candidates for nanophotonic applications, a spectroscopic investigation is of utmost importance to gain a deeper understanding of the interaction of these systems with light.

Graphene's band structure exhibits a saddle point, which gives rise to a unique optical response in the visible and ultraviolet wavelength regime. Assuming a discrete excitonic state in the vicinity of the saddle point, a classical Fano model based on interference between a continuum of states and the discrete state can be applied. It reproduces very well both lineshape and position of the measured spectrum even down to infrared wavelengths. After a discussion of the general optical properties, we study the influence of strain on graphene. Unlike most other modifications, strain breaks the symmetry of the lattice and the band structure and is hence predicted to induce profound changes in the optical spectrum. In addition to a study of the response considering different substrate materials, we introduce Raman spectroscopy as a reference measurement to reliably quantify the amount of strain applied to the graphene flakes. However, our thorough investigations indicate that the Fano resonance in graphene is very robust towards strain as we do not observe strain-induced changes in the optical spectrum.

The second part of this thesis addresses the nonlinear optical properties of gold nanostructures. Whereas most investigations in nonlinear plasmonics focus on the enhancement of nonlinear processes and their spectral characteristics, we consider the spatial origin of the signals which is still under debate. Due to the coherence of the higher harmonics generation process, the third-harmonic emission from different emitting centers of a nanostructure interferes. In analogy to classical diffraction experiments, the interference pattern observed in the Fourier plane is very sensitive towards parameters such as separation and relative phase of the emitting spots. We use this method to accurately determine the high fields

inside the nanostructures as the source of third-harmonic generation. Moreover, we show that the emission properties of an elongated plasmonic structure can be switched between a configuration with one emission spot in the center and a configuration with two spatially separated spots by slightly varying the excitation wavelength. Due to the third power dependence of the third-harmonic generation process, the near-fields generated in the vicinity of the particle switch accordingly. While assemblies of nanoparticles are commonly used to shape fields, we show that the local field can also be sculptured around a single, elongated nanostructure by taking higher-order plasmonic modes into account. This approach opens up a new direction for field shaping on the nanoscale.

ZUSAMMENFASSUNG

Diese Dissertation befasst sich mit zwei bedeutenden Materialsystemen auf dem Gebiet der Nano-Optik. Auf der einen Seite untersuchen wir die optischen Eigenschaften von Graphen, sowohl unter allgemeinen Gesichtspunkten als auch bei von Dehnspannung hervorgerufenem Symmetriebruch. Andererseits nutzen wir die plasmonischen Eigenschaften von Gold-Nanostrukturen und analysieren die erzeugten nichtlinearen Signale auf einer lokalen Skala. Beide Systeme sind vielversprechende Kandidaten für nanophotonische Anwendungen, daher ist es von großer Bedeutung, mithilfe von spektroskopischen Untersuchungen ein tieferes Verständnis über ihre Wechselwirkung mit Licht zu erlangen.

Graphens Bandstruktur weist einen Sattelpunkt auf, der zu einem charakteristischen optischen Spektrum im sichtbaren und ultravioletten Wellenlängenbereich führt. Wird ein diskreter exzitonischer Zustand in der Nähe des Sattelpunktes angenommen, kann ein klassisches Fano-Modell angewendet werden, welches die Kopplung zwischen einem Kontinuum von Zuständen und dem diskreten Zustand beschreibt. Das Modell führt im Hinblick auf Linienform und Position zu einer guten Übereinstimmung mit dem gemessenen Spektrum bis in den infraroten Bereich. Nach einer Diskussion der allgemeinen optischen Eigenschaften untersuchen wir den Einfluss von Dehnspannung auf Graphen. Im Gegensatz zu den meisten Effekten wird hier die Symmetrie des Gitters und der Bandstruktur gebrochen, was zu tiefgreifenden Änderungen im optischen Spektrum führen sollte. Neben einer Analyse des Spektrums bei Verwendung unterschiedlicher Substratmaterialien stellen wir Raman-Spektroskopie vor, mit welcher die in den verschiedenen Messgeometrien angelegte Dehnspannung quantifiziert werden kann. Unsere Untersuchungen zeigen jedoch, dass die Fanoresonanz in Graphen sehr stabil auch gegenüber Dehnspannung ist, da keine Änderungen im optischen Spektrum beobachtet werden.

Der zweite Teil dieser Dissertation beschäftigt sich mit den nichtlinearen optischen Eigenschaften von Gold-Nanostrukturen. Während die meisten Studien in nichtlinearer Plasmonik sich auf die Verstärkung von nichtlinearen Prozessen und deren spektrale Charakteristik konzentrieren, betrachten wir den räumlichen Ursprung der Signale, der Gegenstand aktueller Diskussion ist. Aufgrund der Kohärenz des nichtlinearen Prozesses interferiert die Emission der

dritten Harmonischen von verschiedenen, räumlich getrennten Emissionspunkten der Nanostruktur. In Analogie zu klassischen Beugungsexperimenten ist das im Fernfeld beobachtete Interferenzmuster sehr sensibel auf Parameter wie den Abstand und die relative Phase der Emissionsspot. Wir nutzen diese Methode um mit großer Genauigkeit zu bestimmen, dass die hohen Felder innerhalb der Nanostrukturen die Quelle der dritten Harmonischen sind. Zudem zeigen wir, dass durch Variieren der Anregungswellenlänge die Emission einer ausgedehnten plasmonischen Struktur zwischen einer Konfiguration mit einem zentralen Emissionspunkt und einer Konfiguration mit zwei räumlich getrennten Emissionspunkten geschaltet werden kann. Durch die Potenzabhängigkeit der dritten Harmonischen verschieben sich die erzeugten Nahfelder in der Umgebung des Partikels auf gleiche Weise. Während üblicherweise räumliche Anordnungen von Nanopartikeln ausgenutzt werden um Felder zu formen, zeigen wir, dass auch das lokale Feld um eine einzelne, ausgedehnte Nanostruktur durch Berücksichtigung von Plasmonmoden höherer Ordnung kontrolliert werden kann. Dieser Ansatz eröffnet neue Möglichkeiten für das Formen von Feldern auf der Nanoskala.

PUBLICATIONS

In scientific journals:

D. Wolf, T. Schumacher, and M. Lippitz, *Shaping the nonlinear near field*, Nature Communications 7:10361 (2016)

T. Schumacher, M. Brandstetter, **D. Wolf**, K. Kratzer, M. Hentschel, H. Giessen, and M. Lippitz, *The optimal antenna for nonlinear spectroscopy of weakly and strongly scattering nanoobjects*, Applied Physics B: Lasers and Optics, 122:91 (2016)

C. Dicken, T. Schumacher, **D. Wolf**, K. Lindfors, H. Giessen, and M. Lippitz, *Homodyne detection of small changes of the optical constants of lossy metal nanoparticles*, in preparation (2016)

C. Schörner, **D. Wolf**, T. Schumacher, M. Lippitz, Peter Bauer, and M. Thelakkat, *Nondestructive probing of a photochromic dithienylethene coupled to plasmonic nanostructures*, in preparation (2016)

Book chapters:

D. Wolf, D.-H. Chae, T. Utikal, P. Herlinger, J. Smet, H. Giessen, and M. Lippitz, *Spectroscopy of graphene at the saddle point*, in: Optical properties of graphene, edited by R. Binder, World Scientific

Contributions at international conferences (own):

Talk

D. Wolf, T. Schumacher, and M. Lippitz, *Shaping the nonlinear near field*, 4th International Workshop on Ultrafast Nanooptics, Bad Dürkheim/Germany (2015)

D. Wolf, T. Schumacher, and M. Lippitz, *Local Nonlinear Spectroscopy of Single Gold Nanostructures*, DPG Spring Meeting, Berlin/Germany (2015)

D. Ullrich, P. Herlinger, H. Giessen, J. Smet, and M. Lippitz, *Effects of strain on the excitonic Fano resonance in the optical spectrum of graphene*, DPG Spring Meeting, Regensburg/Germany (2013)

Poster

D. Ullrich, P. Herlinger, D.-H. Chae, T. Utikal, H. Giessen, J. Smet, and M. Lippitz, *Investigation of excitonic Fano resonances in graphene using optical spectroscopy*, Graphene 2012, Brussels/Belgium (2012)

Contributions at international conferences (other):

Talk

C. Dicken, **D. Wolf**, T. Schumacher, K. Lindfors, H. Giessen, and M. Lippitz, *Far-field interferometry of weak plasmonics scatterers*, DPG Spring Meeting, Regensburg/Germany (2016)

C. Dicken, T. Schumacher, **D. Ullrich**, K. Lindfors, H. Giessen, and M. Lippitz, *The Role of the Scattering Phase in Single Particle Spectroscopy*, DPG Spring Meeting, Regensburg/Germany (2013)

T. Schumacher, **D. Ullrich**, M. Hentschel, H. Giessen, and M. Lippitz, *Optical antennas for ultrafast spectroscopy of single CdSe nanoobjects*, DPG Spring Meeting, Regensburg/Germany (2013)

T. Schumacher, **D. Ullrich**, M. Hentschel, H. Giessen, and M. Lippitz, *Optical Nanoantennas for Ultrafast Spectroscopy of Single Nanoobjects*, DPG Spring Meeting, Berlin/Germany (2012)

T. Schumacher, **D. Ullrich**, K. Kratzer, M. Hentschel, H. Giessen, and M. Lippitz, *Optical Nanoantennas for Ultrafast Spectroscopy of Single Nanoparticles*, DPG Spring Meeting, Dresden/Germany (2011)

T. Schumacher, K. Kratzer, **D. Ullrich**, M. Hentschel, H. Giessen, and M. Lippitz, *Nanoantenna-enhanced ultrafast nonlinear spectroscopy of a single plasmonic nanodisc*, CLEO: QELS, Baltimore/USA (2011)

Poster

J. Obermeier, T. Schumacher, **D. Wolf**, and M. Lippitz, *Higher Harmonics Generation in Single Extended Gold Nanostructures*, DPG Spring Meeting, Regensburg/Germany (2016)

J. Koller, T. Schumacher, C. Dicken, **D. Wolf**, A. Köhler, and M. Lippitz, *Coupling of an organic cyanine dye with a plasmonic structure*, DPG Spring Meeting, Berlin/Germany (2015)

M. Berger, **D. Wolf**, T. Schumacher, S. Earl, D. Gomez, and M. Lippitz, *Positioning colloidal nanocrystals next to plasmonic nanostructures using electron-beam lithography*, DPG Spring Meeting, Berlin/Germany (2015)

T. Schumacher, **D. Ullrich**, M. Hentschel, H. Giessen, and M. Lippitz, *Optical Nanoantennas for Nonlinear Spectroscopy of a Single Nanoobject*, Ultrafast Phenomena, Lausanne/Switzerland (2012)

T. Schumacher, **D. Ullrich**, M. Hentschel, H. Giessen, and M. Lippitz, *Nanoantenna-enhanced ultrafast spectroscopy of a single nanoparticle*, SPP1391: Second Summer School, Bad Honnef/Germany (2012)

P. Herlinger, **D. Ullrich**, H. Giessen, J. Smet, and M. Lippitz, *Investigation of excitonic Fano resonances in graphene using optical spectroscopy*, DPG Spring Meeting, Berlin/Germany (2012)

T. Schumacher, **D. Ullrich**, M. Hentschel, H. Giessen, and M. Lippitz, *Optical Nanoantennas for Nonlinear Spectroscopy of a Single Nanoobject*, Ultrafast Phenomena, Lausanne/Switzerland (2012)

T. Schumacher, **D. Ullrich**, M. Hentschel, H. Giessen, and M. Lippitz, *Nanoantenna-enhanced ultrafast spectroscopy of a single nanoparticle*, SPP1391: Second Summer School, Bad Honnef/Germany (2012)

Other contributions:

Annual report 2011 of the Max Planck Institute for Solid State Research:
Excitonic Fano resonance in free-standing graphene

CONTENTS

1	PREFACE AND OUTLINE	1
I	OPTICAL SPECTROSCOPY OF GRAPHENE	5
2	GRAPHENE – A 2D WONDERLAND	7
2.1	Crystal and electronic structure	8
2.2	Optical properties	11
2.3	Sample fabrication and characterization	15
3	SPECTROSCOPY OF GRAPHENE AT THE SADDLE POINT	21
3.1	Van Hove singularities in the band structure	22
3.2	Experimental realization	23
3.3	Saddle point excitons and many-body effects	26
3.4	Interpretation of the spectrum with a classical Fano model	28
3.5	Properties of the excitonic resonance	31
3.6	Derivation of the optical constants from the Fano model	34
4	EFFECT OF STRAIN ON THE OPTICAL PROPERTIES	37
4.1	Uniaxial strain: breaking the symmetry	38
4.2	Experimental realization	40
4.3	Calculation of the optical response of multilayer systems	45
4.4	Visibility and Raman spectrum on various substrates	46
4.5	Quantifying strain with Raman spectroscopy	49
4.6	Effect of uniaxial strain on the excitonic Fano resonance	57
4.7	Conclusions and outlook	66

II	LOCAL NONLINEAR SPECTROSCOPY OF NANOSTRUCTURES	69
5	FUNDAMENTALS OF NONLINEAR NANO-OPTICS	71
5.1	Light-matter interaction: electromagnetic theory	72
5.2	Nonlinear optical processes	76
5.3	Plasmonics	81
6	METHODS	87
6.1	Nanofabrication: electron beam lithography	87
6.2	Experimental realization	90
6.3	Calculation of radiation patterns	92
6.4	Finite element method calculations	96
7	THIRD-HARMONIC GENERATION OF GOLD NANORODS	99
7.1	Nonlinear emission properties of a single particle	100
7.2	Nonlinear plasmonic analogue of Young's double slit	104
7.3	Localizing the spatial origin of THG	109
7.4	Switching the emission properties of a long rod	114
7.5	Nonlinear near-field shaping	119
7.6	Conclusions and outlook	120
8	CONCLUSION AND OUTLOOK	123
	BIBLIOGRAPHY	127
	CURRICULUM VITAE	143
	ACKNOWLEDGEMENTS	145

PREFACE AND OUTLINE

The investigation of the properties of light and especially the interaction of light with matter is one of the traditional branches in classical physics. Despite having been object of study for centuries, optics is still a very lively field of research, bringing forth a plethora of breakthroughs and applications. Prominent examples of milestones in optics are new light sources including lasers and light-emitting diodes, optical fibers, photonic crystals, or solar cells [1, 2].

Toward the end of the last century, novel technologies allowed for the fabrication and observation of nanoscale structures, paving the way for the new field of nanotechnology. Nanostructures exhibit a variety of exceptional properties as they bridge the gap between the bulk and the quantum regime. Amongst many other interesting characteristics, the light-matter interaction on the nanoscale gives rise to outstanding effects. In consequence, plasmonics [3] and metamaterials [4, 5] as examples for nano-optical phenomena have to be added to the list of milestones [2]. Quite recently graphene, a monolayer of carbon atoms [6], and other monolayer crystals [7] became available as novel platform to study the interaction of light with purely two-dimensional systems [8, 9, 10].

In contrast to bulk material, nanostructures offer the possibility to tailor the optical properties by varying parameters such as size or geometry [11, 12]. Additional flexibility is gained by arranging nanoparticles into assemblies and combining different structures into hybrid systems [13, 14]. Sculptured two- and three-dimensional nanoarchitectures give the power to control and manipulate light and its flow at the nanoscale, overcoming the diffraction limit [1]. One of the most prestigious amongst the many prospects in nanophotonics are optical circuitry and computing. Combining nanoscale emitters, waveguiding structures as well as switching and other processing devices on a chip potentially allows for fully integrated light-based communication systems [1].

This thesis aims at a more thorough understanding of the optical properties of two different nanoscopic systems.

First, we consider graphene which, being a two-dimensional material, can be viewed as "nano" in the third dimension. Since its discovery in 2004 [6], many important aspects of graphene and related systems have been studied [15]. However, the analysis of the optical properties still lags behind as most investigations

focus on electronic transport properties. Using optical spectroscopy, one can get further insight into the electronic structure of graphene and gain a deeper understanding of the nature of the excited states. This is particularly interesting in the visible to ultraviolet wavelength regime, where graphene's extraordinary band structure exhibits a saddle point [16]. Besides the fundamental research interest, a detailed investigation of the optical properties is of essential importance on the route towards applications of graphene in optoelectronics, for example in modulators or detectors [17, 18].

Second, we study plasmonic structures which are mostly metal nanoparticles and hence truly "nano". Particle plasmons are collective oscillations of the electrons, manifesting as resonances in the visible wavelength regime. These excitations are associated with strong local fields and have found already a multitude of applications ranging from sensing [19, 20] up to negative index and cloaking materials [21, 22, 23, 24]. While the linear interaction of plasmons with light is quite well understood, questions remain on the nonlinear behavior. Such deviations from the linear interaction with light are observed at high excitation powers and give rise to interesting effects including frequency conversion processes and modulation of the signals [25]. In this context, nanostructures offer new possibilities in nonlinear optics, for example promising nonlinear optical components to be scaled down or allowing for ultrafast response times [26].

Merging graphene and plasmonic nanostructures adds a new playground to the field of nanophotonics. First experiments revealed the great potential of such hybrid systems for optoelectronic devices [27, 28] or sensor applications [29], paving the way towards tunable optical nanocircuits [8, 30, 1].

Due to the fundamentally different nature of the two systems under consideration as well as the related experiments and methods, this thesis is divided into two parts. While the first part covers the optical properties of graphene, the nonlinear emission characteristics of gold nanostructures are studied in the second part.

In chapter 2, we first present a short review of the extraordinary material properties of graphene. After discussing the crystal and resulting electronic structure, we focus on the optical properties. Providing the basis for later studies, we restrict here to the visible and near-infrared wavelength regime. Moreover, an overview of the fabrication and characterization techniques for graphene is given.

Chapter 3 gives an introduction to linear spectroscopy of graphene in the visible and UV wavelength regime. First, the experimental setup is presented. We will then see that graphene's band structure exhibits a saddle point which is associated with an excitonic state. A simple Fano lineshape can fully describe

the characteristic absorbance spectrum in the vicinity of the saddle point, but also down to infrared frequencies. The properties of the excitonic resonance in graphene are discussed and compared to excitons in graphene-related systems. In addition, we show that the optical constants of graphene can be extracted from the Fano fit using the Kramers-Kronig relations.

The influence of strain on the Fano resonance is investigated in chapter 4. Strain causes intriguing effects as it breaks the symmetry in the crystal as well as the band structure. Regarding the experimental methods, we present our reflection setup which includes a path for in-situ Raman measurements and discuss how strain is applied to our samples. Based on the optical constants of graphene, the optical spectrum of graphene on an arbitrary substrate can be calculated with a transfer matrix formalism. After introducing this method, we will study the optical response on different substrates. In our experiments, Raman spectroscopy is used as a reference to quantify the amount of strain on the samples. Finally, we discuss our results on the effect of strain on the optical spectrum of graphene in the ultraviolet regime.

In view of our experiments with plasmonic structures, chapter 5 is dedicated to the fundamentals of nonlinear nano-optics. After a general discussion of light-matter interaction, we focus on some essential aspects regarding nonlinear plasmonics. Here, we provide an overview of nonlinear optical processes before giving a brief introduction to plasmonics.

In chapter 6, we summarize the methods that are relevant for our investigations. The nanostructures are fabricated in a standard electron beam lithography process. With a nonlinear transmission setup in combination with back focal plane imaging, we measure spectra of the nonlinear signals and capture the spatial emission characteristics of individual nanostructures. We discuss a simple method to calculate radiation patterns which is based on the emission properties of a dipole near an interface. A finite element method allows us to simulate the distribution of linear and nonlinear fields around a plasmonic structure.

Chapter 7 presents the essential results of our study of the third-harmonic emission properties of nanostructures. First, we discuss the working principle of our experiments at the example of very small rod structures, which yields first intriguing insights. In analogy to classical diffraction experiments, interference is observed between light from different emitting centers. That way, we build the nonlinear plasmonic analogue of a classical double slit from two spatially separated nanorods. Based on these observations, we exploit higher order plasmonic modes in an elongated structure to switch the emission properties between different configurations. Finally, we show that the generated nonlinear near fields exhibit the same switching behavior.

Part of the work presented in this thesis has been published already. Chapter 3 is based on the results obtained by our coworkers [31] and is published as a chapter covering "Spectroscopy of Graphene at the Saddle Point" in the book "Optical Properties of Graphene" [32]. Chapter 7 closely follows our publication "Shaping the nonlinear near field" [33].

Part I

OPTICAL SPECTROSCOPY OF GRAPHENE

Graphene, a monolayer of carbon atoms arranged in a two-dimensional (2D) lattice, has attracted a lot of research interest in the last years. Being sometimes called the ‘mother’ of all graphitic materials [34], it can be stacked into 3D graphite and rolled into 1D carbon nanotubes or 0D fullerenes. Despite having been studied theoretically for decades [35, 36, 37], graphene – like all strictly 2D materials – was long presumed to be thermodynamically unstable in its free state [38, 39, 40, 41]. Apart from the existence as part of larger 3D structures, it was considered to be a purely academic model system [42]. The discovery of the existence of 2D atomic crystals [7] and especially that of graphene in 2004 [6, 43] hence came as a surprise. It has triggered an overwhelming and still-growing number of theoretical and experimental investigations and was awarded with a Nobel prize in Physics in 2010.

This is certainly due to the fact that graphene is a superlative material in many regards. It is the thinnest and at the same time strongest material ever measured [44] and exhibits a record room temperature thermal conductivity [45]. Most striking, however, are its electronic properties, such as the high carrier mobility and the presence of a quantum Hall effect at room temperature [6, 46]. Besides being of general interest for physicists and material scientists, graphene is a promising candidate for a long list of applications, ranging from electronics and optoelectronics via sensing and energy storage to biomedicine [17, 47, 48].

Most of graphene’s physical properties emerge directly from its unique band structure. In the first sections of this chapter, we will give an overview of the atomic and electronic structure (section 2.1) and the resulting optical properties (section 2.2). The fabrication and characterization techniques used in this thesis are presented in section 2.3.

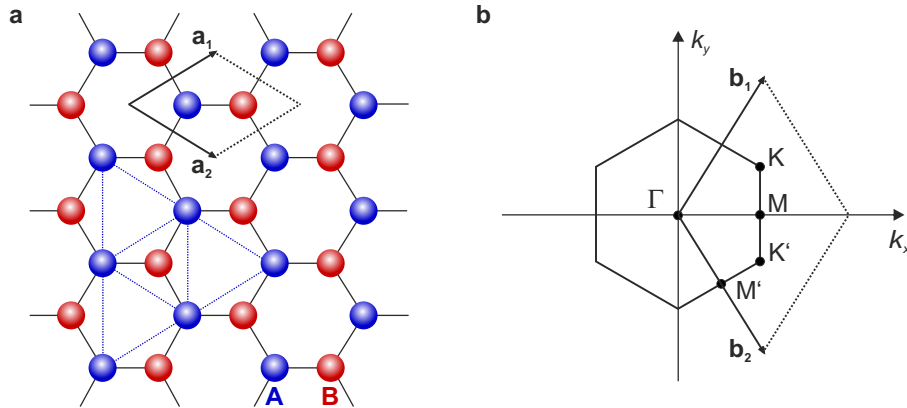


Figure 2.1: **a)** Honeycomb lattice of graphene with the lattice vectors \mathbf{a}_1 , \mathbf{a}_2 . The unit cell contains two carbon atoms, belonging to the two sublattices A and B. Part of triangular sublattice A is indicated by dashed blue lines. **b)** Corresponding Brillouin zone with the reciprocal lattice vectors \mathbf{b}_1 , \mathbf{b}_2 and important points in reciprocal space.

2.1 CRYSTAL AND ELECTRONIC STRUCTURE

The carbon atoms in graphene are arranged in a hexagonal honeycomb lattice shown in figure 2.1a. The structure can be described as two interleaving triangular lattices, i. e. with a basis of two atoms per unit cell [16].

The trigonal planar structure of graphene arises from the sp^2 hybridization which leads to the formation of robust σ bonds with a carbon–carbon separation of $a_0 = 1.42 \text{ \AA}$. The remaining p orbital is oriented perpendicular to the molecular plane and hybridizes covalently with the orbitals of neighboring carbon atoms to form the valence and conduction bands π and π^* , respectively. The π bands are responsible for conduction and hence determine most of graphene’s electronic and optical properties.

The hexagonal symmetry is retained in the Brillouin zone (BZ) as shown in figure 2.1b. Γ , K and M are points of high symmetry in reciprocal space, where Γ is the center point of the BZ. The six so-called Dirac points K are at the corners of the BZ, whereas M denotes a saddle point between two neighboring Dirac points. The two sets K/K' and M/M' correspond to the two sublattices.

The band structure of the π bands of graphene can be calculated with a simple tight-binding model [35, 16]. The Hamiltonian including nearest and next-

nearest neighbor hopping of the electrons (in natural units $\hbar = c = 1$) is given by

$$H = -t \sum_{\langle i,j \rangle, s} (a_{i,s}^\dagger b_{j,s} + \text{h.c.}) - t' \sum_{\langle i,j \rangle, s} (a_{i,s}^\dagger a_{j,s} + b_{i,s}^\dagger b_{j,s} + \text{h.c.}). \quad (2.1)$$

$a_{i,s}$ ($a_{i,s}^\dagger$) annihilates (creates) an electron with spin s ($s = \uparrow, \downarrow$) on sublattice A, the same definition is used for $b_{i,s}$ and $b_{i,s}^\dagger$ in sublattice B. t and t' are the nearest and next-nearest neighbor hopping energies, corresponding to hopping between the sublattices and hopping in the same sublattice. This leads to the energy bands [35, 16]

$$E_{\pm}(\vec{k}) = \pm t \sqrt{3 + f(\vec{k})} - t' f(\vec{k}) \quad (2.2)$$

with

$$f(\vec{k}) = 2 \cos(\sqrt{3} k_y a_0) + 4 \cos\left(\frac{\sqrt{3}}{2} k_y a_0\right) \cos\left(\frac{3}{2} k_x a_0\right). \quad (2.3)$$

Here, the plus sign denotes the antibonding π^* band, the minus sign the binding π band. The symmetry between the π and π^* bands is broken for finite values of the next-nearest neighbor hopping energy t' . Figure 2.2 shows the full band structure of graphene for $t = 2.7$ eV and $t' = -0.2t$. The valence and conduction bands are touching at the Dirac points which coincide with the Fermi energy for undoped graphene. Graphene is hence classified as a semimetal or zero-gap semiconductor. Due to symmetry, neighboring Dirac points K and K' as well as neighboring saddle points M and M' are degenerate.

The dispersion at the K points is obtained by expanding the band structure from equation 2.2 for small \vec{q} relative to the Dirac point [35, 16]:

$$E_{\pm}(\vec{q}) \approx v_F |\vec{q}| + O[(q/k)^2]. \quad (2.4)$$

$v_F = 3ta_0/2$ is the Fermi velocity, which corresponds to an effective speed of light and is on the order of $v_F \simeq 10^6$ m/s. In consequence, the Fermi velocity is a constant independent of the momentum, resulting in a linear dispersion at the Dirac cones. This behavior is similar to relativistic particles and contrasts with the usual case of a quadratic dispersion with $v = q/m = \sqrt{2E/m}$. In the low energy limit, the charge carriers in graphene are described as massless fermions by the relativistic (2+1)-dimensional Dirac equation rather than the Schrödinger equation:

$$E \Psi(\vec{r}) = -i\hbar v_F \vec{\sigma} \cdot \nabla \Psi(\vec{r}) \quad (2.5)$$

with the vector of Pauli matrices $\vec{\sigma} = (\sigma_x, \sigma_y)$ in 2D and the eigenenergies $E = \pm v_F q$. The wave function $\Psi(\vec{r})$ is a two-component spinor where the components correspond to the two sublattices. In analogy to the spin index in quantum electrodynamics (QED), this is interpreted as a pseudospin of the states close to the Dirac point. The massless Dirac fermion characteristic of the charge carriers in graphene manifests in various transport experiments, for example in the minimum conductivity at the charge neutrality point or the anomalous half-integer quantum Hall effect [46]. This makes graphene an ideal and easily accessible platform for studies of QED effects even at room temperature [34].

Another consequence of the linear dispersion at the Dirac point is the ambipolar field effect where the conduction channel can be switched between electrons and holes [6]. When graphene is doped for example by electrostatic gating, the Fermi energy is shifted away from the Dirac point to either higher or lower energies, corresponding to electron and hole conduction, respectively. Doping is a very interesting technique as it allows to continuously tune the charge carrier density. Apart from transport, it also affects the optical properties of graphene, as is described in the following section.

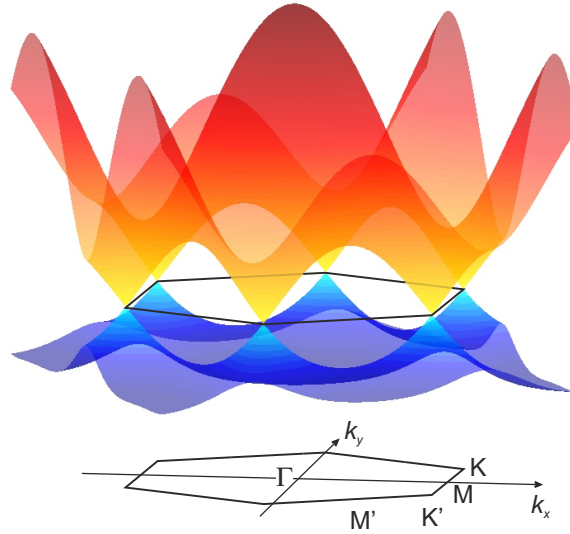


Figure 2.2: Full band structure of graphene in the Brillouin zone calculated from a tight-binding model with the hopping energies $t = 2.7$ eV and $t' = -0.2t$.

2.2 OPTICAL PROPERTIES OF GRAPHENE

2.2.1 Optical conductivity

While the DC conductivity is typically measured in transport experiments, the frequency-dependent optical conductivity becomes important when light interacts with a material. For light of frequency ω and wave vector \vec{k} , the electric field is given by

$$\vec{E} = \vec{E}_0 \exp(\vec{k}\vec{r} - \omega t). \quad (2.6)$$

The complex dielectric function ϵ and the complex optical conductivity σ describe the response of the material to the excitation field. They are introduced through the constitutive relations of Maxwell's equations:

$$\vec{D}(\vec{k}, \omega) = \epsilon(\vec{k}, \omega) \vec{E}(\vec{k}, \omega) \quad (2.7)$$

$$\vec{j}(\vec{k}, \omega) = \sigma(\vec{k}, \omega) \vec{E}(\vec{k}, \omega) \quad (2.8)$$

where \vec{D} is the electric displacement field and \vec{j} the electric current density. At optical frequencies, the dependency on the wave vector can be neglected.

The response functions are linked via

$$\epsilon(\omega) = \epsilon_0 + \frac{i\sigma(\omega)}{\omega} \quad (2.9)$$

with the vacuum permittivity ϵ_0 . Quantities like reflectivity or transmission that are typically observed in optical experiments emerge directly from the response functions. For example, the optical absorption is proportional to the real part of the conductivity (at normal incidence).

The optical properties of graphene arise once again from its unique band structure and 2D nature. Depending on the wavelength regime, two distinct contributions need to be considered. While interband transitions define the optical response from visible down to mid-infrared photon energies, intraband processes corresponding to conduction by free carriers become important in the far-infrared [49, 50]. The different mechanisms are shown schematically in figure 2.3. While for intraband transitions momentum conservation requires scattering on, for example, phonons or defects, interband transitions are direct transitions.

2.2.2 Interband transitions: constant absorption and Pauli blocking

The optical conductivity arising from interband transitions in graphene is expected to be a universal constant in a broad range of photon energies [51, 49]:

$$\sigma_0 \equiv \frac{e^2}{4\hbar} \approx 6.08 \times 10^{-5} \Omega^{-1}. \quad (2.10)$$

Remarkably, the optical response is hence independent of both frequency and material parameters, but is a direct consequence of the linear dispersion at the Dirac point. From equation 2.10, it follows that the absorption of a graphene sheet at visible and near-infrared wavelengths can be expressed as [52]

$$A = \frac{\pi e^2}{\hbar c} = \pi\alpha \approx 2.3\%, \quad (2.11)$$

so that the optical response of graphene is defined solely by the fine structure constant $\alpha \approx 1/137$. Equation 2.11 coincides with the absorption of photons by 2D massless Dirac particles calculated with Fermi's golden rule. The validity of this result has been confirmed by spectroscopic experiments on free-standing graphene in the visible wavelength regime [53]. The absorption of 2.3% is a surprisingly high value for a monolayer and makes it possible to identify individual graphene layers with the bare eye. When more than one graphene layer is considered, the absorption increases linearly with the layer number N as $A \approx N\pi\alpha$ (for $N < 5$) [53].

As mentioned above, the Fermi energy can be shifted away from the Dirac point by doping. Moreover, a finite temperature smears out the distribution of charge carriers at the Fermi level. Both effects hence influence the optical conductivity

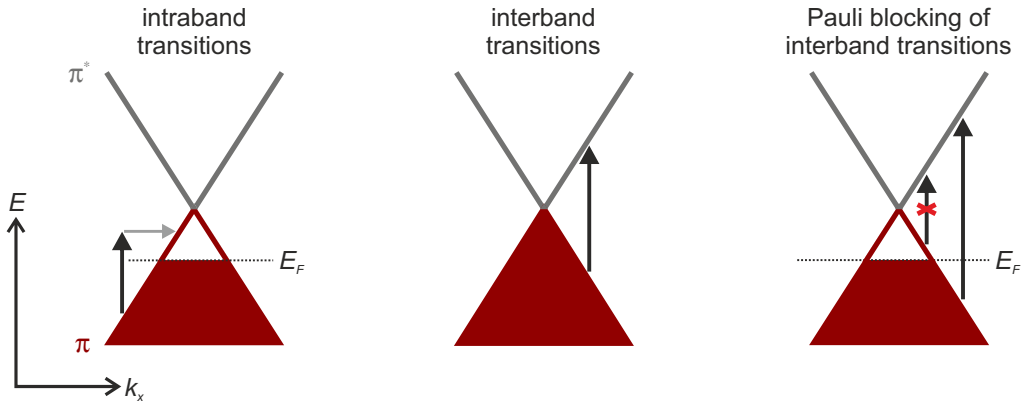


Figure 2.3: Schematic view of intra- and interband transitions near the Dirac point of graphene. Additional momentum for example from phonon scattering (gray arrow) is needed for intraband transitions. Pauli blocking of interband transitions occurs for $E < 2E_F$ when the Fermi energy deviates from the charge neutrality point.

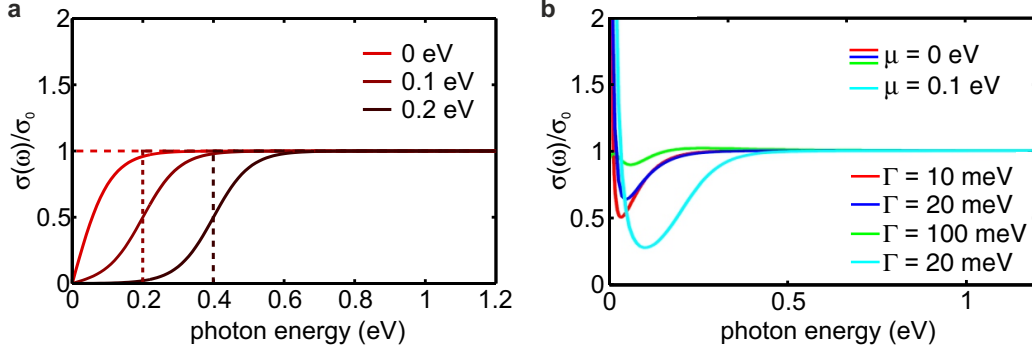


Figure 2.4: Optical conductivity of graphene at low photon energies. **a)** Interband transitions at room temperature (solid lines) and $T = 0$ K (dashed lines) for different values of the chemical potential μ , illustrating the Pauli blocking. In **b)**, the intraband term is also taken into account with different scattering rates $\Gamma = 1/\tau$ (adapted from [54]).

at low energies. This can be taken into account by a Fermi-Dirac distribution so that [54]

$$\sigma(\omega, \mu, T) = \frac{e^2}{2\hbar} \left[\tanh\left(\frac{\hbar\omega + 2\mu}{4k_B T}\right) + \tanh\left(\frac{\hbar\omega - 2\mu}{4k_B T}\right) \right] \quad (2.12)$$

where μ is the chemical potential corresponding to the deviation of the Fermi energy from the Dirac point. Regarding the interband transitions, photons with energies smaller than 2μ cannot excite transitions because the initial or final states are not occupied (see also figure 2.3). Figure 2.4a shows this so-called Pauli blocking in the conductivity spectra for different values of the chemical potential, calculated from equation 2.12. For intrinsic doping and at room temperature, the influence of these corrections can be neglected at photon energies larger than 0.5 eV, as has been confirmed experimentally [54].

2.2.3 Intraband transitions: Drude model

At very low photon energies, the intraband response from the quasi-free carriers can be described to a good approximation with a Drude model [49, 55]. The frequency-dependent conductivity is then given by

$$\sigma(\omega) = \frac{\sigma_0}{1 + i\omega\tau} = \frac{iD}{\pi(\omega + i\tau)} \quad (2.13)$$

where τ is the electron scattering time.

The Drude weight $D = v_F e^2 \sqrt{\pi n} = e^2 / \hbar E_F$ with the charge carrier density n deviates from its conventional form due to the zero mass of the charge carriers. Equation 2.13 can be generalized for finite temperatures and doping with the Kubo formula [56, 54]. The optical conductivity considering both intra- and interband contributions is shown in figure 2.4b for different values of the Fermi energy and typical scattering times [54]. The intraband transitions lead to a strong increase of the optical conductivity at very small photon energies $\omega \ll 0.5$ eV and hence are not relevant in the wavelength regime considered in our experiments.

Consequently, the optical response of graphene in the visible and near-infrared regime is constant as both the contribution from intraband transitions as well as temperature- and doping-corrections to the interband transitions can be neglected. At these photon energies, the conductivity is still defined by the approximately linear dispersion in the vicinity of the Dirac cones. In chapter 3 of this thesis, we will show that this approximation breaks down at even higher photon energies in the ultraviolet where the band structure exhibits a saddle point.

2.2.4 Plasmons in graphene

An additional phenomenon that is observed in the optical response of graphene are plasmons, i. e. a collective oscillation of the free charge carriers. Plasmons in graphene are distinct from those in metals or other two-dimensional electron gases (2DEGs) due to the exceptional nature of the Dirac particles.

While plasmons are strongly damped and hence cannot be excited in undoped graphene, they are supported in doped graphene where the density of states at the Fermi level is finite [16].

The Dirac equation for massless charge carriers in 2D implies that the plasmon frequency scales with the Fermi energy and the carrier density as $\omega_p \simeq E_F^{1/2} \simeq n^{1/4}$ [57, 16] as compared to $\omega_p \simeq n^{1/2}$ in conventional semiconductors. In contrast to metals, the plasmonic response in graphene is therefore tunable over a wide energy range with the help of doping, where carrier densities as high as $n \simeq 10^{14} / \text{cm}^2$ have been reached [58].

For sufficiently high doping ($E_F > \hbar\omega$), the wavelength of the propagating surface plasmons in graphene is given by [8]

$$\lambda_p \approx \lambda_0 \frac{4\alpha}{\epsilon_r + 1} \frac{E_F}{\hbar\omega} \quad (2.14)$$

where ϵ_r is the substrate permittivity and λ_0 the free-space excitation wavelength. This relation is governed by the fine structure constant α and indicates a strong localization of the plasmonic mode as the wavelength is strongly reduced compared to the excitation wavelength.

In practice, the large momentum mismatch between photons and plasmons must be overcome in order to observe a plasmonic response. This has for example been achieved by near-field infrared excitation of graphene sheets with a metal tip [59, 60]. Alternatively, localized plasmons can be observed in graphene nanostructures such as nanoribbons where the plasmon resonance additionally scales with the structure size w as $\omega_p \simeq n^{1/4} w^{1/2}$ [61]. The missing momentum could also be provided by an emitter which couples to a graphene sheet, potentially offering a platform to study quantum effects like vacuum Rabi splitting [8].

Summarizing, plasmons in graphene provide an attractive alternative to metal plasmonics as they offer a wide tunability and exhibit high field confinement. However, graphene plasmonics is so far limited to infrared wavelengths due to experimental restrictions on both doping and structure size and is therefore not studied in this thesis.

2.3 SAMPLE FABRICATION AND CHARACTERIZATION

As shown in 2004 by Geim and Novoselov, graphene as well as other 2D crystals can easily be obtained by mechanical cleavage from bulk material [6, 7]. All samples studied in this thesis are prepared using the mechanical exfoliation method described in the following. Although alternative preparation techniques such as chemical vapor deposition or chemical exfoliation provide large area samples and consequently are promising for graphene applications, the quality of the exfoliated graphene flakes is still unsurpassed.

2.3.1 Exfoliation of graphene from graphite

Graphite is a 3D stack of graphene layers. While the σ bonds within the graphene planes are strong, the individual layers are only weakly coupled by van der Waals forces and can hence easily be separated. In the original approach [7], the layered crystal is rubbed against another solid surface where a variety of flakes attaches. In fact, graphene layers are deposited onto paper whenever we draw with a pencil. This method has been further optimized regarding both the yield of monolayers as well as the size of the obtained flakes. Starting from a

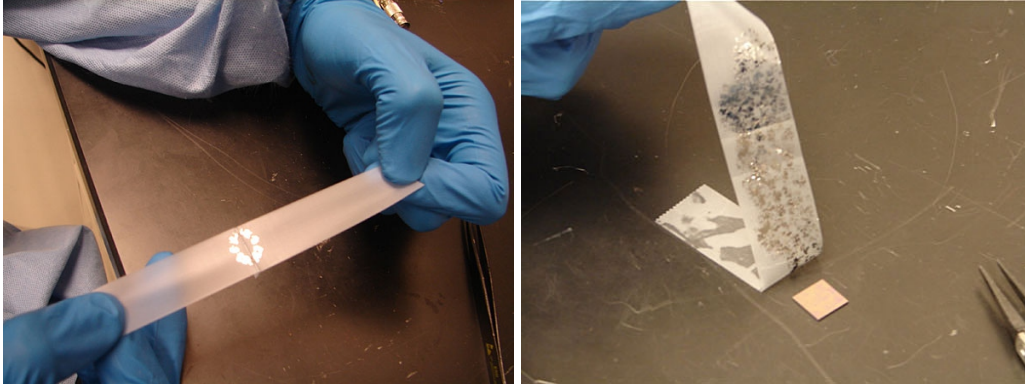


Figure 2.5: Mechanical exfoliation of graphene from graphite flakes using adhesive tape. Images are taken from [62].

small piece of highly oriented pyrolytic graphite (HOPG), adhesive tape (typically Scotch or Nitto) is used to peel off thinner pieces from the graphite as shown in figure 2.5. These layers are thinned out further by repeated peeling with the tape until transparent few-layer flakes are observed. The tape is then pressed against a substrate transferring part of the flakes. That way, graphene layers of different thickness with a size up to about 100 μm can be obtained.

2.3.2 Characterization methods: optical microscopy and Raman spectroscopy

The first characterization of graphene samples is done with an optical microscope. Most samples were exfoliated on an oxidized silicon substrate. Due to the oxide layer, even thin layers give substantial contrast with respect to the empty substrate. As they are transparent, the optical path adds up and the interference color changes [7]. We mostly used substrates with a 300 nm thick oxide layer, which give optimum contrast under white light illumination [63]. As shown in figure 2.6, graphene flakes can be identified with the bare eye and located within the marker grid on the sample for a later measurement.

To further confirm that the identified flakes are monolayer graphene, Raman spectroscopy is a commonly used tool. Here, the exciting laser light interacts with the vibrational, rotational, and other low-energy modes of the system, so that the scattered light exhibits lines shifted with respect to the excitation energy by the energy of the corresponding mode. This Raman shift Δw indicates the Raman wavelength λ_1 relative to the excitation wavelength λ_0 as

$$\Delta w = \frac{1}{\lambda_0} - \frac{1}{\lambda_1}. \quad (2.15)$$

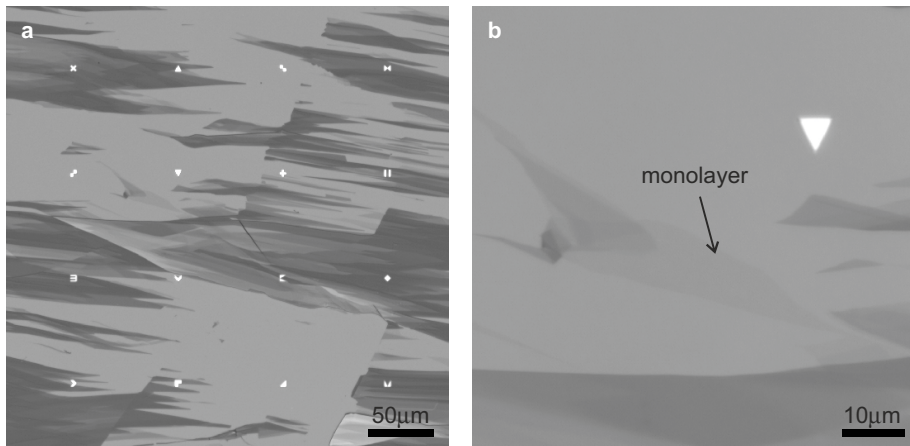


Figure 2.6: Identification of graphene flakes on an oxidized silicon substrate with an optical microscope. **a)** With low magnification (20x objective), a variety of flakes of different contrast and hence different thickness are visible. The flakes are localized in the array of marker structures. **b)** Monolayer graphene flakes can be identified under high magnification (100x objective).

It provides a fingerprint of the molecular structure of the sample and can be used to monitor changes of the chemical bonds.

Graphene's electronic structure leads to a unique Raman spectrum with two prominent modes as shown in figure 2.7. The G peak at 1580 cm^{-1} corresponds to a high-frequency E_{2g} phonon [64, 65], where the two sublattices oscillate

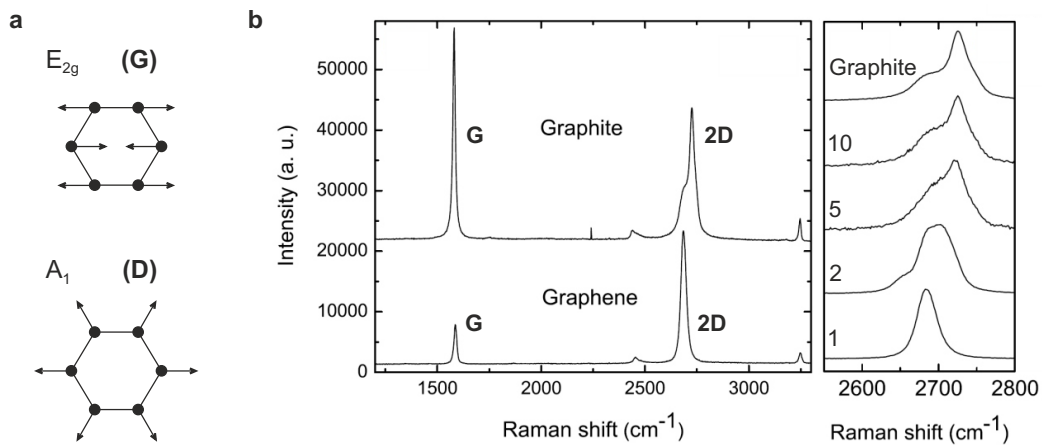


Figure 2.7: **a)** Underlying phonon modes of graphene's Raman spectrum. **b)** Raman spectrum of graphene and graphite and the evolution of the 2D peak with increasing layer number. Taken from [64].

against each other as illustrated in figure 2.7a. The D peak at about 1350 cm^{-1} can only be excited in the presence of defects, its absence thus indicates a high quality of the graphene sheet. As shown in figure 2.7a, this mode is due to the breathing of the carbon ring [65]. The most prominent feature at about 2700 cm^{-1} is the second order of the D peak and therefore called 2D peak. It is a two-phonon band and is also allowed in defect-free graphene, as momentum is always conserved in this second-order process [64, 65].

The shape of the 2D Raman peak of graphene changes distinctly with the layer number [64] as shown in figure 2.7b. Bilayer graphene exhibits a much broader and red-shifted 2D band compared to its monolayer. It has four components, related to the splitting of the π and π^* bands into subbands. For more than 5 layers, the spectrum can hardly be distinguished from graphite anymore, where the 2D peak consists of two components. Consequently, Raman spectroscopy can clearly distinguish between different layer numbers.

Apart from the quality and the layer number of the sample, Raman spectroscopy allows to determine the crystallographic orientation and to monitor perturbations of the structure induced for example by strain, which will be used and shown in section 4.5 of this thesis.

Optical microscopy combined with Raman spectroscopy allows a quick localization of graphene flakes and confirms the layer thickness and sample quality. Further characterization methods (like for example AFM or TEM measurements) are thus not necessary for this work.

2.3.3 *Transfer to an arbitrary substrate*

After the graphene samples are characterized, the flakes can be transferred to an arbitrary substrate using a polymer membrane. This method permits also the fabrication of free-standing graphene flakes as are considered in the transmission experiments in section 3.2.

The key steps of the transfer process are illustrated in figure 2.8. First, the substrate with exfoliated graphene is coated with a few hundred nanometer thick layer of polymer resist (PMMA, poly(methyl methacrylate)). To obtain free-standing samples, apertures with a diameter of a few μm are written on top of the flakes using electron beam lithography. This lithography technique is essential for the fabrication of plasmonic nanostructures; a detailed description of the process is given in section 6.1. After patterning, the resist is developed to remove the exposed areas. To obtain supported samples, i. e. when graphene is transferred to an arbitrary substrate, the patterning and development steps are skipped. The polymer layer together with the graphene flakes are then detached

from the substrate by etching the silicon dioxide layer in a 5% sodium hydroxide solution at 90°C. The membrane which floats on the water surface is fished out to rest on the desired substrate. In order to maintain the free-standing character of the sample, a quartz frame is used to support the membrane. Regarding the supported samples, the resist layer can finally be dissolved with acetone.

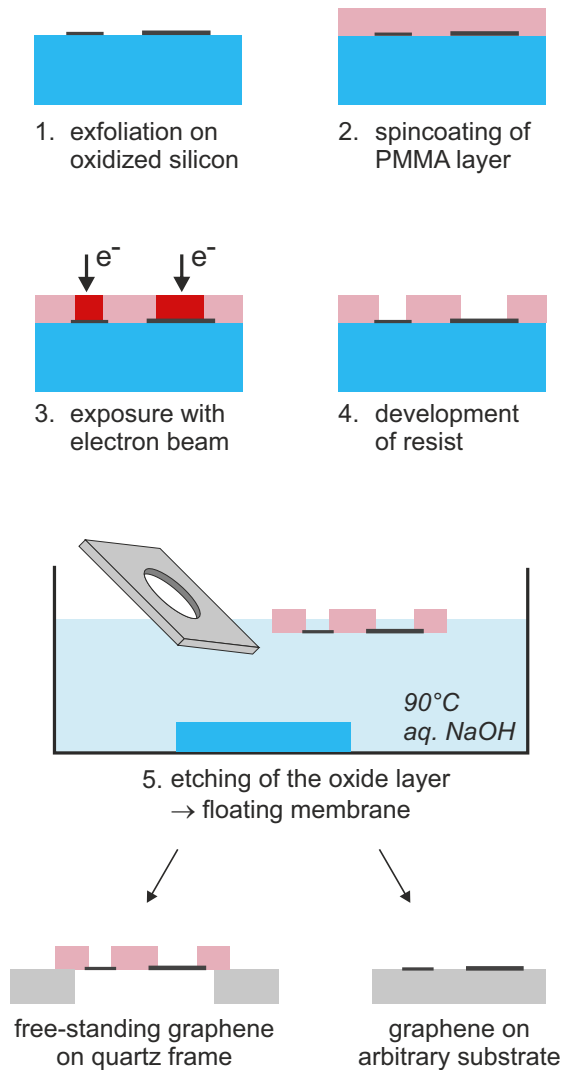


Figure 2.8: Key steps of the graphene transfer process. Electron beam exposure and development is relevant for the free-standing graphene samples only, so that step 3 and 4 are optional. The membrane with the graphene flakes can be fished out either with quartz frame to obtain free-standing samples or with an arbitrary substrate for which the PMMA layer can be washed off.

This chapter follows closely the identically named book chapter in "Optical properties of graphene" [32] and is based on the publication "Excitonic Fano Resonance in Free-Standing Graphene" by our coworkers [31].

As has been shown in section 2.2, at frequencies above the far-infrared region, the optical response of graphene is dominated by interband transitions between the valence and conduction band. This leads to a constant absorption of $\pi\alpha$ at near-infrared and visible wavelengths. In this chapter, the optical properties at even higher photon energies are considered. The band structure of graphene exhibits a saddle point between two neighboring Dirac cones, so that the approximation of the linear dispersion must break down at some point. As a consequence, the optical absorption is expected to deviate from its constant value for photon energies in the visible and ultraviolet regime.

This chapter covers the linear optical response of graphene near the saddle point. After a theoretical treatment of saddle point phenomena like the van Hove singularity (section 3.1), the experimental method based on transmission spectroscopy of graphene in the ultraviolet and visible wavelength regime will be presented in section 3.2. We will then show that the optical properties of graphene near the saddle point can only be explained when many-body effects like electron-hole interactions are taken into account (section 3.3). A simple model based on the classical theory by Fano is presented in section 3.4 which is able to describe the response down to near-infrared energies. In section 3.5, general properties of the excitonic resonance in graphene and graphene-related materials as well as its dependence on influences like doping will be discussed. Finally, we demonstrate that the optical constants of graphene can be extracted from a fit to the Fano model in combination with the Kramers-Kronig relations.

3.1 VAN HOVE SINGULARITIES IN THE BAND STRUCTURE

In a solid state system, the electronic states form bands, described by a dispersion relation $E(\vec{k})$ which relates the energy of the state with the electron wavevector \vec{k} . Many different wavevectors can result in the same energy. The density of states ρ gives the number of states that fall within an energy range E to $E + dE$

$$\rho(E) = \frac{1}{4\pi^3} \int \frac{dS_{\vec{k}}}{|\nabla_{\vec{k}}E(\vec{k})|}. \quad (3.1)$$

where $dS_{\vec{k}}$ is a surface of constant energy E . Obviously, the density of states diverges at points where the dispersion relation $E(\vec{k})$ exhibits a horizontal tangent, i. e. when $\nabla_{\vec{k}}E = 0$, as pointed out by van Hove [66]. The wavevectors at which van Hove singularities occur are the critical points of the Brillouin zone.

Optical spectra are related to transitions between electronic states. The transition probability W_{if} of transitions excited by a photon with energy $E = \hbar\omega$ are described by Fermi's golden rule as

$$W_{if} \cong \frac{2\pi}{\hbar} |\langle f|\hat{H}'|i\rangle|^2 \rho_j(E). \quad (3.2)$$

$|i\rangle$ and $|f\rangle$ represent the initial and final states of the transition. \hat{H}' is the perturbation operator, which for optical transitions is proportional to the dot product of the vector potential \vec{A} and the dipole operator \hat{p} [67]. $\rho_j(E)$ is the joint density of states [68]. It is calculated according to equation 3.1, replacing the electronic band $E(\vec{k})$ with the optical band $E_{cv}(\vec{k}) = E_c(\vec{k}) - E_v(\vec{k})$. E_c and E_v are the dispersion relations of conduction and valence band, respectively [69]. So-called optical critical points occur when $\nabla_{\vec{k}}E_{cv} = \nabla_{\vec{k}}E_c - \nabla_{\vec{k}}E_v = 0$ [69].

Van Hove singularities are classified by the curvature of the bands when moving away from the critical points. In two and three dimensions, a critical point can represent a minimum or a maximum in the band separation or else a saddle point, whereas in the one dimensional case only a minimum or a maximum is possible. The behavior of the density of states in the vicinity of a critical point depends on the type of the van Hove singularity as well as the dimensionality of the system [67].

Looking at the band structure of graphene shown in figure 3.1a, we can identify a saddle point at the M point in the Brillouin zone. Here, both electronic bands and hence also the optical band E_{cv} have a horizontal tangent. Consequently, an electronic and an optical critical point coincide at the M point of graphene. At a

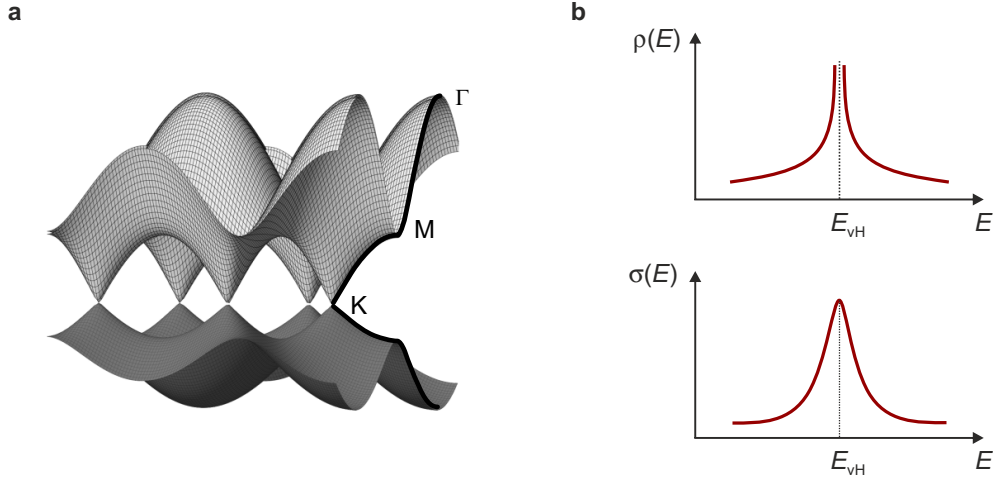


Figure 3.1: a) Band structure of graphene with Dirac point K, center of the Brillouin zone Γ , and saddle point M. E_{vH} is the energy gap at the saddle point. b) Schematic dependence of the density of states and the optical conductivity on the energy in the vicinity of the van Hove singularity E_{vH} at a saddle point in a two dimensional system.

saddle point with energy gap E_{vH} in a two dimensional system, the joint density of states is given by

$$\rho(E) \propto -\ln|E - E_{vH}|. \quad (3.3)$$

Since the density of states is symmetric around the singularity, from Fermi's golden rule one would expect the optical spectrum to be also symmetric around E_{vH} as schematically shown in figure 3.1b. Towards lower energies, the linear dispersion at the Dirac cones shapes the optical response. Here, the universal value of the optical conductivity of $\sigma(E) = \pi e^2/2h$ should be recovered, corresponding to a constant absorbance of $\pi\alpha \approx 2.3\%$ for monolayer graphene [52, 53].

3.2 EXPERIMENTAL REALIZATION: TRANSMISSION SPECTROSCOPY

To investigate the optical properties of graphene in the visible and ultraviolet wavelength regime, different sample and measurement geometries are possible. In the following, we will describe in more detail a transmission measurement of free-standing graphene which has been published in [31].

Free-standing graphene samples can be fabricated by transferring graphene from a substrate to an aperture of polymer resist. This geometry is advantageous

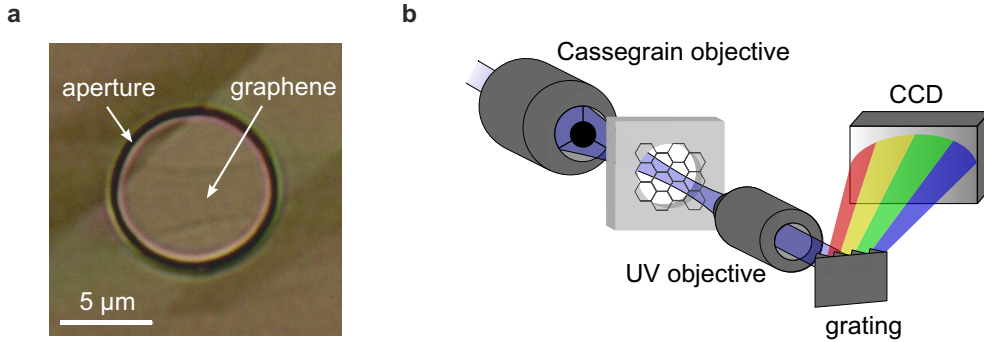


Figure 3.2: a) Optical microscope image of a measured free-standing graphene layer, taken in transmission mode. b) Schematic view of the experimental setup. Adapted from [31].

as it eliminates potential influences of the substrate, so that the response is purely determined by the optical properties of the graphene sheet. The graphene flakes are first exfoliated from natural graphite on an oxidized silicon substrate. The number of layers can be determined by the optical contrast in a microscope image and by Raman spectroscopy. The sample is coated with a polymer resist and apertures with a diameter of a few μm are written on top of the flakes using electron beam lithography. After development, the structured polymer layer together with the graphene flake are removed from the substrate by etching the silicon dioxide in an alkaline solution. A typical free-standing graphene sample is shown in figure 3.2a. Due to the 2.3% absorption in the visible, we can identify the graphene sheets that extend over the holes in the polymer layer.

The transmission of the samples is measured in a confocal microscope (see figure 3.2b). The light source combines a tungsten halogen bulb and a deuterium lamp, providing unpolarized white light with photon energies from 1.5 to 5.5 eV. The light is focused onto the sample by an all-reflective Cassegrain objective and the transmitted light is collected with a UV microscope objective. The spatial resolution on the sample is better than $1.5 \mu\text{m}$, ensuring that only the free-standing part of the graphene flake is measured. The transmitted light is analyzed in a spectrometer consisting of a monochromator and a CCD camera as detector. The spectrum is combined from exposures with two different gratings. The transmittance T is defined as

$$T = \frac{T_g - T_r}{T_r}, \quad (3.4)$$

where T_g is the transmission through the graphene layer and T_r the transmission through an empty reference aperture. This normalization eliminates all spectral

dependencies of the setup such as the lamp spectrum, possible dispersion of the optical elements etc. The weak absorption of the thin graphene sheets implies a negligible reflectance, hence the absorbance A follows directly from the transmittance as $A = 1 - T$.

The measured absorption spectra for monolayer and bilayer graphene are shown in figure 3.3a. At low photon energies below 2 eV, the absorption spectra are almost flat and approach the predicted value of $\pi\alpha$ and $2\pi\alpha$ for the monolayer and the bilayer sample, respectively. Towards higher energies, the absorbance increases monotonically until it reaches a maximum value at about 4.6 eV. Beyond the peak, it steeply decreases, thus giving rise to an asymmetric line shape. The absorbance of graphene in the UV reaches a maximum of about 11%, a strikingly high value for a single-atom thick system.

Our results are in accordance with those obtained from reflectivity measurements on graphene on a silicon dioxide substrate [70] as well as the absorption and transmission curves from ellipsometric data [71]. Both find an asymmetric line shape and a redshift from the van Hove singularity. For graphene supported on a transparent substrate with negligible absorption and refractive index n_s , the optical conductivity is related to absorbance and transmittance via [72, 70]

$$\sigma(E) \propto A = \frac{n_s - 1}{2} T = \frac{n_s^2 - 1}{4} R. \quad (3.5)$$

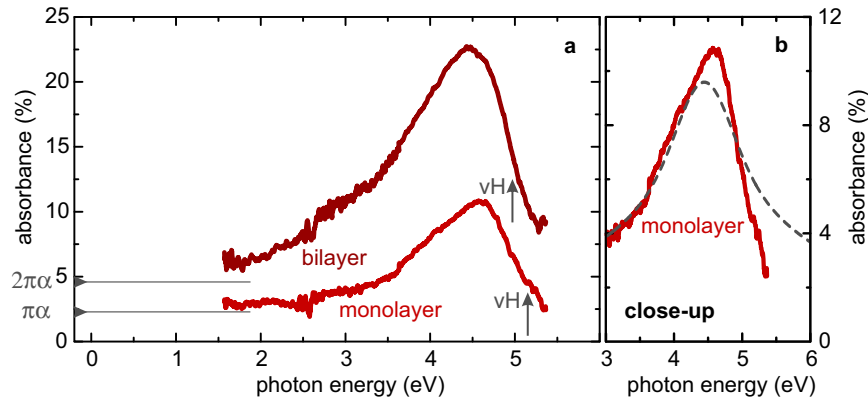


Figure 3.3: **a)** Measured absorbance $A = 1 - T$ spectrum of free-standing mono- and bilayer graphene (red lines). The curves approach the universal value of $\pi\alpha$ and $2\pi\alpha$ at lower energies, but the peaks are red-shifted compared to the energy of the van Hove singularity (vH). **b)** Close-up up showing that the asymmetric line shape of the monolayer spectrum (red line) cannot be brought into agreement with a model neglecting electron-hole interactions (grey dashed line). Figure adapted from [31].

The reflectance contrast R is defined and measured in analogy to the transmittance T (see equation 3.4). Due to these simple relations, the data obtained with the different measurement methods can easily be compared.

To model the measured data, we first draw on the relations developed in the previous section. We have seen that the spectral shape of the interband transitions near the saddle point in a two dimensional system is proportional to the joint density of states. To take inhomogeneous broadening due to carrier relaxation into account, the resulting line shape can be convoluted with a Gaussian function of width γ . This simple single-particle model based on band-to-band transitions thus predicts a symmetric absorption spectrum of the shape

$$A(E) = B + C \left[\exp \left(-\frac{(E - E_{vH})^2}{\gamma^2} \right) \otimes [-\ln|E - E_{vH}|] \right]. \quad (3.6)$$

E_{vH} is given by the transition energy at the van Hove singularity, which is about 5.15 eV for monolayer and 5.0 eV for bilayer graphene [73]. The constant absorption at low energies from the Dirac cones is modeled as an offset B , so that the constant scaling factor C and the width γ are the only free parameters.

However, this model utterly fails to describe the measured absorbance spectrum as is shown in the close-up in figure 3.3b. The measured absorbance peak is red-shifted compared to the position of the van Hove singularity to about 4.6 eV. However, even when the van Hove singularity is shifted to this energy as in figure 3.3b, the pronounced asymmetry of the line shape disagrees with the predicted symmetric response. Obviously, the absorption spectrum of free-standing graphene in the visible and UV regime cannot be described considering band-to-band transitions only. In this approximation, the charge carriers are uncorrelated and interactions are not taken into account. We therefore conclude that many-body effects cannot be neglected here and we will address this issue in the next sections.

3.3 SADDLE POINT EXCITONS AND MANY-BODY EFFECTS

As we have seen in the previous section, the single non-interacting particle picture fails to describe the absorption spectrum of graphene in the visible and UV regime. A similar effect has been observed in the optical spectra of bulk semiconductors such as CdTe or ZnTe [74], where the discrepancies between experiment and theory based on band-to-band transitions have been explained by Coulomb effects between electrons and holes at the critical points [75]. When an electron is excited from the valence to the conduction band, it will interact with the remaining electrons in the valence band, which can also be

described in terms of the interaction with a hole. Due to the attractive Coulomb interaction between electron and hole, their motion will be correlated, resulting in a bound electron-hole pair known as an exciton. Assuming that excitonic states exist in the vicinity of the saddle point, the optical spectra of CdTe and ZnTe have been explained successfully. Since the constant energy surfaces near a saddle point have hyperbolic shape, such excitonic states are called hyperbolic or saddle point excitons [67]. In analogy to the semiconductor example, we will in the following assume an excitonic state near the saddle point in graphene.

Depending on the screening of the Coulomb interaction by the valence electrons, excitons can be weakly to tightly bound. In semiconductors, where the binding energy of an exciton can be described in analogy to the hydrogenic atom, the screening scales inversely with the dielectric constant of the material and is usually on the order of a few meV [67]. In three dimensional bulk metals, the screening is large and thus usually prevents correlated electron-hole pairs [76]. However, when the dimensionality is reduced such as in one-dimensional metallic carbon nanotubes, the screening is weakened so that excitonic correlations can occur [77].

The screening depends on the density of states near the Fermi energy. Graphene is a semi-metal, so that the density of states vanishes at the Dirac point and then grows linearly. In bilayer graphene, however, the density of states is constant and nonzero near the Dirac point [16]. For Fermi energies near the Dirac point, the screening ability of electrons in monolayer graphene is therefore reduced compared to the bilayer. Hence, we expect that the exciton binding energy, corresponding to the energy difference between the saddle point and the discrete excitonic state, is larger in monolayer than in bilayer graphene.

The influence of excitonic effects on the optical response of graphene has first been investigated theoretically by Yang et al. [73]. Using first-principles calculations based on a many-body Green's function, this approach indicates remarkable effects of Coulomb interactions on the optical response of graphene. According to these calculations, the attractive interactions between electrons and holes dominates over the repulsive interaction between the electrons. Overall, a red-shift of the absorption peak to about 4.5 eV with an asymmetric line shape is predicted, which is in very good agreement with the effects observed in the measurements.

Consequently and in accordance with the interpretation of other groups [71, 70], it is a clear signature of saddle point excitons that is observed in the optical spectrum of graphene in the visible and ultraviolet wavelength regime. Due to the attractive interaction between electron and hole, these excitons form

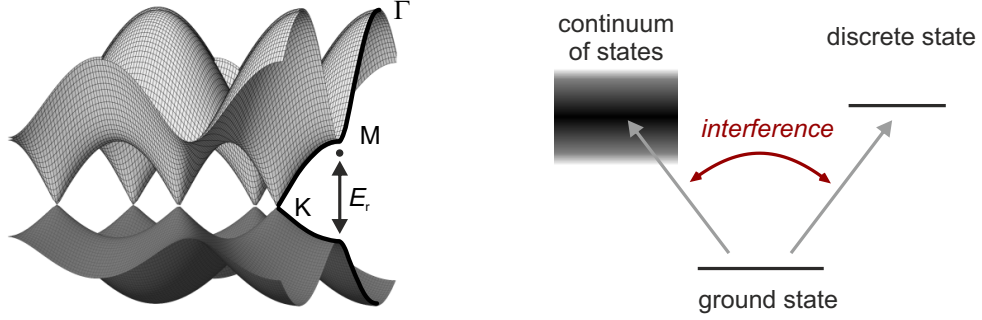


Figure 3.4: Band structure of graphene with the discrete excitonic state (marked as a dot) near the saddle point M with resonance energy E_r . Note that this sketch merges one- and two-particle pictures for a more intuitive visualization. As schematically shown on the right, a Fano resonance can be interpreted as interference between transitions to a discrete state and a continuum of states.

a discrete state at an energy slightly below the saddle point as indicated in figure 3.4. In the next section, we introduce a simple model to calculate the optical response of graphene including excitonic effects.

3.4 INTERPRETATION OF THE SPECTRUM WITH A CLASSICAL FANO MODEL

To explain the influence of electron-hole interactions on the optical spectra of semiconductors, Phillips drew on the classical theory developed by Fano [78, 79]. In this picture, a resonance occurs when a discrete state couples to a continuum of states, giving rise to an asymmetric line shape. Fano interpreted this in a general approach by configuration interaction between two quantum mechanical channels, belonging to transitions to the discrete state and the continuum, respectively. In graphene, the discrete excitonic state near the M point in the band structure overlaps with the continuum of states descending from the saddle point down to the Dirac point, the so-called Dirac continuum, as shown in figure 3.4.

With the Fano model, the resulting absorption spectrum has the form

$$A_{\text{Fano}}(E) = C \frac{(s+q)^2}{1+s^2} = C \left(1 + \frac{q^2-1}{1+s^2} + \frac{2qs}{1+s^2} \right), \quad (3.7)$$

with

$$s = \frac{E - E_r}{\gamma/2}. \quad (3.8)$$

The Fano resonance can be interpreted as interference between the two channels, i. e. between transitions into the continuum and to the discrete state (see figure 3.4). Here, the discrete exciton state is modeled as a Lorentzian resonance of width γ and energy E_r . These quantities determine the parameter s . The unit-free Fano parameter q is given by the ratio of the transition probabilities to the discrete state and to the continuum. C is an overall scaling factor.

The three terms in the parentheses of equation 3.7 correspond to the spectrally constant absorption of the Dirac continuum, the discrete state, and the interference, respectively. The interference term leads to the asymmetric line shape, which can be ascribed to destructive interference between the channels. Alternatively, it can be understood in terms of the phase change by π of the Lorentzian in the vicinity of the resonance. For a negative Fano parameter q , the interference term is positive below the resonance ($s < 0$) and negative above ($s > 0$). Coming from low energies, this leads to the slow increase of the absorbance toward the resonance and the steep decrease beyond. In the limit of vanishing transitions into the continuum, the Fano parameter q becomes infinite and equation 3.7 reduces to a Lorentzian, as expected. Far away from the resonance E_r , the transitions to the continuum dominate the response.

As can be seen in figure 3.5, a Fano model using equation 3.7 excellently describes the measured data over the entire spectral range for both monolayer and bilayer graphene. The asymmetric peak in the ultraviolet is well reproduced in line shape as well as position and there is a very good agreement also down to low photon energies. Table 3.1 summarizes the resulting values of the fit parameters for the two measured samples as well as two other mono- and bilayer samples. The low-energy limit $A(0)$ of the absorption obtained from the fit parameters agrees well with the universal value of $n\pi\alpha$ ($n = 1, 2$). The relevance of the other fit parameters is discussed in the next section in the context of the intrinsic properties of the excitonic state.

Note that no signature of the direct interband transition at E_{vH} appears in the measured and fitted spectra. This can be explained in terms of a redistribution of oscillator strength by the resonant excitons, in accordance with the theory presented above [73].

Finally, we remark that the optical response of graphene is fully determined by the topology of the band structure, whereas its detailed shape seems to be less relevant. To illustrate this idea further, imagine the band dispersion of graphene as a rubber sheet which is pinned down at all points corresponding to the Dirac points in the band structure. If now the sheet is pulled up at the center of each Brillouin zone, automatically a saddle point as well as a continuum of states evolves. Following this topological reasoning, we suggest that the system can

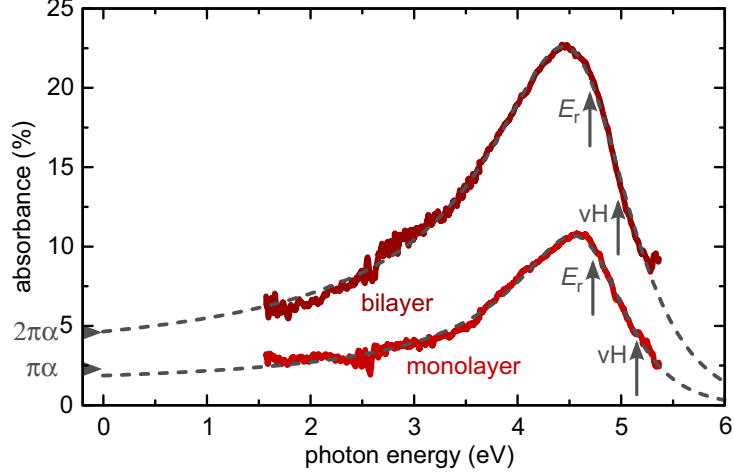


Figure 3.5: The measured absorbance $A = 1 - T$ spectrum of free-standing mono- and bilayer graphene (red lines) are well described by a Fano model (grey dashed lines). The difference between the resonance energy E_r of the exciton and the van Hove singularity (vH) determines the exciton binding energy. Adapted from [31].

data set	E_r (eV)	γ (eV)	q	C (%)	$A(0)/(\pi\alpha)$	E_b (meV)
monolayer*	4.73	1.30	-3.3	0.9	0.82	420
monolayer	4.78	1.58	-3.6	0.7	0.75	370
bilayer*	4.70	1.63	-3.2	2.0	2.0	270
bilayer	4.73	1.39	-3.3	1.8	1.7	240

Table 3.1: Summary of the Fano fitting parameters and deduced values for different samples. The data sets marked with (*) are shown in figure 3.3 and figure 3.5. $A(0)$ is the absorbance at zero energy in units of $\pi\alpha$. E_b is the exciton binding energy calculated from the difference between E_r and the van Hove singularity E_{vH} .

always be described with a single resonance, irrespective of the details of the band structure such as the slope of the Dirac cones. Hence, it is not surprising that we find an excellent agreement between our measured data and a Fano model fit, even when ignoring details of the band structure.

3.5 PROPERTIES OF THE EXCITONIC RESONANCE IN GRAPHENE

3.5.1 *General properties of the excitonic resonance*

The fit parameters from the Fano interference model as listed in table 3.1 reveal several properties of the excitonic resonance.

The binding energy of the exciton is calculated as the energy difference from the resonance to the van Hove singularity as $E_{\text{vH}} - E_r$ (see section 3.3). We find values of about 400 meV for monolayer and 250 meV for bilayer graphene. This confirms the reasoning given in section 3.3 that the binding energy is larger in monolayer graphene due to reduced screening at the Fermi energy. The obtained values of the exciton binding energy are surprisingly large, as compared to a few tens of meV in metallic carbon nanotubes [77].

Whereas there is a systematic variation of the excitonic binding energy between monolayer and bilayer, the other fit parameters γ and q are seemingly only subject to sample-to-sample variation. The linewidth γ corresponds to a lifetime $\tau = \hbar/\gamma$ of the excitonic state. The large values of γ emerging from the Fano fit indicate very short exciton lifetimes on the order of 0.5 fs. Moreover, the linewidth exceeds the exciton binding energy by about a factor of three. Hence, the exciton is strongly modified due to the coherent superposition with the continuum, or, in other words, the exciton quickly decays into the continuum of states. Consequently, one speaks of an excitonic resonance rather than of truly bound excitons in graphene. In this context, a resonant state describes a bound state whose energy level overlaps with the band states of its host [67].

3.5.2 *Influence of doping*

The influence of doping on the excitonic resonance has been studied both experimentally and theoretically by Mak et al. [80]. The measured and calculated optical conductivity spectra for different levels of doping are shown in figure 3.6. In the experiments, a graphene field-effect transistor is prepared on a transparent quartz substrate and contacted with a transparent polymer electrolyte top gate. That way, high carrier concentrations on the order of $n \approx 10^{14} \text{cm}^{-2}$ of both holes and electrons can be obtained, corresponding to a Fermi energy of up

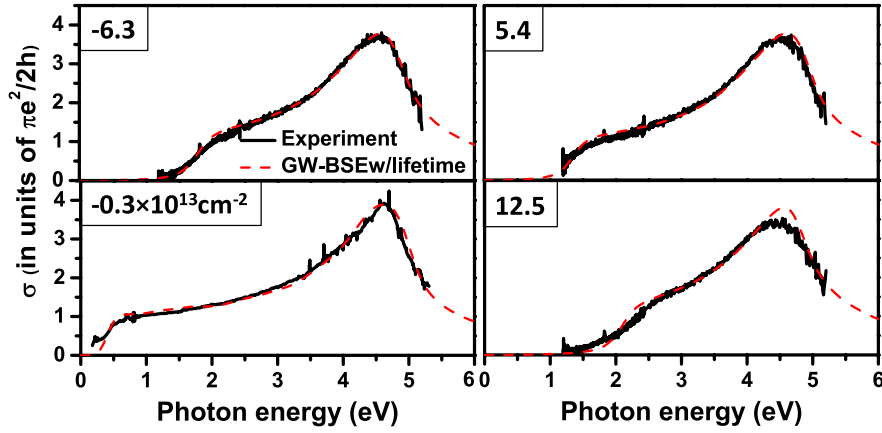


Figure 3.6: Calculated conductivity spectra $\sigma(E)$ with quasiparticle lifetime effects included (dashed red lines) are compared to experimental spectra (solid black lines) for four different doping levels, given by the carrier density n . Adapted from [80].

to 1.2 eV. At low photon energies, a progressive suppression of the absorption is observed with increasing doping, as expected due to Pauli blocking of interband transitions [81]. The absorption peak in the UV shows a redshift and becomes broader as well as more symmetric for both electron and hole doping, whereas the absolute peak height is not affected. All effects can be explained by the increased dielectric screening which leads to a modification of the Coulomb interactions. The enhanced screening weakens the electron–hole interactions, hence giving rise to a more symmetric absorption peak. This agrees with the fact that the symmetric line shape emerging from the band-to-band transitions should be recovered in the limit of vanishing excitonic effects. The redshift of the resonance is attributed to the repulsive electron–electron interaction which with increasing doping dominates over the attractive electron–hole interaction. The increased width of the peak corresponds to a decreased lifetime of the excitonic state. This is the result of an increased density of states at the Fermi energy due to the doping and hence an increased number of available decay channels.

3.5.3 Evolution with increasing layer number

As shown in section 3.4 and 3.5, bilayer graphene exhibits a slightly redshifted excitonic resonance, so that the binding energy of the exciton is reduced compared to monolayer graphene. With increasing layer number $N = 1 - 5$, interlayer interactions modify the band structure, also near the saddle point [82, 83]. Due to the symmetry of the bands, however, only optical transitions with energies compara-

ble to that of the monolayer are allowed. On the other hand, screening increases with the thickness of the sample due to the increasing density of states at the Fermi energy [16]. The peak position is a result of the competing contributions of attractive electron–hole and repulsive electron–electron interaction, as discussed above. While the attractive interaction dominates for monolayer graphene, both contributions are increasingly screened and cancel for $N > 3$ [73]. This is underlined by experiments showing that the optical conductivity increases almost linearly with N and that the peak position exhibits only a negligible redshift [70] which quickly converges towards the value of bulk graphite [84, 73].

3.5.4 *Twisted bilayer graphene*

So far, our discussions have focused on graphene sheets with the most common stacking, so-called Bernal stacking, where adjacent layers are shifted by one atomic spacing. When the layers are twisted compared to the Bernal stacking configuration, interlayer interactions perturb the band structure and additional van Hove singularities emerge, as has been observed for example in bilayer graphene with scanning tunneling spectroscopy [85]. These features are very interesting as they can be tuned via the rotation angle. The rotation-induced van Hove singularities give rise to additional peaks in the optical spectra of twisted bilayer graphene. In addition to the redshift of the peaks due to excitonic effects, coherent interactions between multiple van Hove singularities seem to cause a redistribution of oscillator strength [86].

3.5.5 *Graphene-related low-dimensional systems*

When the dimensionality of graphene is further reduced by structuring it for example into nanoribbons, excitonic effects will dominate the spectrum as a consequence of enhanced Coulomb interactions. However, the band structure is completely altered compared to graphene so that the excitons observed in graphene nanoribbons are of different nature. They are not related to a saddle point but to van Hove singularities at the band gap or represent so-called dark edge excitons [87, 88]. The emerging excitonic peaks in the optical spectrum depend on the structure and width of the ribbons and are in the visible energy range for few nanometer wide ribbons [89]. The behavior is very similar to that of one dimensional carbon nanotubes [90, 91, 92]. This does not come as a surprise, since graphene nanoribbons essentially are unzipped carbon nanotubes.

Besides graphene, a lot of attention has been paid recently to other two dimensional crystals that exhibit a hexagonal arrangement of atoms, the so-called graphene analogues. Extensively studied systems are monolayers of hexagonal

boron nitride as well as transition metal dichalcogenides (XY_2 , with $X=Mo,W$ and $Y=S,Se,Te$). These systems offer an interesting alternative to graphene especially regarding optoelectronic applications as they possess sizable band gaps of a few hundred meV up to a few eV, hence allowing to build switchable devices. Excitonic states have also been observed in the optical response of these materials in the visible and ultraviolet wavelength regime [93, 94, 10, 95]. As for nanoribbons, these excitonic states are related to the band gaps at the K point of the band structure.

3.6 DERIVATION OF THE OPTICAL CONSTANTS FROM THE FANO MODEL

In the last section of this chapter, we would like to address an additional benefit of the Fano model. In combination with the Kramers-Kronig relations, the optical constants can be recovered from measured optical spectra. This represents an interesting alternative to ellipsometric measurements that are often used to determine optical constants.

In general, the complex refractive index and the complex dielectric function are linked via

$$\tilde{n} = n + i\kappa = \sqrt{\tilde{\epsilon}} = \sqrt{\epsilon_1 + i\epsilon_2}. \quad (3.9)$$

The real part n of the complex refractive index describes the dispersion. The imaginary part κ is called the extinction coefficient and captures the absorption of the material.

Kramers-Kronig relations describe the fundamental connection between the real and imaginary parts of a system's response to a sinusoidal perturbation. An important application in optical spectroscopy is the calculation of the real refractive index from the extinction coefficient typically measured in transmission [69]. When both quantities are measured, the Kramers-Kronig relations are used to check the consistency of the data.

In the formulation by Kramers [96], the real and imaginary part of the dielectric function are connected by integral relationships as follows:

$$\epsilon_1(\omega) - 1 = \frac{2}{\pi} \mathcal{P} \int_0^\infty \frac{\epsilon_2(\omega')\omega'}{\omega'^2 - \omega^2} d\omega' \quad (3.10a)$$

$$\epsilon_2(\omega) = -\frac{2\omega}{\pi} \mathcal{P} \int_0^\infty \frac{\epsilon_1(\omega') - 1}{\omega'^2 - \omega^2} d\omega' + \frac{4\pi\sigma_{DC}}{\omega}, \quad (3.10b)$$

where \mathcal{P} denotes the Cauchy principal value. Note that the DC conductivity, σ_{DC} , vanishes for many materials, so that the last term in equation 3.10b is often

neglected. To do this calculation correctly, in principle a measurement over the whole frequency range from zero up to infinity is required. Unavoidably, the finite range of any measurement leads to inaccuracies. Several methods have been suggested to improve the accuracy of the transformation and its convergence [97]. However, even a finite spectral range leads to good results when the main features of the function are captured and proper extrapolations are made. An important condition is that the considered functions decay faster than $1/\omega$ so that $\epsilon_1 \rightarrow 1$ for $\omega \rightarrow \infty$. This behavior corresponds to a driven harmonic oscillator that at large frequencies cannot follow the excitation anymore.

The accuracy of the optical constants derived with the Kramers-Kronig relation is usually comparable to those derived from ellipsometric measurements which critically depend on the choice of the physical model. The Kramers-Kronig relations are therefore extensively used in many areas of spectroscopy, ranging from photoemission and electron energy loss spectroscopy up to high energy particle physics and acoustics.

In our approach, the optical constants of graphene are calculated from the Fano fit to the measured absorbance spectrum shown in section 3.4. That way, the spectral range is extended from the measured range of 1.5 – 5.5 eV to the range 0.5 – 12 eV in which the Fano is considered to be valid, hence improving the accuracy of the deduced optical constants. For the calculation, the infinite integral in equation 3.10a is transformed into a sum over a finite number of N energy increments:

$$\epsilon_1(E) - 1 = \frac{2}{\pi} \Delta E \sum_{k=1}^N \frac{\epsilon_2(k) E(k)}{E(k)^2 - E(j)^2}, \quad (3.11)$$

where the summand for $k = j$ is zero to exclude the pole from the integration. The absorption (or transmission/reflection) curve resulting from a Kramers-Kronig consistent set of optical constants ϵ_1, ϵ_2 is calculated with a transfer matrix method [98]. Based on the Fresnel coefficients, this method describes the propagation of light through a multilayer system as a function of the thicknesses and the optical constants of the individual layers. It has been used already in the early days of graphene to study its visibility on different substrates [63]. In our fitting routine, the optical constants are varied until the absorption spectrum calculated with the transfer matrix method fits the measured curve best. The optical constants derived from the Fano model are shown in figure 3.7. Within the measured wavelength regime, there is a good qualitative agreement with the optical constants of graphene [71, 99] as well as of graphite [84, 100].

Having the optical constants at hand, the response of graphene on an arbitrary substrate can be calculated with the transfer matrix formalism [63]. In this case,

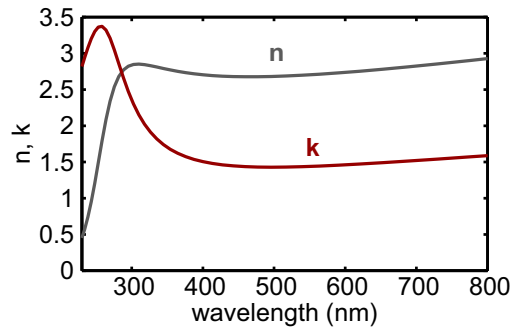


Figure 3.7: The Kramers-Kronig consistent optical constants n and k of graphene derived from the Fano model in the visible and UV wavelength regime.

usually reflectivity contrast measurements are performed as described in section 3.2. The calculations are a simple method to predict the value and spectral dependence of the optical response, giving hence also an estimate of the visibility of the graphene flakes on the substrate. It will be used in chapter 4 where the influence of strain on the optical spectrum is studied. The transfer matrix method is discussed in detail in section 4.3.

EFFECT OF STRAIN ON THE OPTICAL PROPERTIES OF GRAPHENE

In the previous chapter, we have seen that the excitonic Fano resonance arises from the saddle point in graphene's band structure. As long as the overall shape of the band structure is retained, the optical spectrum in this wavelength regime is very robust towards modifications for example due to doping or interlayer interactions. Hence, in order to induce profound changes in the spectrum, the band structure of graphene must be modified. An intriguing possibility to controllably alter the band structure is strain. The effect of strain on graphene's properties is subject of intensive research, mainly with respect to its electronic properties [101]. In this context, the opening of a band gap at the Dirac points has long been discussed [102, 103], but finally shown to be hardly achievable under realistic experimental conditions [104, 105, 106]. Nevertheless, strain engineering is of high interest as it offers to create and tailor local gauge fields [104, 106, 107]. This might even induce a superconducting state in graphene, as is suggested by theory [108]. In practice, the strain dependence of the electrical resistance has been successfully used in sensor applications [109, 110]. With regard to the great potential of graphene for optoelectronic applications such as printable and foldable displays and devices [111, 112], a study of the optical properties of graphene under strain is certainly indispensable.

In this chapter, the effects of uniaxial strain on the optical spectra of graphene will be examined. After introducing the concept of uniaxial strain and discussing the resulting modifications in the band structure (section 4.1), the experimental setup combining reflectivity and Raman measurements is presented in section 4.2. The optical properties of graphene on different flexible substrates are analyzed in the central part of this chapter. In section 4.3, we briefly give an overview of the calculation of optical responses with the transfer matrix method and compare the results from theory and experiment in section 4.4. The amount of strain applied to the samples is quantified from in-situ Raman measurements (section 4.5). Finally, we discuss our results on the behavior of the optical spectrum of graphene under strain in section 4.6.

4.1 UNIAXIAL STRAIN: BREAKING THE SYMMETRY

The most simple way to deform a graphene sheet is to stretch it along one direction, applying uniaxial strain. Most experimental and theoretical studies of graphene under strain consider this deformation method. In contrast to symmetric strain where the symmetry of the lattice remains unchanged, uniaxial strain is asymmetric and breaks the hexagonal symmetry of the lattice.

Considering a graphene sheet as shown in figure 4.1, different distinct directions can be identified. Most prominent are the so-called zigzag (ZZ) and armchair (AC) directions which repeat every 60° due to the hexagonal symmetry. A symmetry breaking in the lattice due to strain at the same time breaks the hexagonal symmetry in the Brillouin zone, where the Dirac points are shifted from the corners of the original hexagon as indicated in figure 4.2a. Obviously, the changes in the BZ and hence the behavior of the electronic states depend critically on the strain direction.

The strain-induced anisotropy in the band structure can be calculated with a modified tight-binding approach [114]

$$H = \sum_{\vec{R}, \vec{\delta}} t(\vec{\delta}) a_{\vec{R}}^\dagger b_{\vec{R}+\vec{\delta}} + \text{h.c.} \quad (4.1)$$

where \vec{R} is the position vector and $\vec{\delta} = \vec{\delta}_{1,2,3}$ the connection of site \vec{R} to the next neighbors. The hopping parameter $t(\vec{\delta})$ reduces to the unperturbed scalar value in the absence of strain. In the linear elastic case, the deformed lattice distances $\vec{\delta}$ are related to the unperturbed ones $\vec{\delta}_0$ by [114]

$$\vec{\delta} = (1 + \bar{\epsilon}) \cdot \vec{\delta}_0. \quad (4.2)$$

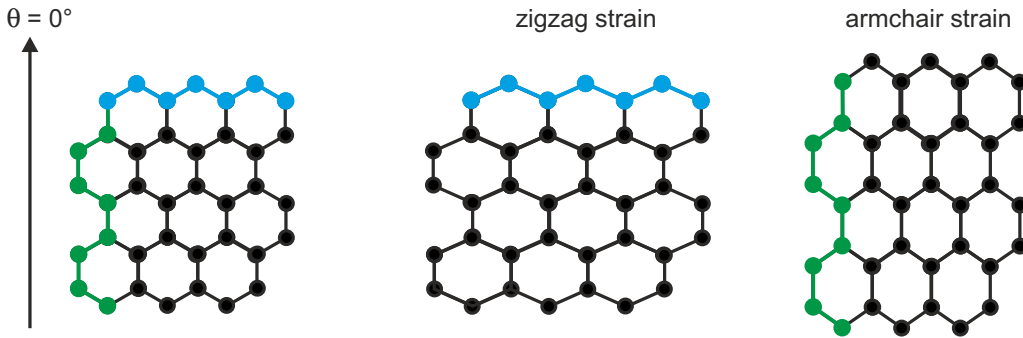


Figure 4.1: Main directions and corresponding strain in the graphene lattice (blue: zigzag direction, green: armchair direction). The strain angle is defined relative to the armchair direction.

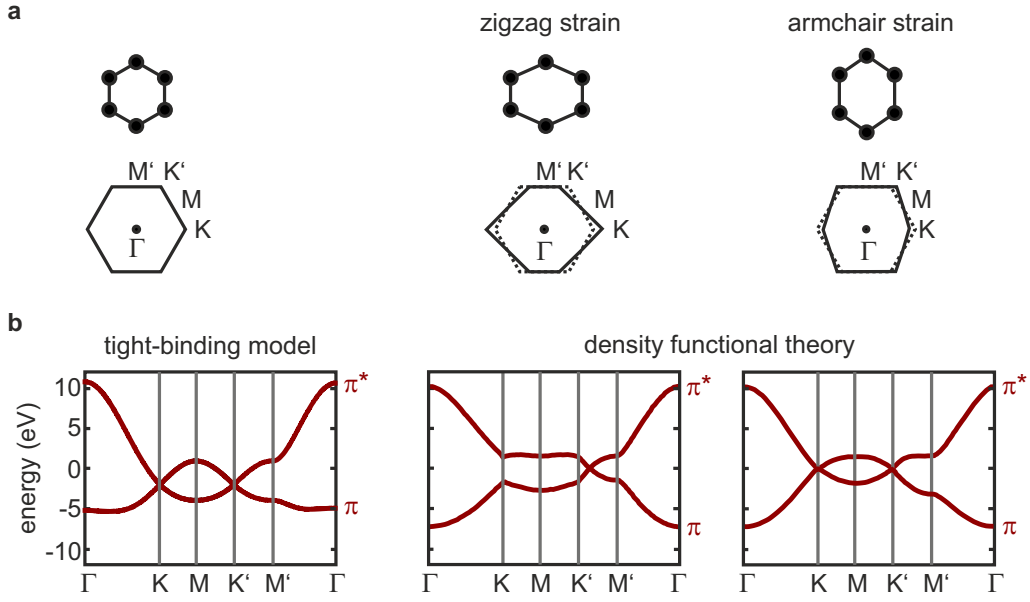


Figure 4.2: a) Graphene lattice under zigzag and armchair strain and induced changes in the band structure. b) Corresponding band structure, calculated with density functional theory for 10% strain compared to the tight-binding model without strain. Shown is a cut along the important points of the unperturbed BZ. Adapted from [113].

$\bar{\epsilon}$ is the strain tensor [115]

$$\bar{\epsilon} = \epsilon \begin{pmatrix} \cos^2 \theta - \nu \sin^2 \theta & (1 + \nu) \cos \theta \sin \theta \\ (1 + \nu) \cos \theta \sin \theta & \sin^2 \theta - \nu \cos^2 \theta \end{pmatrix} \quad (4.3)$$

which depends on the strain angle θ as indicated in figure 4.1. ϵ is the tensile strain applied to the sample. ν is the Poisson's ratio, which is ~ 0.14 for free-standing graphene corresponding to the in-plane Poisson's ratio of graphite [116] or otherwise represents the value of the used substrate when perfect contact is assumed. Of particular interest are the deformed bond lengths for strain along the AC and ZZ direction at $\theta = 0^\circ$ and $\theta = 90^\circ$, respectively:

$$\text{AC: } |\vec{\delta}_1| = |\vec{\delta}_3| = 1 + \frac{3}{4}\epsilon - \frac{3}{4}\epsilon\nu, \quad |\vec{\delta}_2| = 1 + \epsilon \quad (4.4a)$$

$$\text{ZZ: } |\vec{\delta}_1| = |\vec{\delta}_3| = 1 + \frac{3}{4}\epsilon - \frac{1}{4}\epsilon\nu, \quad |\vec{\delta}_2| = 1 - \epsilon\nu \quad (4.4b)$$

The inverse lattice vectors can be calculated with equation 4.4, confirming the above-mentioned shifting of the Dirac points. In addition to the bond deformation, the hopping parameter $t(\vec{\delta})$ changes with strain, but cannot be

straightforwardly determined [114]. Moreover, next nearest neighbor hopping as well as many body effects have been neglected so far.

We therefore draw on calculations performed with density functional theory (DFT) where both next nearest neighbor hopping and many-body effects are included. As an additional benefit, this also allows a prediction of the behavior of the optical spectra under strain (see section 4.6). The results for the band structure from Liang et al. [113] are obtained with DFT in the local-density approximation and are shown in figure 4.2b. The shifting of the Dirac points is well reproduced. What is of special importance regarding the optical spectrum of graphene is the behavior at the saddle points. While neighboring saddle points M and M' are degenerate in the unperturbed case, this degeneracy is lifted for both strain directions. As the transitions at the van Hove singularities are related to the optical absorption, we expect a splitting and shifting of the Fano resonance of graphene in the UV. This chapter aims at the observation of such behavior in the optical spectrum.

4.2 EXPERIMENTAL REALIZATION: REFLECTION AND RAMAN SPECTROSCOPY

Compared to the measurements on free-standing graphene presented in section 3.2, the experimental method needs to be adapted and extended in order to study the strain dependence of the optical spectra. First, we now consider graphene supported on flexible substrates, so that reflectivity instead of transmission is observed. Moreover, a Raman path is added to the setup, allowing to characterize the samples and to monitor perturbations. Finally, a four-point bending device is used to apply uniform uniaxial strain.

4.2.1 Reflectivity setup

The reflectivity experiment has been set up by diploma student Patrick Herlinger, detailed information about the setup and its individual components can be found in his thesis [117]. A simplified sketch of the setup is shown in figure 4.3.

The white light source (Ocean Optics DH-2000) consists of a combined tungsten and halogen lamp, providing light with photon energies between 1.5 and 5.5 eV. The most critical component is the beamsplitter as our measurements require a constant splitting ratio over the whole energy range. Here, a customized

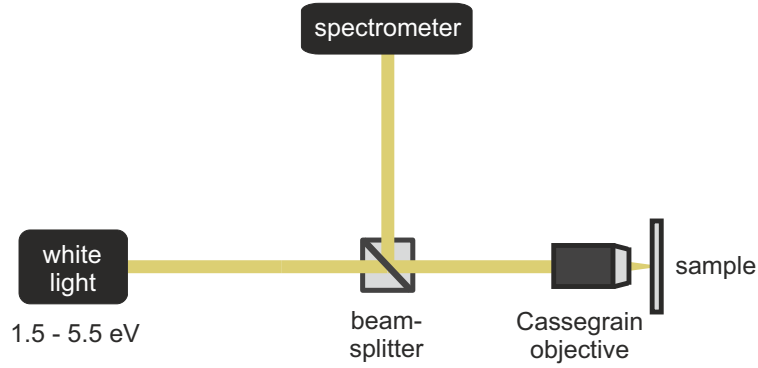


Figure 4.3: Schematic overview of the reflectivity setup.

all-dielectric 50:50 beam splitter (Cascade Optics) proved to be the best choice with regard to spectroscopy as well as imaging applications. The all-reflective Cassegrain objective (Davin Optronics 74x) now focuses and recollects the reflected light. To navigate and position the white light spot on the sample, a home-built wide field microscope unit can be integrated into the setup when necessary. Spectral analysis is done with a monochromator (Princeton Instruments Acton SP2500) equipped with a UV-enhanced CCD camera (Princeton Instruments Pixis 100). The complete spectrum is merged from two exposures with different gratings covering the UV and the visible wavelength regime, respectively.

As mentioned in section 3.2, the reflectivity of the graphene flakes is given in analogy to transmittance by

$$R = \frac{R_g - R_s}{R_s} \quad (4.5)$$

corresponding to the reflection contrast between the supported graphene flake (R_g) and the bare substrate (R_s). Again, this normalization eliminates the intrinsic spectral dependencies of the setup.

4.2.2 *In-situ Raman measurements*

To characterize the measured samples as well as to monitor eventual perturbations, a Raman path is included in the existing setup. Here, an in-situ implementation as shown in figure 4.4 is desirable. This permits to quickly switch between the reflectivity and the Raman measurement mode by inserting and removing a flip mirror while the sample does not have to be moved.

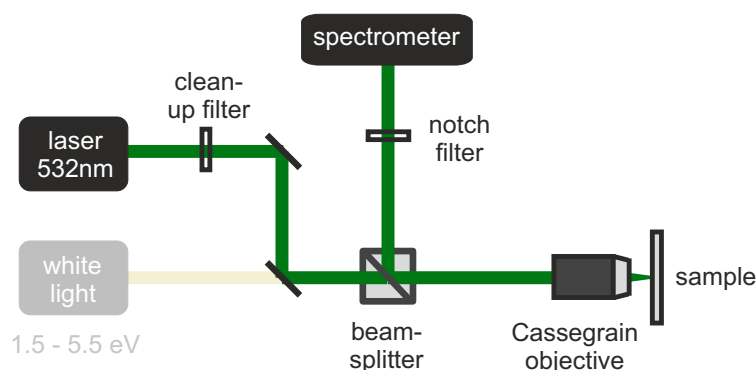


Figure 4.4: Implementation of the in-situ Raman characterization method.

The intensity of the scattered Raman light increases with decreasing wavelength λ_0 of the excitation light as $I \propto 1/\lambda_0^4$. However, for excitation at blue wavelengths, the absorption of graphene and potentially also the substrate increases so that the samples heat up more easily. Moreover, usually a larger fluorescence background is observed in this case. As a compromise and due to availability, we use a pump laser (Coherent Verdi V8) at a wavelength of 532 nm. This laser provides very stable and narrow-linewidth output which is essential for Raman measurements. To avoid heating-induced shifting of the Raman peaks, the laser power on sample is kept below 2 mW. Behind the laser, a clean-up filter (Semrock HC Laser Clean-up MaxLine 532/2) transmits light at 532 nm

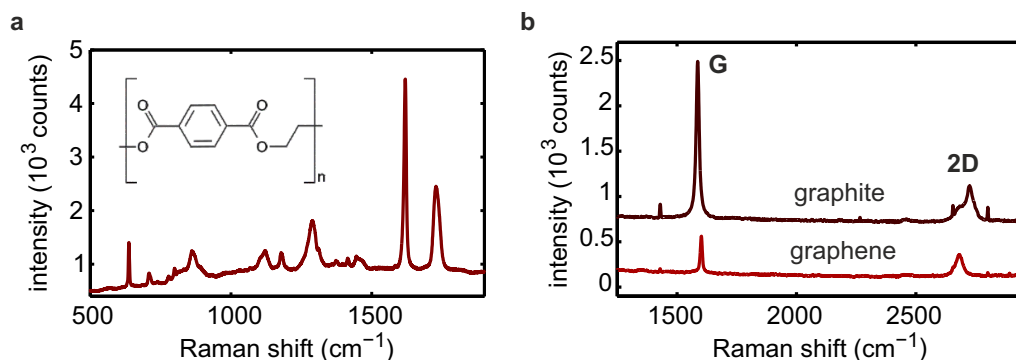


Figure 4.5: a) Raman spectrum of a bulk PET sample. The inset shows the fundamental building block of the polymer. The most prominent peaks at 1300 cm^{-1} , 1615 cm^{-1} , and 1730 cm^{-1} correspond to C–O stretching, breathing of the ring, and stretching of the C=O double bond. b) Raman spectra of graphite and graphene on quartz. The G and 2D modes can be identified at $\sim 1650\text{ cm}^{-1}$ and $\sim 2700\text{ cm}^{-1}$, respectively, and show the expected line shapes.

only. A very steep Notch filter (Semrock Single Notch Filter 532/17 – U grade) blocks the excitation light and allows the observation of the Raman lines that are shifted to higher and lower energies.

The intensity ratio of these so-called Stokes and Anti-Stokes lines is given by the occupation probabilities n of the initial states which follow a Boltzmann distribution:

$$\frac{I_{AS}}{I_S} = \frac{n(\nu = 1)}{n(\nu = 0)} = \exp\left(-\frac{h\nu_m}{kT}\right) \quad (4.6)$$

At room temperature and for a mode energy of $\nu_m = 1000 \text{ cm}^{-1}$, this gives a value of $e^{-5} \approx 0.7\%$. In our experiments, we hence observe the redshifted Stokes lines only. To get an overview of the whole relevant wavenumber regime, a low-resolution grating with 150 1/mm is used in the spectrometer, while a grating with 1800 1/mm yielding a high resolution of $\sim 1 \text{ cm}^{-1}$ is used to monitor the individual Raman lines.

To check the performance of our Raman setup, we first take a Raman spectrum of a PET block as shown in figure 4.5a. We observe good agreement with literature data (see for example [118]) and can even assign the individual peaks to different vibrational modes. As a next step, we measure exfoliated graphene on a quartz substrate, which has the advantage that quartz itself does not exhibit Raman modes in the considered energy regime. The resulting spectra of multi- and monolayer graphene are shown in figure 4.5b. The position as well as the line shape of the G and 2D mode agree well with the reference spectra (see figure 2.7b), proving the performance of our in-situ Raman measurements.

4.2.3 How to apply strain: bending method

To complete our experimental setup, we need a method to apply strain to the samples. Our experiment imposes several conditions on the straining device:

- we need uniform strain over an area of $10 \times 10 \text{ mm}^2$,
- the amount of strain should be controllable and ideally reach values up to about 5%,
- accessibility with the Cassegrain objective (working distance 1 mm, diameter $\sim 30 \text{ mm}$) is crucial.

To meet these requirements, we developed a four-point bending device as shown in figure 4.6a. Bending has the advantage that it can easily be implemented in the experiment. As the bending radius is always large compared to the size of

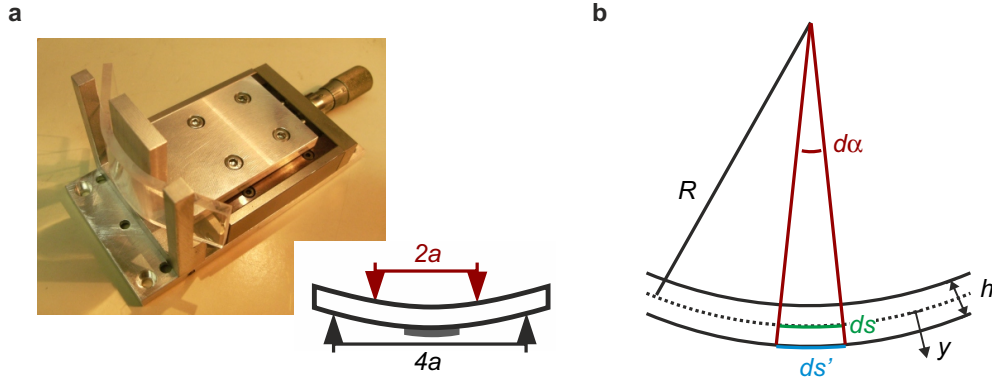


Figure 4.6: a) Strain is applied to the sample (3 mm thick PET block) with a four-point bending device ($a = 1$ cm). The outer pins (black) are fixed while the inner pins (red) are moveable with the linear stage (25 mm travel). b) Important parameters for beam bending theory, allowing to estimate the amount of strain applied to the sample. R is the bending radius, h the sample thickness, $d\alpha$ the central angle, and ds/ds' the neutral/deformed length element.

the flakes, out-of-plane curving can be neglected, so that the applied strain is uniaxial. Four-point bending is advantageous as it results in a uniform amount of strain between the two inner pins. The exact position of the graphene flake on the substrate is then less critical. The distance between the outer pins is 4 cm, which ensures accessibility with the objective.

The amount of strain that is applied to the samples can be calculated from beam theory [119]. The relevant parameters are given in figure 4.6b. When the sample is bent, strain increases linearly from the inner side with compressive strain ($\epsilon < 0$) to the outer side with tensile strain ($\epsilon > 0$). The so-called neutral fiber at $h/2$ does not change its length $ds = R d\alpha$, while the outer fiber is stretched to $ds' = (R + y) d\alpha$. Consequently, the tensile strain is

$$\epsilon = \frac{ds' - ds}{ds} = \frac{y}{R}. \quad (4.7)$$

For our four-point bending device with a travel l of the inner pins, the strain can be estimated from [120]

$$\epsilon = \frac{y}{R} = \frac{3ly}{4a^2}. \quad (4.8)$$

For $a = 1$ nm and a 1 mm thick sample, 5% strain correspond to a travel of $l \approx 13$ mm while for a 5 mm thick sample, the minimum step size of $\Delta l = 0.05$ mm still gives good controllability of the strain with $\Delta\epsilon \approx 0.1\%$. The bending device hence meets all the requirements.

4.3 CALCULATION OF THE OPTICAL RESPONSE OF MULTILAYER SYSTEMS WITH A TRANSFER MATRIX FORMALISM

In section 3.6, we have seen that the optical constants of graphene in the considered wavelength regime can be derived from the Fano fit to the absorption spectrum with the help of the Kramers-Kronig relations. The general optical response of graphene embedded in a multilayer system can be calculated with a transfer matrix formalism that is based on the Fresnel coefficients. The number, order, and thickness of the layers can be easily varied while only the optical constants of the individual layers need to be known. In the following, we will give a short overview over the formalism, a more detailed description can be found for example in [98].

Basically, the approach treats two phenomena separately and combines them by matrix multiplication. First, light is refracted and partially reflected at each interface. The electric field in each layer can be split into two components E_i^+ and E_i^- for the light travelling to left and to the right, respectively (considering a vertical interface and light travelling from left to right). The electric fields on the two sides i and j of the interface are linked via the interface transition matrix

$$\overline{\overline{T}}_{ij} = \frac{1}{t_{ij}} \begin{pmatrix} 1 & r_{ij} \\ r_{ij} & 1 \end{pmatrix} \quad (4.9)$$

as

$$\begin{pmatrix} E_i^+ \\ E_i^- \end{pmatrix} = \overline{\overline{T}}_{ij} \begin{pmatrix} E_j^+ \\ E_j^- \end{pmatrix}. \quad (4.10)$$

The Fresnel coefficients for reflection r_{ij} and transmission t_{ij} for normal incidence depend on the refractive index n of the layers and are given by

$$r_{ij}^s = -r_{ij}^p = \frac{n_i - n_j}{n_i + n_j} \quad (4.11a)$$

$$t_{ij}^s = t_{ij}^p = \frac{2n_i}{n_i + n_j}. \quad (4.11b)$$

s and p indicate the components for polarization perpendicular and parallel to the plane of incidence, respectively. Second, the propagation of the light through the individual layers must be taken into account. The layer propagation matrix for layer j with thickness d_j is

$$\overline{\overline{P}}_j = \begin{pmatrix} e^{-i\beta_j} & 0 \\ 0 & e^{i\beta_j} \end{pmatrix} \quad (4.12)$$

with

$$\beta_j = \frac{2\pi}{\lambda} n_j(\lambda) d_j. \quad (4.13)$$

The response of a multilayer is then calculated by multiplying the electric field vector of the incoming light with the propagation and interface matrices of the individual layers. This multiplication can be condensed into a single transfer matrix $\overline{\overline{M}}$. The total reflection and transmission coefficients are simply given by

$$r = \frac{M_{12}}{M_{22}} \quad \text{and} \quad t = \frac{1}{M_{22}}, \quad (4.14)$$

yielding the reflection $R = |r|^2$ and transmission $T = \gamma |t|^2$, where $\gamma = n_N/n_1$ for a system of N layers. Note that absorption $A = 1 - T - R$ occurs in the presence of absorbing layers with non-zero imaginary part of the refractive index. This method allows also the quick estimation of contrast signals by calculating two systems that differ in one layer only.

In the next section, the transfer matrix method based on the optical constants of graphene derived from the Fano fit is used to calculate the reflectivity of graphene on different substrates.

4.4 VISIBILITY AND RAMAN SPECTRUM ON VARIOUS SUBSTRATES

Regarding the strain experiments, we would like to measure the optical spectrum of graphene on a flexible substrate. Here, different choices are possible but several aspects must be taken into account and verified before strain is applied. An obvious choice for a flexible substrate are plastics, i. e. polymers like PET (poly(ethylene terephthalate)) or PMMA (poly(methyl methacrylate), plexiglas). Also very thin glass substrates with a thickness of 50 or 100 μm offer sufficient flexibility. Last, PDMS (polydimethylsiloxane) combines high flexibility with stickiness, hence promising good adhesion.

The graphene transfer process as described in section 2.3 suggests the removal of the PMMA transfer membrane with acetone as the last transfer step. This is not possible with the polymer substrates as they would be damaged and partially dissolved. On the other hand, the presence of the membrane causes unwanted interference effects in the spectra. As an alternative to transfer, graphene can be exfoliated directly on the plastic substrates. Especially when no marker system is available, it is crucial to check if the visibility of the flakes on the considered substrate is high enough. In addition to visibility, the shape of the optical

spectrum must allow the observation of changes in the vicinity of the saddle point transition, i. e. at about 290 nm. Moreover, the Raman spectrum on the considered spectrum must be conclusive. The Raman lines of graphene should not be hidden behind substrate modes or a large luminescence background.

The reflectivity and Raman spectra of graphene on different substrates are summarized in figure 4.7 and will now be discussed individually. All samples have been fabricated by direct exfoliation of graphene without a transfer process. Thin glass (Schott D263Teco 100 μm), PMMA (Evonik Plexiglas Foil 0.375 mm), and PET (Mitsubishi Hostaphan 350 μm) substrates have been purchased while the PDMS is fabricated from raw materials in-house (Dow Corning Sylgard184 Kit). The measured reflectivity spectra are compared to calculations with the transfer matrix code using tabulated data [121, 122] for the optical constants of the substrates. Although the polymers show a variety of Raman modes, identification of the G and 2D peaks of graphene is still possible.

i) Thin glass:

As shown in figure 4.7a, the Fano resonance is retained in the optical spectrum of graphene on the glass substrate. The reflectivity reaches a maximum value of about 35% and decreases to about 8% in the visible region, which is sufficient to identify monolayer flakes. Regarding the Raman spectrum in figure 4.7e, the Raman modes of graphene can be easily identified as the glass shows no lines itself. The glass substrate is hence well suited for the strain application.

ii) PMMA:

Also on the PMMA substrate, a Fano lineshape is observed in the reflectivity spectrum shown in figure 4.7b. The maximum reflectivity is about 30% while the visibility at green and red wavelengths is about 10%. The Raman spectrum in figure 4.7f exhibits a variety of modes. Although most arise from the substrate, the Raman lines of graphene can still be identified at the expected wavenumbers as indicated. Therefore, also PMMA complies with the conditions.

iii) PET:

Regarding the reflectivity spectrum of graphene on PET shown in figure 4.7c, a different behavior is observed. The original Fano lineshape is modulated with a maximum reflectivity of only 8% and drops below 4% at visible wavelengths. This behavior is due to the non-negligible absorption of PET, which renders an identification of graphene flakes almost impossible. Moreover, it hampers the observation of strain-induced changes in the reflectivity spectrum. Also the

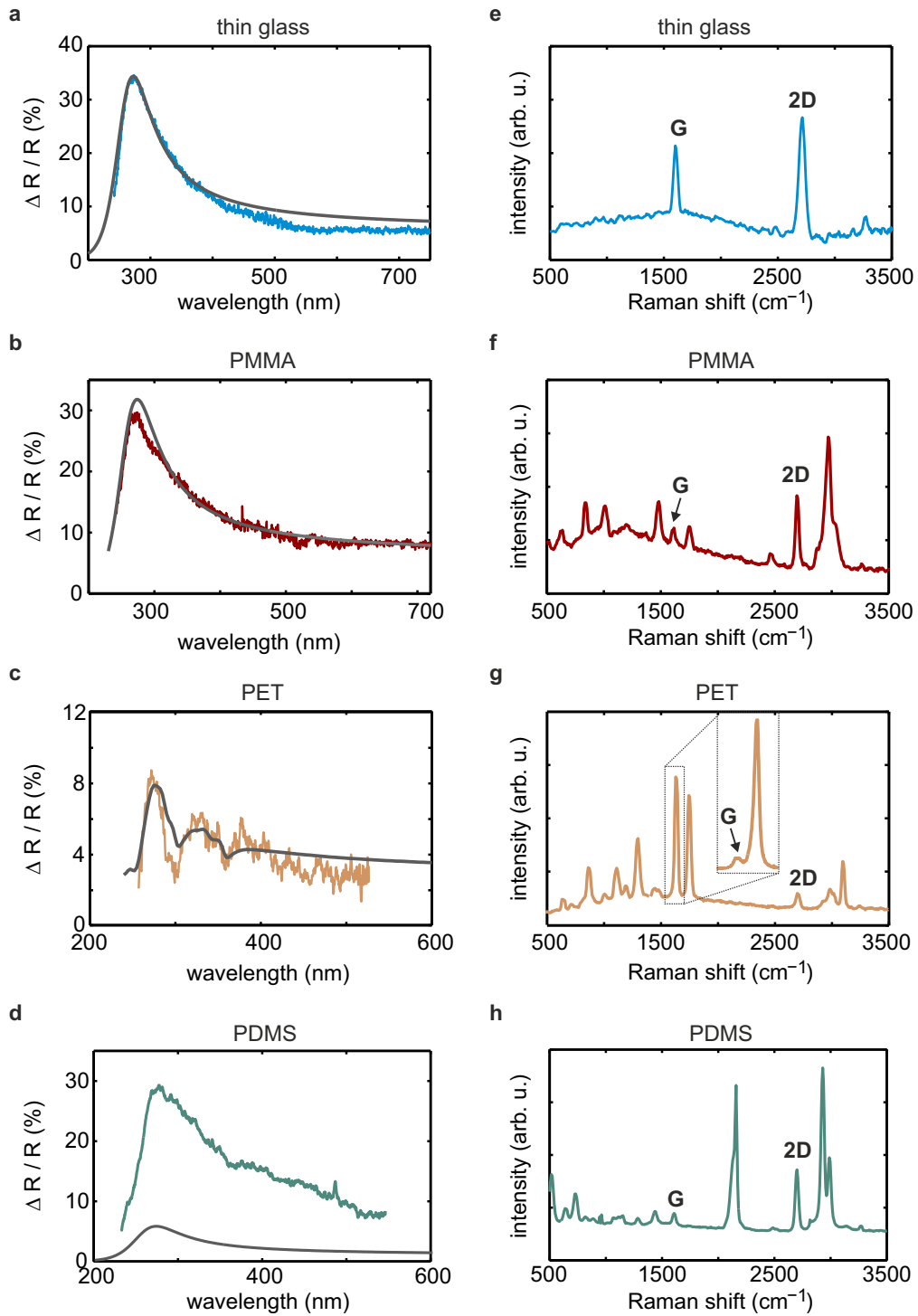


Figure 4.7: **a-c)** Calculated and measured reflectivity of graphene on different substrates: **a)** glass, **b)** PMMA, **c)** PET and **d)** PDMS. **e-h)** Corresponding Raman spectra.

Raman spectrum in figure 4.7g is more complex. While the 2D mode can be easily identified, the G mode is found in the flank of a PET Raman mode. Overall, PET as substrate material is not a good choice due to the distorted reflectivity spectrum with weak visibility.

iv) PDMS:

As shown in figure 4.7d, the Fano resonance in the reflectivity spectrum is again retained on the PDMS substrate. Maximum value and visibility are comparable to those obtained with glass and PMMA. In the Raman spectrum in figure 4.7h, the graphene modes can be clearly identified. The PDMS substrate seems to be applicable in the strain experiments.

There is a good agreement between the measured reflectivity spectra and the spectra calculated with the transfer matrix formalism for glass, PMMA, and PET. This is essential in order to analyze the strain-induced changes in the spectra, i.e. in the optical constants of graphene. Regarding PDMS, although the overall shape agrees well, the reflectivity is considerably underestimated. In contrast to the other substrates, the optical constants here depend critically on the exact recipe and raw materials used to fabricate the PDMS. It seems that the values found in the literature [122] are not appropriate here. Due to the good quality of the signals, the PDMS substrate will still be considered in the further experiments.

4.5 QUANTIFYING STRAIN WITH RAMAN SPECTROSCOPY

After having studied which substrates are suitable for the investigation of strain on the optical properties of graphene, strain can be applied in a next step. The amount of strain on the samples can be estimated from beam bending theory as described in section 4.2 (see equation 4.8). However, one cannot safely assume perfect adhesion of the flakes to the substrates. It is thus indispensable to have a reference measurement that directly quantifies the amount of strain applied to the graphene flakes. Here, Raman spectroscopy offers the possibility to not only characterize the samples but has been shown to represent a reliable strain gauge [116]. Conveniently, it at the same time allows to determine the crystallographic orientation of the graphene flakes when the crystal symmetry is broken by strain [123].

4.5.1 Strain dependence of the Raman modes

When graphene is subject to tensile strain, in general a redshift of the phonon modes is observed, i. e. a phonon softening [103, 116, 123]. This can be explained by the elongation of the carbon–carbon bonds due to the stretching, which leads to a bond weakening and hence a lower vibrational frequency [103]. The rate of the shift depends on the anharmonicity of the interatomic potentials [123] and is quantified by the Grüneisen parameters γ and β for hydrostatic and shear deformation, respectively [124].

For the doubly degenerate E_{2g} phonon which gives rise to the G mode, they are given by

$$\gamma_{E_{2g}} = -\frac{1}{\omega_{E_{2g}}^0} \frac{\delta\omega_{E_{2g}}^h}{\delta\epsilon_h} \quad \text{and} \quad \beta_{E_{2g}} = \frac{1}{\omega_{E_{2g}}^0} \frac{\delta\omega_{E_{2g}}^s}{\delta\epsilon_s} \quad (4.15)$$

where the indices h and s mean hydrostatic and shear, respectively. The overall behavior of the E_{2g} mode under uniaxial strain is described by [116]

$$\begin{aligned} \Delta\omega_{G^\pm} &= \Delta\omega_{E_{2g}}^h \pm \Delta\omega_{E_{2g}}^s \\ &= -\omega_G^0 \gamma_{E_{2g}} (1 - \nu) \epsilon \pm \frac{1}{2} \omega_G^0 \beta_{E_{2g}} (1 + \nu) \epsilon \end{aligned} \quad (4.16)$$

in dependence of the Poisson's ratio ν and the applied strain ϵ . This corresponds to a shifting and a splitting of the G peak into two subbands named G^+ and G^- . The behavior of the 2D mode is in general more complex as it is affected by any change in the band structure in contrast to the zone center only in case of the G mode. This can lead to peak broadening and splitting [65].

Several groups have published their results on the strain dependence of the Raman modes of graphene. We trust the study of Mohiuddin et al. [116] because it on the one hand represents the most complete and reliable investigation and on the other hand constitutes the highest values for the shifting of the modes. Moreover, a similar measurement method is used. Their results will therefore serve as a reference for our measurements. We suspect, as will also be the case in our experiments later in this section, that adhesion is not perfect in the other experiments, which leads to an overestimation of the applied strain. Mohiuddin et al. [116] obtain values of $\sim -64 \text{ cm}^{-1}/\%$ for the shifting of the 2D mode with increasing strain and $\sim -10.8 \text{ cm}^{-1}/\%$ and $\sim -31.7 \text{ cm}^{-1}/\%$ for the G^+ and G^- modes, respectively. For a Poisson's ratio of $\nu = 0.33$ (graphene on PET), this corresponds to Grüneisen parameters of $\gamma_{E_{2g}} = 1.99$ and $\beta_{E_{2g}} = 0.99$, which agrees well with first-principles calculations [116].

In a next step, we would like to see the effect of strain on the Raman spectrum of graphene in our experiment. According to the outcome of the last section, substrate materials to be considered here are thin glass, PMMA, and PDMS. In the following, the results of the individual measurements are summarized and compared to the reference. The intensity ratio and the exact position of the Raman peaks depends on the used substrate [65]. As we do not consider absolute intensities or peak positions, this does not restrict the applicability of our strain calibration method.

i) Thin glass:

The 2D Raman peak of graphene on glass is shown in figure 4.8a. When the substrate is bent, strain should be applied and a shifting of the Raman peak is expected. However, no shifting of the 2D peak position is observed as indicated by the red data points in figure 4.8b. As the Poisson's ratio of glass $\nu = 0.2$ [125] is smaller than that of PET used in the reference, the resulting shift per 1% strain should be less distinct but still clearly visible. We therefore conclude that the adhesion of the flake to the substrate is weak so that no strain is actually applied to the graphene. To improve the contact, gold bars are fabricated with electron beam lithography to clamp the flake to the substrate as shown in figure 4.9. Data points measured on the clamped structure are indicated as black crosses in figure 4.8b. Strikingly, also this method does not yield an im-

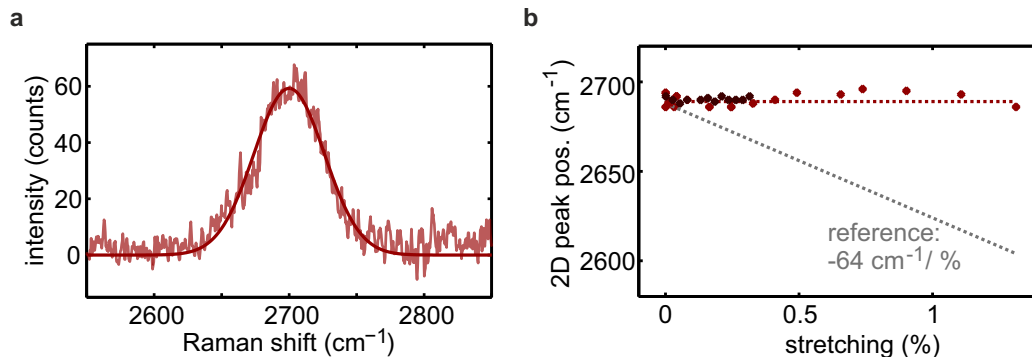


Figure 4.8: **a)** 2D Raman peak of graphene on a thin glass substrate measured with a high-resolution grating, integration time 10 min, binning 4 pixels. The peak position can be extracted from a Lorentzian fit (dark red line). **b)** While the reference predicts a strong shifting of the 2D mode with increasing strain (grey dashed line), no change in the peak position is observed here (red dashed line). Red crosses mark data points where the flake is clamped while black crosses indicate measurements without clamps. Stretching corresponds to the nominal value of strain calculated from equation 4.8.

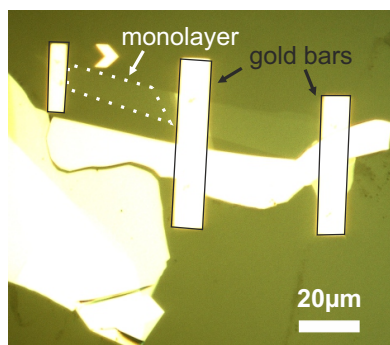


Figure 4.9: Microscope image of a monolayer graphene flake on glass, clamped with gold bars fabricated by electron beam lithography to improve the adhesion.

provement. Commonly, thin glass substrates are provided by the manufacturer with a layer preventing adhesion between individual substrates. We suspect that this layer has not been completely removed in our standard cleaning process involving acetone and isopropanol baths. Unfortunately, more intense treatment, for example with ultrasound, is not possible here as the ultrathin substrates are very fragile. This sample geometry will therefore not be considered further.

ii) PMMA:

The Raman spectra of graphene on PMMA for different degrees of bending are shown in figure 4.10a and c. Clearly, a shifting to lower frequencies is observed for both the G and the 2D mode. The position of the respective peaks obtained from a Lorentzian fit to the spectra is plotted in dependence of the nominal strain in figure 4.10b and d. From a linear fit to the data points, we find a shift of $\sim -52 \text{ cm}^{-1}/\%$ for the 2D mode and $\sim -25 \text{ cm}^{-1}/\%$ for the G mode. Considering the Poisson's ratio $\nu = 0.36$ of PMMA [126], these values do not reach those of the reference ($\sim -64 \text{ cm}^{-1}/\%$ (2D) and $\sim -32 \text{ cm}^{-1}/\%$ (G^-)). The reference values fit excellently to the measured data when an offset of 0.18% is assumed in the stretching (see dashed lines). We attribute this to an error in the adjustment of the zero position of the straining device. Overall, comparing our measurements to the reference, we achieve almost 0.6% strain on the graphene sample using a PMMA substrate. Repeated up- and down-cycling of the stretching did not result in major deviations or hysteresis so that this method is very reliable (see figure 4.10b and d). It is noteworthy that the G^+ mode seems to be suppressed in our experiments, as the spectra can always be fitted with a single Lorentzian line only and its position agrees well with the G^- mode. We think this could be due to the substrate choice and refer to other measurements where also no splitting was

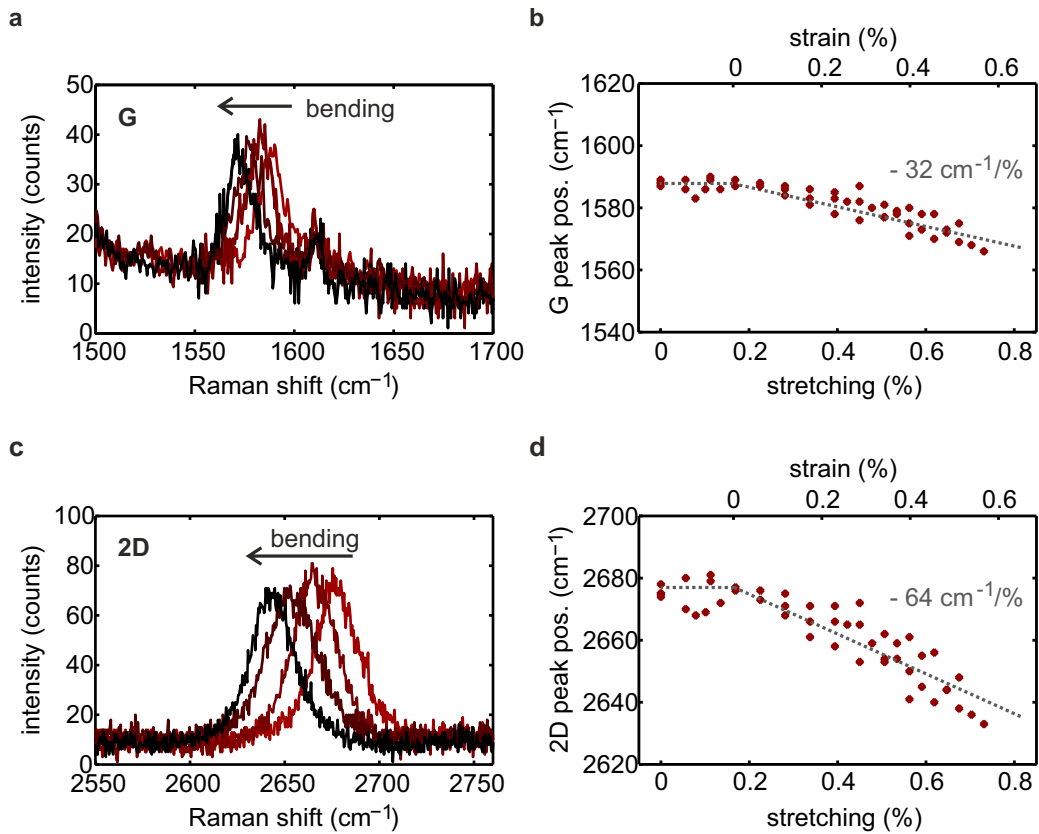


Figure 4.10: Behavior of the Raman modes of graphene on PMMA with strain. **a, c)** G and 2D mode measured with the high-resolution grating for increasing bending, integration time 12 min. **b, d)** Shifting of the G and 2D mode obtained from repeated stretching and relaxing with linear fits (light gray dashed lines). Peak positions are again extracted from Lorentzian fits to the spectra. Assuming an offset of 0.18% in the stretching, the slope of the linear fits is in excellent agreement with the reference (dark gray dashed lines). This offset directly gives the strain values (top axis).

observed [103]. Nevertheless, this does not limit our strain calibration method as the G^- and 2D mode show the expected behavior.

iii) PDMS:

At last, we investigate the strain dependence of the Raman modes of graphene on a PDMS substrate. Also here, clearly an effect is visible as shown in figure 4.11a and c. While the 2D mode is redshifted, here we see a shifting and also a splitting of the G mode. However, in the plot of the peak positions over the stretching a nonlinear behavior arises, see figure 4.11b and d. Although some stretching steps result in a considerable peak shift, other data points indicate a backshifting towards the original peak position. Apparently the PDMS relaxes in a nonlinear way, which is also confirmed by the observation of a distinct drift of the focus during the measurements. Due to this nonlinearity, we deduce the

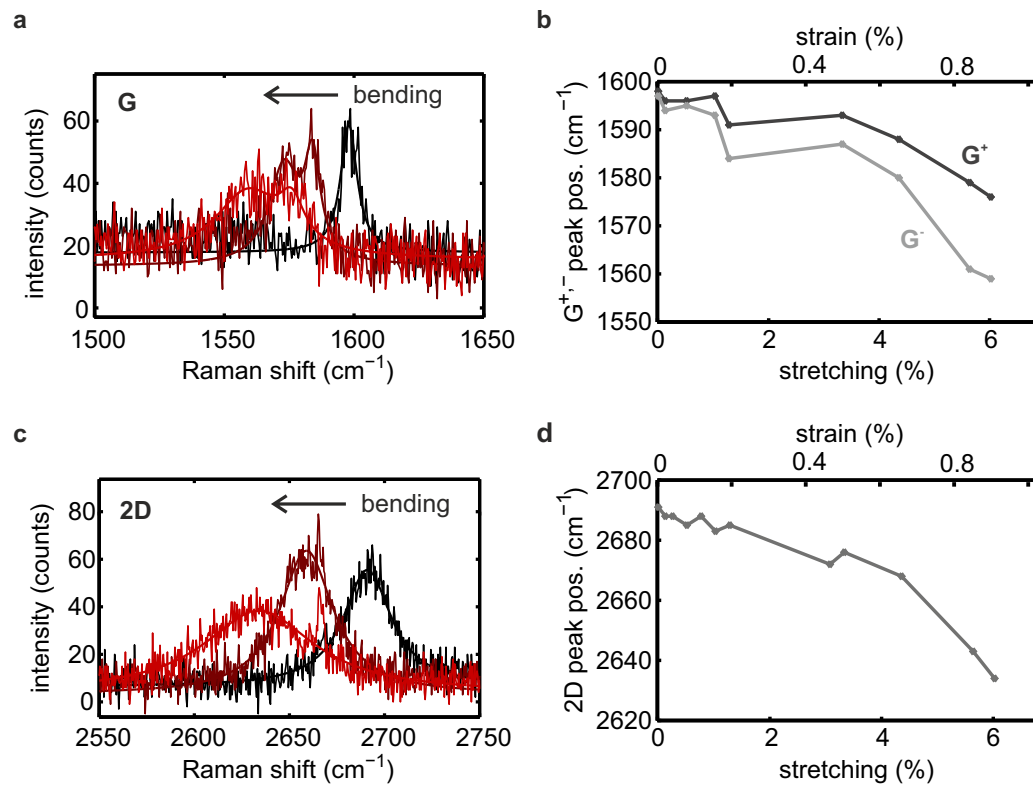


Figure 4.11: Strain-induced changes in the Raman modes of graphene on PDMS. **a)** Splitting and shifting of the G mode with Lorentzian fits. **b)** Shifting of the G^+ and G^- modes. **c)** 2D mode. **d)** Shifting of the 2D mode with Lorentzian fits. In **b)** and **d)**, the applied strain has been calculated from the shifting of the peaks due to the nonlinear behavior.

applied strain directly in comparison to the reference, as shown in the top axis of the plots. We neglect the influence of the Poisson's ratio which is slightly higher here $\nu=0.5$ [126] and emphasize that this method is not accurate, but still allows a rough estimate of the applied strain. That way, we see that up to $\sim 0.9\%$ strain can be applied with the PDMS substrate.

In summary, our experiments indicate missing adhesion of graphene on the thin glass substrates, so that this sample geometry will not be considered in the following. In case of the PMMA and PDMS substrates, we successfully verified that strain is applied to the graphene flakes with the help of in-situ Raman measurements. Moreover, the amount of strain can be quantified when the spectra are compared to a reference measurement. While PMMA sample gives a very reproducible behavior with a maximum strain of $\sim 0.6\%$, the PDMS sample shows a nonlinear behavior but allows slightly higher strain values up to $\sim 0.9\%$. These results constitute a good basis to study the effects of strain on the excitonic Fano resonance of graphene in the following section.

4.5.2 Determination of the lattice orientation

In the investigation of the effect of strain on the optical spectrum of graphene, we will see later (section 4.6) that the behavior depends on the orientation of the graphene lattice relative to the stretching direction. The crystal orientation of strained graphene can be determined from the polarization dependence of the Raman peaks, which will be shown in the following at the example of the sample with graphene on PMMA.

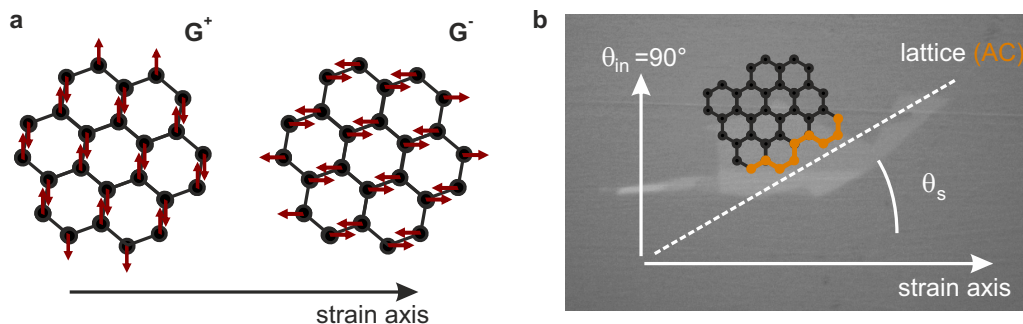


Figure 4.12: **a)** Orientation of the G^+ and G^- modes relative to the strain axis. **b)** Definition of the strain axis with respect to the armchair direction in the graphene lattice. In our experiment, the polarization of the excitation light is perpendicular to the strain axis. The image shows the actually measured flake.

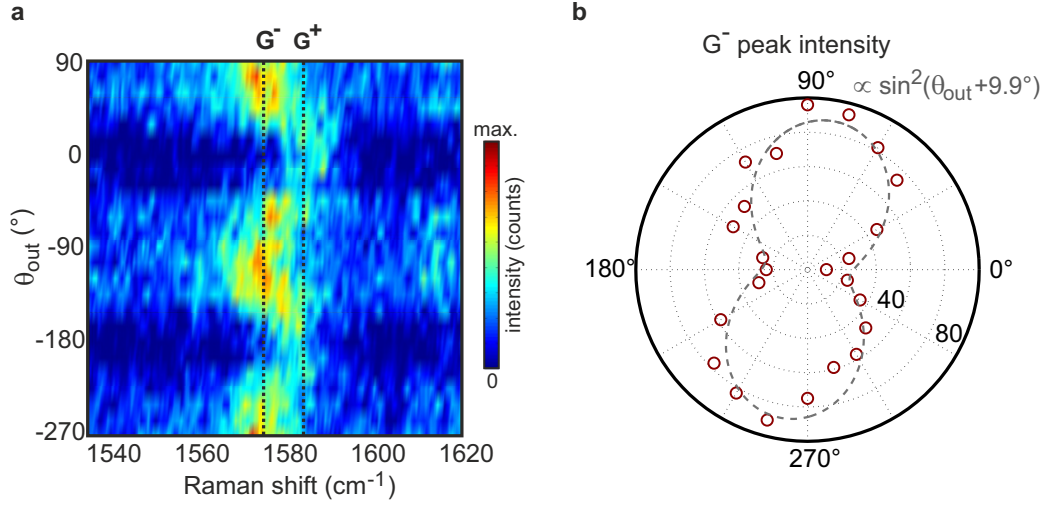


Figure 4.13: a) Polarization dependence of the G^+ and G^- Raman modes: the excitation polarization is kept constant (perpendicular to the strain axis) and the polarization of the scattered light is probed with an analyzer. Step size is 15° , integration time 15 min per spectrum. b) Polar plot of the intensity of the G^- mode (sum over 5 cm^{-1} to reduce noise) with a \sin^2 fit from which the strain angle can be determined.

Above we have seen that the G mode exhibits a splitting into two subbands when strain is applied. As is shown in figure 4.12a, this is due to the orthogonal phonon displacements: the displacement regarding the G^+ mode is perpendicular to the strain axis, whereas it is parallel in case of the G^- mode [116]. The emission probability of these phonons depends on the excitation polarization θ_{in} , the analyzer polarization θ_{out} , and the strain angle θ_s as defined in figure 4.12b. While the angles $\theta_{\text{in, out}}$ are known with respect to the strain axis, the angle θ_s between strain axis and crystallographic axis (armchair direction) is unknown. It can however be determined from the polarization dependence of the intensity of the G^\pm modes, which is given by [123]

$$I(G^-) \propto \sin^2(\theta_{\text{in}} + \theta_{\text{out}} + 3\theta_s) \quad (4.17a)$$

$$I(G^+) \propto \cos^2(\theta_{\text{in}} + \theta_{\text{out}} + 3\theta_s) \quad (4.17b)$$

The factor of three for the strain angle arises from the symmetry of the lattice.

In our Raman experiments, the orientation of the excitation polarization is fixed and perpendicular to the strain axis, so that $\theta_{\text{in}} = 90^\circ$. The strain angle can hence be directly extracted from a measurement of the analyzer polarization dependence of the G^\pm modes as shown in figure 4.13a. We observe a clear \sin^2 behavior of the G^- mode. Also the G^+ mode is now observed, however,

it is still very weak and its polarization dependence cannot be evaluated as the signal barely exceeds the noise. Figure 4.13b shows a polar plot of the intensity of the G^- mode with a \sin^2 fit. From the fit, we obtain the strain angle $\theta_s = \frac{1}{3}(9.9^\circ - \theta_{in}) = -26.7^\circ$ which is very close to the zigzag direction at an angle of 30° relative to the armchair direction.

4.6 EFFECT OF UNIAXIAL STRAIN ON THE EXCITONIC FANO RESONANCE

In this last section, we will investigate the strain-dependence of the optical spectrum of graphene in the visible and ultraviolet wavelength regime. Before we present and discuss our experimental results, we consider the predictions from theory in order to get a feel for the expected behavior.

4.6.1 Theoretical predictions

In section 4.1, we have seen that strain has intriguing effects on the electronic band structure of graphene. Of special importance regarding the optical spectrum in the visible and ultraviolet regime are the induced changes in the vicinity of the saddle point. We showed that the symmetry breaking in the lattice lifts the degeneracy between neighboring M and M' points (see figure 4.2).

A summary of the simulated optical spectra for the different strain and polarization directions by Liang et al. [113] is shown in figure 4.14. Their computational approach starts from the electronic band structure of strained graphene obtained with density functional theory as shown in figure 4.2. The absorption spectrum is then calculated from the electron-hole excitations of the two-particle Green's function and the transition matrix element [127], so that excitonic effects are included. Alternatively, a single-particle Green's function delivers the spectra without electron-hole contributions. Figure 4.14a shows the optical spectrum of pristine graphene without strain. It corresponds to the spectrum obtained by Yang et al. [73] which is in excellent agreement with the experimental results [31, 70] as presented in chapter 3. The absorbance spectra with 10% strain for zigzag and armchair polarization are shown in figure 4.14b-e. Regarding excitation polarized parallel to the zigzag direction (b and d), no splitting of the absorption peak is observed. This is in contrast to armchair polarization where the expected splitting related to transitions at M and M' points is clearly visible (c and e). The strong polarization dependence is explained by the symmetry of the wave functions at M and M', leading to a suppression of the transitions at M' for zigzag polarization [113]. All absorption peaks are considerably redshifted

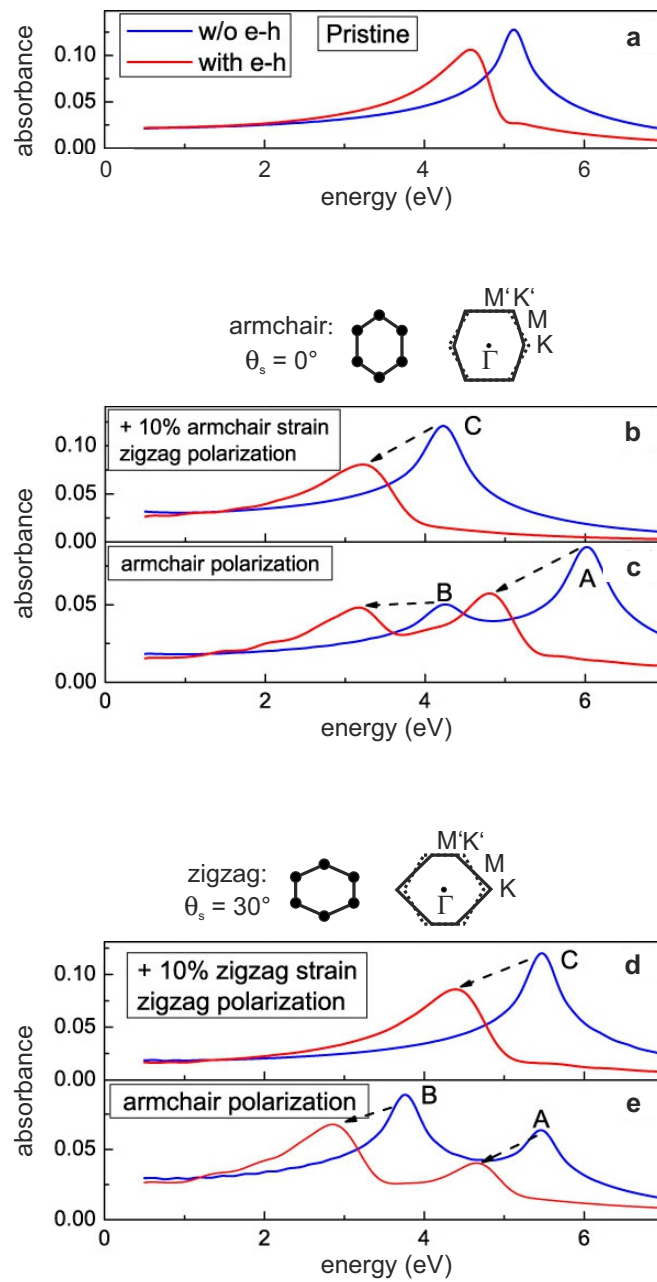


Figure 4.14: **a)** Optical absorption spectra of pristine graphene compared to graphene under armchair (**b,c**) and zigzag (**d,e**) strain for light polarized along the zigzag and armchair directions. The curves calculated including excitonic effects (red) are always redshifted with respect to those not taking many-body effects into account (blue). Adapted from [113].

due to electron-hole interactions.

Similar studies have been performed by other groups [128, 115] however without taking many-body effects into account. Their results confirm the calculations made by Liang [113] as they yield a good agreement regarding both the peak positions and the polarization dependence in the optical spectra without electron-hole interactions. Therefore, we trust also the calculations including excitonic effects presented above and set out to observe the predicted changes in our experiments on strained graphene.

4.6.2 Experimental results

Before discussing our results, we would like to turn the attention towards the given experimental conditions. Due to the fabrication of graphene with an exfoliation technique, the orientation of the flakes on the substrate is random. It can be determined from Raman spectroscopy, but cannot be controlled as the substrate has a preferred mounting direction. Furthermore, the white light from our source is unpolarized. A polarizer would allow to chose a certain excitation polarization, however, this results in a very low excitation power and long integration times. We therefore decided to neglect the polarization dependence of the spectra in a first step and measure with unpolarized light. This has the advantage that unpolarized light represents a superposition of zigzag and armchair polarization. We hence expect to see a change in the spectra independent of the actual crystal orientation because then in all cases a splitting of the absorption peak is predicted, as we have seen in figure 4.14b-e. Once a distinct change in the optical spectrum is observed, the experimental setup can be improved further so that polarization dependent measurements become possible.

i) PDMS:

Figure 4.15 summarizes our investigation of strain on the optical spectrum of graphene on PDMS. While the sample is continuously stretched, the Raman modes shown in figure 4.15c-d indicate a backshifting close to the original position for the last stretching step. We assume that the contact to the substrate is lost when a certain amount of strain is reached so that the flake relaxes. The strain values corresponding to the individual spectra can be estimated from equation 4.16 for the G^{\pm} mode (with $\nu = 0.5$ and the Grüneisen parameters as given above) and from direct comparison with the reference shift of $-64 \text{ cm}^{-1}/\%$ [116] for the 2D mode. Although this method is only an approximation, the values obtained for the different modes are in a good agreement and are indicated in the reflectivity spectra in figure 4.15a.

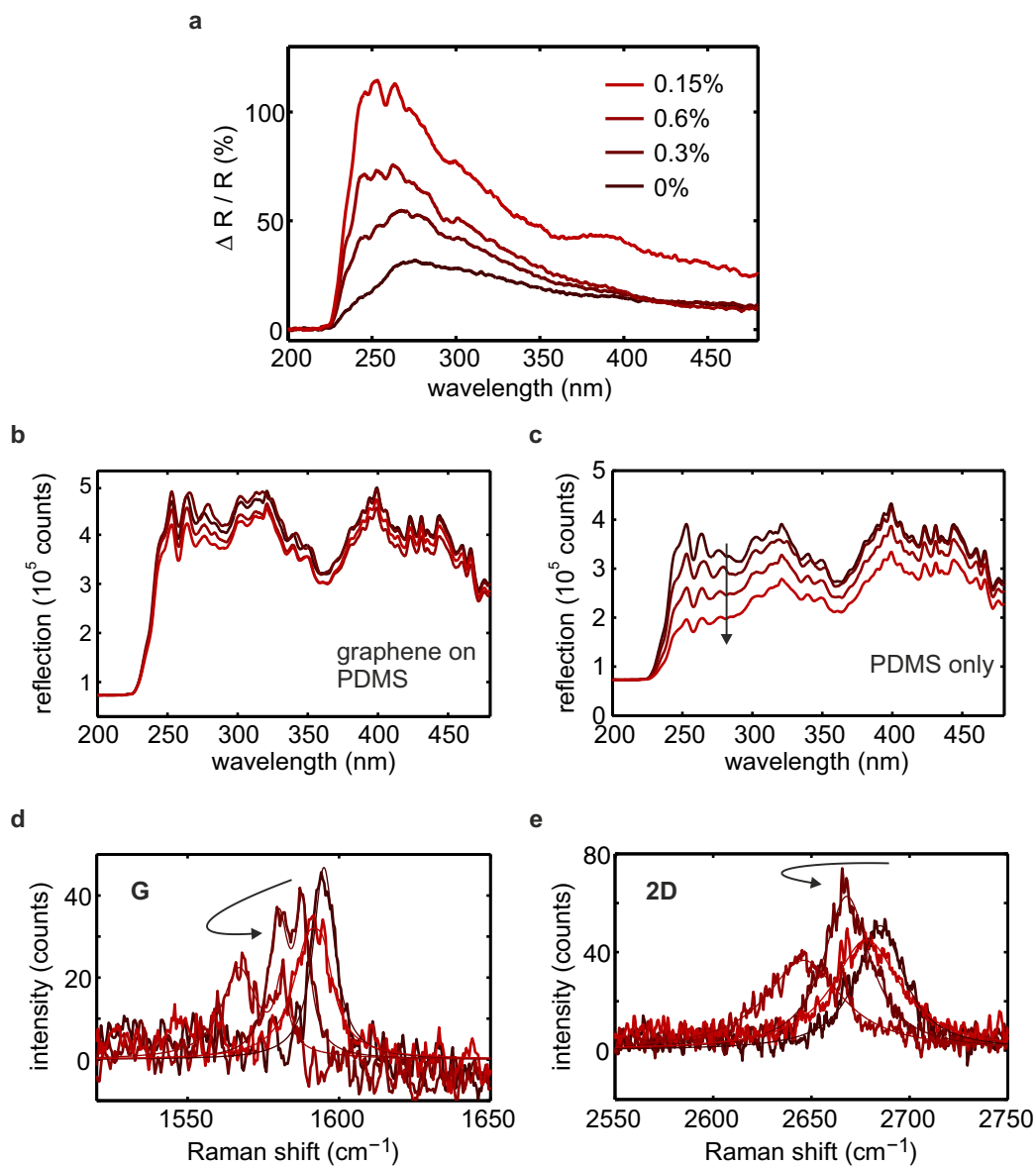


Figure 4.15: **a)** Reflectivity spectrum of graphene on PDMS for different amounts of strain as determined from the Raman spectra. **b)** While the reflection of graphene on PDMS is almost stable, **c)** the reflection of the bare substrate is constantly decreasing with increasing stretching as indicated by the black arrow. **d, e)** Corresponding behavior of the Raman modes G and 2D.

We immediately see that a drastic change is observed in the simultaneously measured reflectivity spectra in figure 4.15a, where the maximum of the peak in the ultraviolet increases from about 30% to more than 100%. Moreover, a signal seems to be modulated onto the original Fano lineshape which could indicate a peak splitting in the UV. Naturally, the induced changes in the spectrum should scale linearly with strain. We therefore expect the spectrum to come back close to the Fano lineshape in the last measurement where the strain decreases from $\epsilon = 0.6\%$ to $\epsilon = 0.15\%$ according to the Raman spectra. However, the reflectivity continuously increases with increasing stretching although the flake relaxes. We therefore suspect that it is the substrate rather than the graphene flake that gives rise to the observed behavior. To verify this assumption, let us consider the reflection spectra of graphene and graphene on the PDMS substrate shown in figure 4.15b and c. They are not normalized, so that the spectral shape is largely determined by the light source. Indeed, our suspicion is confirmed: while only minor changes are observed in the reflection of graphene on PDMS (figure 4.15b), there is a dramatic decrease in the reflection of the PDMS reference (figure 4.15c). It seems that the structure of the PDMS substrate used in our investigation is severely altered by strain. The behavior is less pronounced when a graphene cover layer is present, which seems to partially prevent the structure modification. Moreover, the reflectivity decrease and the exact spectral shape varies significantly over the sample. These facts hint at surface damages such as crack formation or other roughening effects. Consequently and regardless of the reason for the reflection decrease, the normalization of the reflectivity signal fails as PDMS exhibits spatial inhomogeneity and different behavior with and without graphene. That way, the evaluation of the spectra is ruled out. In addition to the reflectivity increase, the discrepancy also explains the modulation of the reflectivity signal in the vicinity of the maximum. It does not originate from the graphene flake but clearly corresponds to the features of the lamp spectrum in this spectral regime. Using the reflection spectrum of unstrained PDMS as reference for all measurements is not a valid option as, in this case, one cannot separate anymore between contributions from the graphene flake and contributions from the substrate.

In summary, we therefore state that PDMS does not allow the evaluation of strain-induced changes in the reflectivity spectrum of graphene. Any effects arising from the graphene flake are obscured by strain-induced and spatially varying modifications of the substrate.

ii) PMMA:

As we have seen in section 4.5, up to 0.6% strain can be applied reliably to a graphene sheet on PMMA. We monitor the Raman modes for every measured

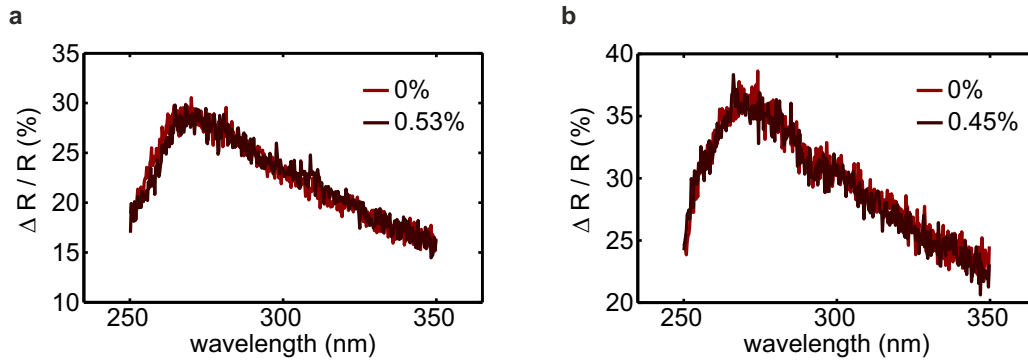


Figure 4.16: Comparison of the reflectivity spectra of graphene on PMMA with and without strain. Shown is only the UV regime where the strain-induced changes are expected. a) and b) represent different measurement series. The deviation arises from spatial inhomogeneities of the substrate. The strain value is determined from the corresponding Raman spectra and is the maximum value achieved in the respective measurement series.

reflectivity spectrum to estimate the amount of strain applied to the graphene flake. The Raman spectra are not shown in the following as they do not yield any further insight.

Figure 4.16 shows the reflectivity spectra without and with maximum achievable strain for two independent measurement series. For each series, the position of the light spot on the flake and on the substrate is fixed. In contrast, different positions on the flake have been measured in the different series. Obviously, the spectra within one series are comparable whereas slight deviations regarding both lineshape and maximum reflectivity arise between the series. We attribute this to spatial inhomogeneities of the substrate, leading to small variations in the optical constants and hence a few percent deviation in the response of the system. Nonetheless, the two examples in figure 4.16 clearly show that we do not observe a distinct change in the reflectivity spectrum of graphene. In addition to the spectra shown here, we have measured several strain cycles between 0 and 0.6% strain with step sizes of 0.025 – 0.05%. None of the series shows the development of a strain-induced feature like for example an additional peak or a peak broadening. Any deviations from the Fano lineshape can either not be reproduced when the measurement is repeated or turn out to be not systematic. We hence conclude that we do not see an effect of strain on the reflectivity spectrum of graphene on PMMA for strain values up to 0.6%.

	ΔE (eV)	$\Delta\lambda$ (nm)
10%	1.65*	$\sim 130^*$
2%	0.33	~ 20
0.6%	0.10	~ 5

Table 4.1: Estimation of the peak splitting for different amounts of strain. Data marked with an asteriks (*) is extracted from [113], the other values are extrapolated from these values. Splitting in wavelength regime is calculated relative to the peak position without strain at $E_0 = 4.8$ eV.

4.6.3 Discussion

Summarizing the experimental results, we have seen that our measurement method works – i.e. we apply strain to a graphene sheet on PMMA and are able to simultaneously measure Raman and reflectivity spectra – but we do not observe a strain-induced change in the Fano resonance. Is this in contradiction to the results from theory which predict a distinct effect? Here, we must be aware of the fact that the calculations by Liang [113] are carried out for 10% strain, whereas we reach below 1% strain with our experimental method. Inevitably, the expected changes in the optical spectrum will be considerably weaker. Assuming that the peak splitting with strain is linear in energy, the splitting at other strain values can be estimated from a simple extrapolation.

Table 4.1 shows the splitting of the peaks at 10% strain extracted directly from the calculation [113] (see figure 4.14) and the extrapolated splitting at 2% and 0.6%. Considering the strain values reached in our experiments, the expected splitting is only on the order of 5 nm. This is a very small value compared to the total width of the peak of 80 – 100 nm. As a consequence, we cannot expect to see a splitting of the UV peak in the experiment. The predicted effect might however manifest in a broadening of the peak. In our case, also this change will be subtle so that a careful analysis of the data is necessary in order to separate systematic changes from non-systematic deviations in the measurement. Note that this is most probably still the case for 20 nm splitting at 2% strain, which corresponds to an amount of strain that can be reliably achieved with the bending method (reported for example by [123]).

To get the clearest picture possible, we hence evaluate all reflectivity measurements performed with the PMMA sample as this allows a statistical analysis of potential changes in the spectra. Here, the Fano model presented in section 3.4 constitutes a simple yet powerful method to capture the overall shape of a spectrum. As shown in section 4.4, the measured reflectivity signal is in good

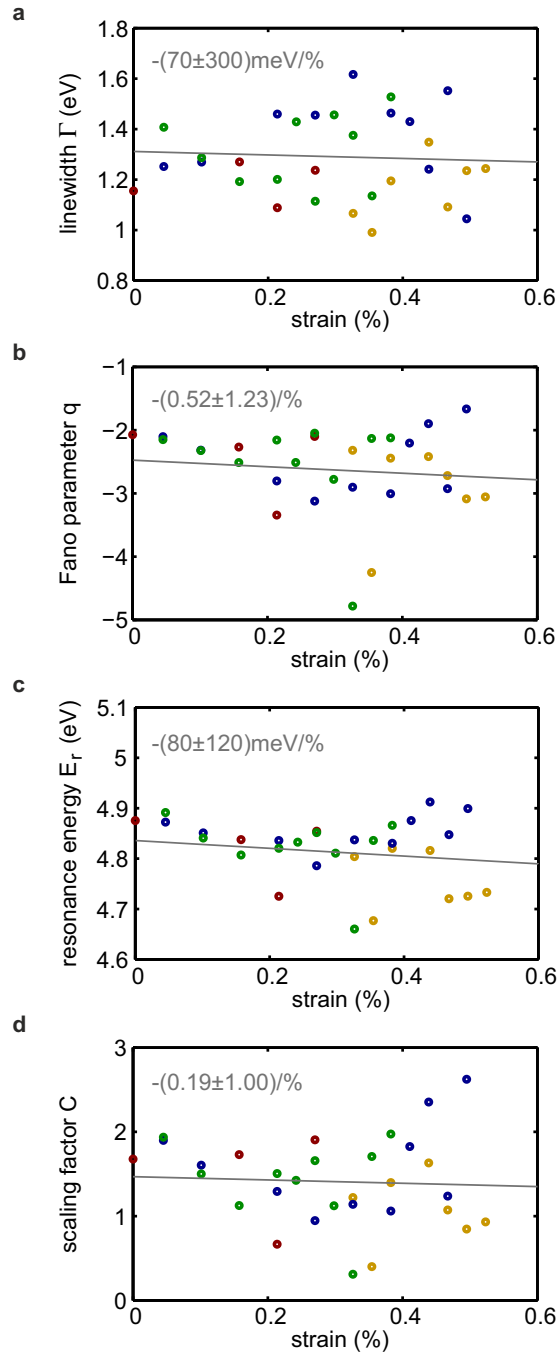


Figure 4.17: Overview of the strain dependence of the Fano parameters characterizing the reflectivity spectra, extracted from a Fano fit: **a)** linewidth Γ , **b)** Fano parameter q , **c)** resonance energy E_r , and **d)** scaling factor C . Different colours represent different measurement series. Gray lines are linear fits to the data with the given slopes.

agreement with the spectrum calculated with a transfer matrix model based on the optical constants of graphene extracted from a Fano fit to the absorption spectrum of a free-standing sample. Running this argument in reverse, we conclude that Fano fits to the strain-dependent spectra should reveal potential changes in the spectrum. We are very well aware of the fact that this method is not accurate: in fact, two independent Fano resonances should emerge with strain, corresponding to the non-degenerate saddle point excitons. In this case, however, the large number of fitting parameters leads to inconclusive results. We hence restrict to a single Fano lineshape, carefully checking the goodness of the fit and keeping in mind that potential trends in the fitting parameters have no physical meaning except for indicating strain-induced deviations.

Figure 4.17 shows scatter plots of the four Fano fitting parameters as a function of applied strain. Deviations from values of the Fano parameters determined for free-standing graphene (see Table 3.1) are attributed to the interaction with the substrate. Evidently, the parameters show a significant spread, which however agrees well with the variation observation for different graphene flakes without strain, which has been determined by Patrick Herlinger in his diploma thesis [117]. From his results, we originally concluded that the parameter spread is due to sample-to-sample inhomogeneities. In contrast, the present results suggest that the spread mainly arises from the measurement accuracy of our experimental setup.

However, the substantial number of data points in our experiment should at least partially compensate for this uncertainty, potentially allowing trends to be noticeable in the distribution. The linear fits to the data in figure 4.17 show that minor trends are observed for the different Fano parameters. We are mainly interested in the trend in the linewidth Γ . With increasing strain, we would expect a broadening due to the onset of a peak splitting and hence an increase in the linewidth. As shown in figure 4.17a, instead a narrowing with -70 meV/% is observed. However, the uncertainty of the extracted slope is many times higher than the actual value, undermining the validity of the fit. The same behavior is observed for the other Fano parameters. In consequence, neither the data nor the fit allows conclusion to be drawn about the influence of strain on the reflectivity spectrum. Note that this is also the case when the measurement series are analyzed individually. The limited measurement accuracy results in a substantial spread of the data and a considerably larger number of data points would be required to compensate for this.

In summary, we have seen that also the Fano fit does not reveal strain-induced changes in the reflectivity spectrum of graphene for strain values up to 0.6%.

4.7 CONCLUSIONS AND OUTLOOK

In this chapter, we have presented a detailed investigation of the effects of strain on the optical properties of graphene. Using a bending method and flexible substrates, strain values of up to a few percent lie within reach. Starting from a white light reflection setup, a Raman path was included in the experiment, allowing an in-situ characterization of the samples. We showed that the strain sensitivity of graphene's Raman modes in combination with well-established reference measurements establishes a reliable strain gauge. Moreover, we successfully demonstrated that the crystal orientation can be determined from polarization-dependent Raman measurements. Most important for our investigation is the fact that substrates and sample geometries must meet a set of requirements. These are imposed by our experimental conditions and include the adhesion of the flake to the substrate, the accessibility of the Raman spectrum, and good contrast in the optical spectrum. Step by step, we therefore tested the suitability of different substrate materials. Regarding our application, PMMA proved to be the best choice. Several strain cycles were measured with this sample, reproducibly providing strain values up to 0.6%. While the Raman spectra unambiguously show that strain is applied, we observed no effect in the reflectivity signal of graphene on PMMA. In contrast to theoretical calculations which predict a distinct splitting of the UV peak for 10% strain, more subtle changes are expected for small amounts of strain. However, even a careful analysis of the measured spectra with a Fano fitting method in combination with statistical analysis did not reveal any deviations arising from the applied strain.

We see mainly two possibilities for observing the predicted effect in spite of the given experimental results. First, it is clearly desirable to improve the measurement accuracy. Here, higher quality substrates and an optimization of the fabrication process could reduce or even eliminate spatial inhomogeneities. In addition, modulation techniques can help to suppress noise and background effects. With the present sample geometry, the maximum achievable strain is evidently too small to cause distinct effects. As a consequence, one might have to consider other approaches. However, many of the suggested and investigated straining methods lead to small-area and strongly nonuniform strain [44, 129, 130] and hence are not compatible with optical measurements. In our opinion, most promising alternatives to the bending technique are the clamping of graphene to piezoelectric substrates [131] and thin-film shrinkage technologies [132]. Both methods can provide tunable strain up to about 10% over large areas. Such more advanced samples will inevitably lead to more complex optical spectra. As in our investigation, it must be assured that the

analysis of the changes caused by a strain-induced modification of graphene's optical properties is still feasible.

Overall, our investigations prove once more the astonishing robustness of the optical spectrum of graphene as realistic amounts of strain have no detectable effect on the excitonic Fano resonance. Hence, we conclude that graphene's band structure is not only very stable against layer interactions and doping, but also against severe perturbations such as strain. The finding that strain hardly influences the optical properties of graphene is in fact beneficial regarding potential applications in optoelectronics where, on the contrary, strain-induced changes in the appearance or even the functionality of a device must be ruled out.

Part II

**LOCAL NONLINEAR SPECTROSCOPY OF
NANOSTRUCTURES**

Nano-optics or nanophotonics is an area of research covering the interaction of nanoscale systems with light, mostly in the visible wavelength regime [133, 1]. Many investigations in nano-optics involve metal nanoparticles which constitute the fundamental building blocks of plasmonics and metamaterials [22, 3]. Plasmonic effects are found for example in stained glasses and hence have in fact been observed for centuries. However, sophisticated techniques are required for the controlled fabrication of nanostructures, so that plasmonics is still a quite new field of research. Whereas the linear optical properties of nanoparticles and their assemblies are widely studied [13, 3], there are still many open questions regarding the nonlinear response of plasmonic structures. In our experiments, we study the nonlinear emission properties of individual gold nanostructures, shedding light onto different aspects of the still growing field of nonlinear plasmonics.

In this chapter, we provide an overview of the fundamentals of nonlinear nano-optics. First, a general introduction to the interaction of light with matter is given in section 5.1. Here, Maxwell's equations form the basis for a formal description. Drude-Lorentz theory is presented to model the linear material response. Our experiments focus on nonlinear material properties. An overview of important nonlinear optical processes and relevant properties of the signals is given in section 5.2. As plasmonic nanostructures are considered in our studies, we finally touch on the basics of plasmons in metal nanoparticles as well as the field of nonlinear plasmonics (see section 5.3).

5.1 LIGHT-MATTER INTERACTION: ELECTROMAGNETIC THEORY

5.1.1 Maxwell's equations

Maxwell's equations represent the basic equations of electromagnetic theory and describe the interaction of light with matter. In this section, we follow the description by Jackson and Maier [134, 3, 135]. The macroscopic Maxwell's equations read

$$\vec{\nabla} \cdot \vec{D} = \rho_{\text{ext}} \quad (5.1a)$$

$$\vec{\nabla} \times \vec{E} = -\frac{\partial \vec{B}}{\partial t} \quad (5.1b)$$

$$\vec{\nabla} \cdot \vec{B} = 0 \quad (5.1c)$$

$$\vec{\nabla} \times \vec{H} = \vec{j}_{\text{ext}} + \frac{\partial \vec{D}}{\partial t}. \quad (5.1d)$$

This set of equations is completed by the two constitutive relations

$$\vec{D} = \epsilon_0 \vec{E} + \vec{P} \quad (5.2a)$$

$$\vec{H} = \frac{1}{\mu_0} \vec{B} - \vec{M}, \quad (5.2b)$$

with the electric and magnetic field \vec{E} and \vec{H} , the dielectric displacement \vec{D} , the magnetic induction \vec{B} , the external charge density ρ_{ext} , the external current density \vec{j}_{ext} , the polarization \vec{P} , the magnetization \vec{M} , the vacuum (electric) permittivity ϵ_0 , and the vacuum (magnetic) permeability μ_0 . These equations hence link the four macroscopic fields to the external charge and current densities as well as the polarization and magnetization.

Polarization and magnetization represent the response of the medium to the electric and magnetic field of the incident wave. In this work, we restrict to isotropic and nonmagnetic media so that the magnetic response can be neglected. The polarization results from the alignment of microscopic dipoles with the electric field, yielding a linear relationship:

$$\vec{P} = \epsilon_0 \chi(\vec{E}) \vec{E} \quad (5.3)$$

where χ is the dielectric susceptibility. For low field intensities, the response of a medium is linear in the fields. In this case, the constitutive relations simplify to

$$\vec{D} = \epsilon_0 \epsilon \vec{E} \quad (5.4a)$$

$$\vec{H} = \frac{1}{\mu_0 \mu} \vec{B} \quad (5.4b)$$

with the relative permittivity or dielectric constant ϵ and the relative permeability μ . Furthermore, Ohm's law establishes a linear relationship between the current and the electric field via the conductivity σ :

$$\vec{j} = \sigma \vec{E}. \quad (5.5)$$

In contrast to the external current density \vec{j}_{ext} , \vec{j} is the current density in the medium. It is linked to the internal charge density ρ by $\nabla \cdot \vec{j} = -\partial\rho/\partial t$ which represents charge conservation. This also requires that the internal current density is related to the polarization by

$$\vec{j} = \frac{\partial \vec{P}}{\partial t}. \quad (5.6)$$

Comparing the above equations yields $\epsilon = 1 + \chi$. In general, the material constants ϵ and μ are second rank tensors and simplify to scalars only in the isotropic case.

From permittivity and permeability, the complex refractive index \tilde{n} can be derived as

$$\tilde{n} = n + i\kappa = \sqrt{\epsilon\mu}, \quad (5.7)$$

which for nonmagnetic media with $\mu = 1$ simplifies to $\tilde{n} = \sqrt{\epsilon}$.

Taking into account equations 5.2a and 5.6 and the fact that $\partial/\partial t \rightarrow -i\omega$ in frequency domain, we acquire a fundamental relationship between conductivity and dielectric function:

$$\epsilon(\vec{k}, \omega) = 1 + i \frac{\sigma(\vec{k}, \omega)}{\epsilon_0 \omega} \quad (5.8)$$

which has already been introduced in section 2.2. At optical frequencies, the dependency on the wavevector \vec{k} can be neglected as the wavelength in the material is significantly longer than the mean free path of the electrons [3]. Investigating the optical properties of a material, it is sufficient to determine either of the complex response functions ϵ , \tilde{n} , σ , or χ as they are all equivalent due to the above relations.

5.1.2 Drude-Lorentz theory of the linear material response

This section treats the Drude-Lorentz theory as a classical microscopic model for the frequency dependent complex response functions [76]. While the Lorentz model describes the response of the bound electrons, the Drude model treats

the free charge carriers.

In the Lorentz model, the response of electric charges in matter can be described by harmonic oscillators. For electrons driven by an applied electromagnetic field, the equation of motion is given by

$$\ddot{\vec{x}} + \gamma\dot{\vec{x}} + \omega_0^2\vec{x} = -\frac{e}{m}\vec{E}, \quad (5.9)$$

with the displacement \vec{x} , the electron mass m and charge e , the applied electric field \vec{E} , and the decay rate γ and eigenfrequency ω_0 of the harmonic oscillator. The solution to equation 5.9 is a superposition of a transient part, which is damped and dies away, and an oscillatory part with the frequency ω of the driving field. We are interested in the long-lasting oscillatory part

$$\vec{x} = \frac{(e/m)}{\omega^2 - \omega_0^2 + i\gamma\omega} \vec{E}. \quad (5.10)$$

For an ensemble of many oscillators n per unit volume, the dipole moments of the single oscillators $\vec{p} = -e\vec{x}$ sum up to the polarization (per unit volume)

$$\vec{P} = -ne\vec{x} = -\frac{n(e^2/m)}{\omega^2 - \omega_0^2 + i\gamma\omega} \vec{E}. \quad (5.11)$$

Comparing this result with $\vec{P} = \epsilon_0\chi\vec{E}$, we obtain the dielectric function for the system of harmonic oscillators

$$\epsilon = 1 + \chi = 1 - \frac{ne^2}{m\epsilon_0} \frac{1}{\omega^2 - \omega_0^2 + i\gamma\omega} \quad (5.12)$$

with the real and imaginary parts

$$\epsilon_1 = 1 - \frac{ne^2}{m\epsilon_0} \frac{(\omega^2 - \omega_0^2)}{(\omega^2 - \omega_0^2)^2 + \gamma^2\omega^2} \quad (5.13a)$$

$$\epsilon_2 = \frac{ne^2}{m\epsilon_0} \frac{\gamma\omega}{(\omega^2 - \omega_0^2)^2 + \gamma^2\omega^2}. \quad (5.13b)$$

In contrast to semiconductors or dielectrics, the conduction band of a metal is partially filled, allowing a quasi free movement of the electrons. Therefore, the conduction electrons in a metal are described as free electrons in the Drude model. They follow the same equation of motion as in the Lorentz oscillator model, but with vanishing restoring force so that $\omega_0 = 0$ and

$$\ddot{\vec{x}} + \gamma_D\dot{\vec{x}} = -\frac{e}{m}\vec{E}. \quad (5.14)$$

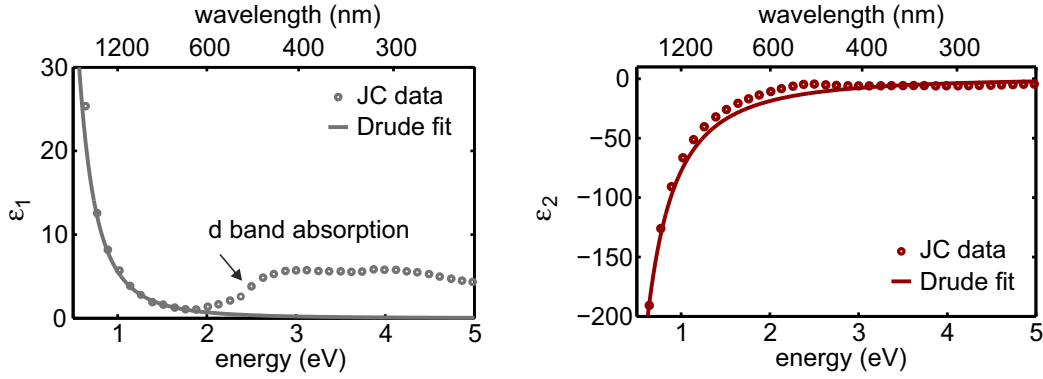


Figure 5.1: Comparison between the dielectric function measured by Johnson and Christy [136] (circles) and the Drude model (solid lines) with $\omega_p = 8.89$ eV and $\gamma_D = 0.07088$ eV [137].

γ_D is the phenomenological Drude damping parameter which accounts for deviations from the free electron approximation, for example due to scattering. The dielectric function can be derived as above to

$$\varepsilon = 1 + \chi = 1 - \omega_p^2 \frac{1}{\omega(\omega + i\gamma_D)} \quad (5.15)$$

with real and imaginary parts

$$\varepsilon_1 = 1 - \frac{\omega_p^2}{\omega^2 + \gamma_D^2} \quad (5.16a)$$

$$\varepsilon_2 = \frac{\gamma_D \omega_p^2}{\omega(\omega^2 + \gamma_D^2)}. \quad (5.16b)$$

Here, we have introduced the plasma frequency

$$\omega_p = \sqrt{\frac{ne^2}{m\varepsilon_0}}. \quad (5.17)$$

It can be interpreted as the frequency of the collective oscillation of the free electrons in the metal, which corresponds to a quasiparticle excitation called plasmon. n is the density of the free electrons and m the effective mass of an electron. In this simple picture, the optical properties of a metal are solely determined by the plasma frequency and the damping constant. In spite of its simplicity, the Drude model is a good way to estimate the optical constants of metals. As shown in figure 5.1, the measured data for gold agrees well with the Drude model, especially in the infrared and visible wavelength regime. The deviations in the imaginary part of the dielectric function above 2.2 eV (corresponding to wavelengths below 550 nm) are due to interband transitions – the so-called d band absorption – which also lead to increased damping [3].

5.2 NONLINEAR OPTICAL PROCESSES

Beyond the linear processes considered so far, we will now turn to nonlinear optical phenomena which are investigated in this part of the thesis. In nonlinear media, the material responds nonlinearly to the electric field of the excitation light. The field of nonlinear optics is tightly associated with the development of the laser as nonlinear effects require high intensity coherent excitation as is provided by lasers and especially by ultrashort laser pulses. In this overview of nonlinear optical phenomena, we closely follow the notation and argumentation of Boyd [25].

5.2.1 *Nonlinear polarization and nonlinear susceptibilities*

In the previous section, we have seen that the polarization of a material in the linear regime is related to the electric field by equation 5.3

$$\vec{P}(t) = \epsilon_0 \chi \vec{E}(t).$$

Microscopically, the nonlinearity of a material originates from the anharmonicity of the atomic potentials. While harmonic potentials are a good approximation for low excitation fields, anharmonic contributions are non-negligible when the field is on the order of the interatomic fields. In nonlinear optics, this is accounted for by generalizing the above relation to

$$\vec{P}(t) = \epsilon_0 \chi^{(1)} \vec{E}(t) + \epsilon_0 \chi^{(2)} \vec{E}(t)^2 + \epsilon_0 \chi^{(3)} \vec{E}(t)^3 + \dots \quad (5.18a)$$

$$\equiv \vec{P}^{(1)}(t) + \vec{P}^{(2)}(t) + \vec{P}^{(3)}(t) + \dots \quad (5.18b)$$

so that the polarization is a power series in the field strength. The first term describes linear effects while the higher order terms give the nonlinear polarization. $\vec{P}^{(n)}$ are referred to as n^{th} -order polarizations. $\chi^{(n)}$ are the n^{th} -order susceptibilities, which in general are tensors of rank $(n + 1)$.

The form of the linear as well as the nonlinear susceptibility tensors is determined by the symmetry of the material. According to Neumann's principle [138], the physical properties of a crystal must be invariant under the same symmetry operations as the crystal itself, determined by its point group. Hence, considering the symmetry properties of the corresponding crystal class, the number of nonzero and independent tensor elements can often be tremendously reduced. For example, the linear susceptibility condenses into a scalar value for isotropic and cubic materials. Out of the 32 crystal classes, 11 are centrosymmetric, i. e. possess an inversion center. When the sign of the excitation field changes

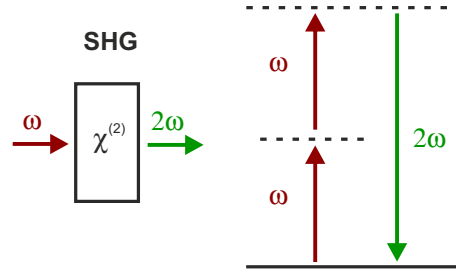


Figure 5.2: Geometry and energy level diagram of second-harmonic generation (SHG). Dashed lines represent virtual energy levels.

in a centrosymmetric material, the sign of the induced nonlinear polarization must also change due to the inversion symmetry:

$$-\vec{p}^{(2)}(t) = \epsilon_0 \chi^{(2)} [-\vec{E}(t)]^2 = \vec{p}^{(2)}(t). \quad (5.19)$$

This relation is only satisfied if the second-order polarization and hence $\chi^{(2)}$ vanishes. Consequently, centrosymmetric media do not exhibit second-order optical effects. In contrast, third-order nonlinear phenomena are allowed for both centro- and non-centrosymmetric materials.

5.2.2 Nonlinear optical processes

The most prominent effects investigated in nonlinear optics and also in this thesis are second- and third-order processes. To introduce the basic concept of these interactions, we first discuss second-order processes at the example of a lossless and dispersionless medium.

i) Second-harmonic generation

Consider a laser beam with electric field

$$\vec{E}(t) = E e^{-i\omega t} + \text{c.c.} \quad (5.20)$$

excites a material with second-order susceptibility $\chi^{(2)}$. c.c. denotes the complex conjugate and E is the field amplitude. From $\vec{p}^{(2)} = \epsilon_0 \chi^{(2)} \vec{E}^2$, we then obtain

$$\vec{p}^{(2)}(t) = \epsilon_0 \chi^{(2)} \left[2EE^* + (E^2 e^{-2i\omega t} + \text{c.c.}) \right]. \quad (5.21)$$

Consequently, there are two contributions, one at zero frequency and one at twice the excitation frequency. The first leads to a process called optical rectification, but does not generate radiation as the second time derivative vanishes. The

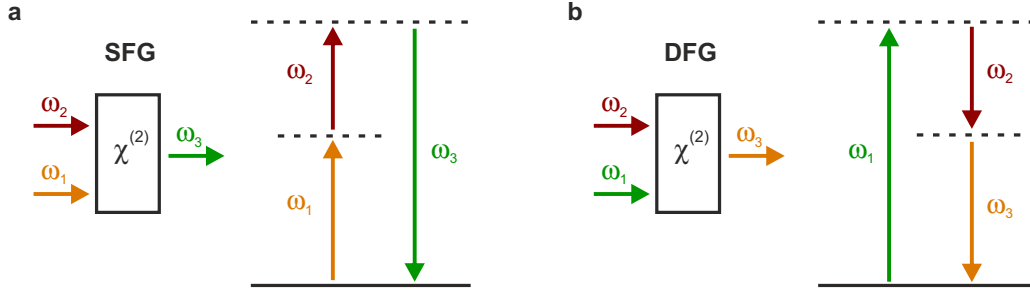


Figure 5.3: **a)** Sum-frequency generation (SFG) and **b)** difference-frequency generation (DFG). Shown are the geometry and the energy level diagram of the respective process. Dashed lines represent virtual energy levels.

latter contribution leads to second harmonic generation (SHG) which is schematically shown in figure 5.2. In this process, two photons of the excitation light generate one photon at the second-harmonic frequency 2ω . Usually not all power is converted so that the output light consists of ω and 2ω . SHG is a commonly used tool to frequency-double the output of infrared laser such as Nd:YAG and provide light in the visible spectral regime.

ii) Sum- and difference-frequency generation

Next, a field consisting of two different frequency components is applied:

$$\vec{E}(t) = E_1 e^{-i\omega_1 t} + E_2 e^{-i\omega_2 t} + \text{c.c.} \quad (5.22)$$

for which the second-order polarization then reads

$$\begin{aligned} \vec{P}^{(2)}(t) = \epsilon_0 \chi^{(2)} \Big[& E_1^2 e^{-2i\omega_1 t} + E_2^2 e^{-2i\omega_2 t} \\ & + 2E_1 E_2 e^{-i(\omega_1 + \omega_2)t} + 2E_1 E_2^* e^{-i(\omega_1 - \omega_2)t} \\ & + \text{c.c.} + 2(E_1 E_1^* + E_2 E_2^*) \Big]. \end{aligned} \quad (5.23)$$

Using the notation

$$\vec{P}(t) = \sum_n P(\omega_n) e^{-i\omega_n t}, \quad (5.24)$$

the complex amplitudes of the various terms of the nonlinear polarization are given by

$$P(2\omega_1) = \chi^{(2)} E_1^2 \quad (5.25a)$$

$$P(2\omega_2) = \chi^{(2)} E_2^2 \quad (5.25b)$$

$$P(\omega_1 + \omega_2) = 2\chi^{(2)} E_1 E_2 \quad (5.25c)$$

$$P(\omega_1 - \omega_2) = 2\chi^{(2)} E_1 E_2^* \quad (5.25d)$$

$$P(0) = 2\chi^{(2)} (E_1 E_1^* + E_2 E_2^*). \quad (5.25e)$$

Apart from the zero-frequency and the SHG contributions, two new contributions can be identified. The process in equation 5.25c converts two photons of frequency ω_1 and ω_2 into a photon of the sum of these frequencies $\omega_1 + \omega_2$ and is hence called sum-frequency generation (SFG), shown in figure 5.3. SHG is in fact a special case of SFG with $\omega_1 = \omega_2$. In analogy, equation 5.25d describes difference frequency generation (DFG), where the frequency of the generated photon is the difference of the incoming photon frequencies. However, energy conservation in this case requires that for any photon created at frequency $\omega_1 - \omega_2$, a photon at ω_1 is destroyed, but one at ω_2 is created by stimulated emission, as can also be seen in the energy level diagram in figure 5.3b. The lower-frequency excitation field is amplified in this process which is hence also called optical parametric amplification. Adding an optical resonator, this is used to build an optical parametric oscillator. SFG and DFG are essential in laser applications to extend the accessible frequency range.

iii) Third-harmonic processes

Regarding the third-order nonlinear polarization, obviously many contributing terms arise when the field consists of two or even three different frequency components, as shown in equation 5.23 for the second-order case. Consequently, a multitude of nonlinear frequency mixing processes arise. Involving four photons, these effects are referred to as four wave mixing (FWM). In case of a monochromatic fields of frequency ω as is considered in our experiment, only two terms remain. In the third-harmonic generation (THG) process, three photons of frequency ω are combined to generate a high-energy photon at 3ω (see figure 5.4b). This effect is in complete analogy to SHG. The other term leads to an intensity- and $\chi^{(3)}$ -dependent refractive index at the fundamental frequency ω , which can result in effects like self focusing or self phase modulation.

iv) Multi-photon photoluminescence

In addition to the nonlinear optical effects discussed so far, we also observe multi-photon excited photoluminescence in our experiments. The underlying nonlinear optical effect is multi-photon absorption which is followed by photoluminescence. As an example, a three-photon photoluminescence (3PPL) process is shown in figure 5.4c. The name is determined by the number of photons that are absorbed in the process. Similar to THG, three excitation photons are converted into a photon of higher energy, however, with a frequency ω_L that is smaller than three times the excitation frequency ω . This deviation is due to the fact that, after excitation, the system nonradiatively relaxes into a lower-energy state from which it then decays, emitting luminescence light at ω_L .

v) Parametric processes and coherence

Nonlinear optical effects are categorized into parametric and non-parametric processes. In a parametric process, the quantum mechanical state of the system is not changed by the interaction with the excitation field, so that the initial and final states are identical. Consequently, parametric processes are considered to be instantaneous and are in general coherent. Except for the ground state, the involved energy levels are virtual. The properties of the light generated in a parametric process are hence directly correlated with the properties of the excitation light such as phase and polarization. Higher harmonic generation (SHG, THG) and frequency-mixing processes (DFG, SFG, FWM) are examples of parametric processes. On the other hand, any quantum state of the system changes in a non-parametric process and population is transferred between two real levels. Such processes are often related to loss and, most importantly, are not coherent so that the generated light can have random phase and polarization. Absorption and inelastic scattering are typical examples of non-parametric processes. Multi-photon photoluminescence is hence the result of a non-parametric process and not coherent with the excitation light.

vi) Relative strength of the nonlinear optical processes

In general, the probability of a process decreases significantly with the number of photons involved. As mentioned above, higher-order nonlinear effects can still become comparable to linear ones when the excitation field intensity is on the order of the interatomic field strength, which is achievable with lasers. At a fixed excitation power, the strength of the nonlinear contributions usually

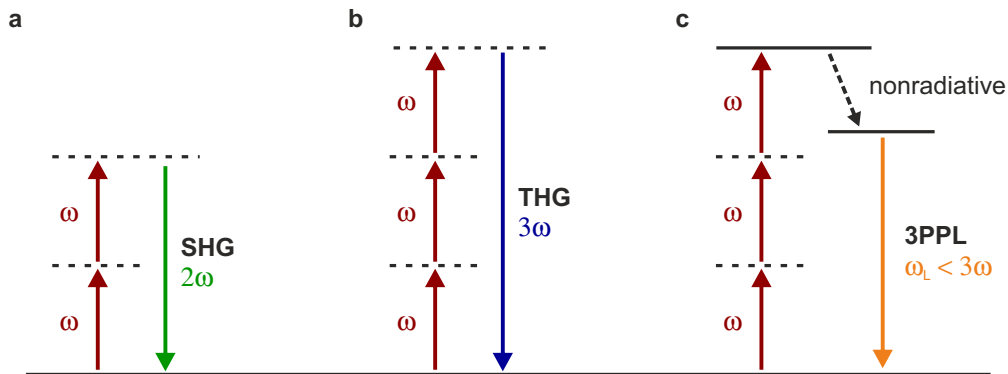


Figure 5.4: Overview of the nonlinear processes observed in our experiments. **a)** Second-harmonic generation (SHG), **b)** third-harmonic generation, and **c)** multi-photon photoluminescence, here involving four photons. Dashed lines represent virtual states, solid lines real states.

decreases with increasing order. Naturally, the strength of a certain effect is determined by the corresponding nonlinear susceptibility $\chi^{(n)}$. Although the symmetry considerations according to Neumann's principle are very powerful, they cannot predict the relative strength of different $\chi^{(n)}$ processes. Some semi-empirical models relate the nonlinear susceptibility of a material to its linear susceptibility. For example, Miller's rule predicts the second-order nonlinearity and can be generalized to third-order in some cases [139, 25]. Typically, only one of the nonlinear processes of a certain order (for second order see equations 5.25a-5.25d) is efficient in a bulk material. This is due to the fact that the phase-matching condition must be fulfilled, i. e. there must be a fixed phase relation between the different waves to ensure constructive interference and hence high conversion efficiency. In practice, nearly any process can be phase-matched by creating a structure of a certain periodicity in the crystal, a technique which is called quasi-phase-matching. For structures smaller than the wavelength, phase-matching conditions are not relevant [26] whereas other effects become important, which will be discussed in the next section. Finally, the efficiency of a particular parametric process can be enhanced considerably when one of the virtual states coincides or nearly coincides with a real state. In this case, the coupling of the system to the excitation field is particularly strong, resulting in a large nonlinear susceptibility. This includes also material resonances like plasmonic resonances. Here, a perturbation term can be added to the Lorentz model (see section 5.1), resulting in an anharmonic oscillator model which predicts the frequency dependence of the nonlinear signal from a plasmonic structure. The anharmonic oscillator model is a basic part of our simulations of nonlinear responses and fields which is discussed in section 6.4.

5.3 PLASMONICS

As mentioned in section 5.1, the plasma frequency ω_p in the Drude model for the free electrons in a metal can be recognized as the frequency of a collective oscillation of the electron sea, corresponding to a quasiparticle excitation. The quanta of this excitation are called volume plasmons. Being longitudinal by nature, volume plasmons cannot be excited with (transverse) electromagnetic fields. Also at the surface of the interface between a dielectric and a metal, collective oscillations of the electrons can arise. The resulting surface plasmons are excited by electromagnetic fields and propagate along the interface [3]. Correctly, they are referred to as surface plasmon polaritons (SPP) due to the coupling between the electromagnetic fields in the metal and the dielectric. Most often, the term "plasmon" is used for a third category of quasiparticles, named localized surface

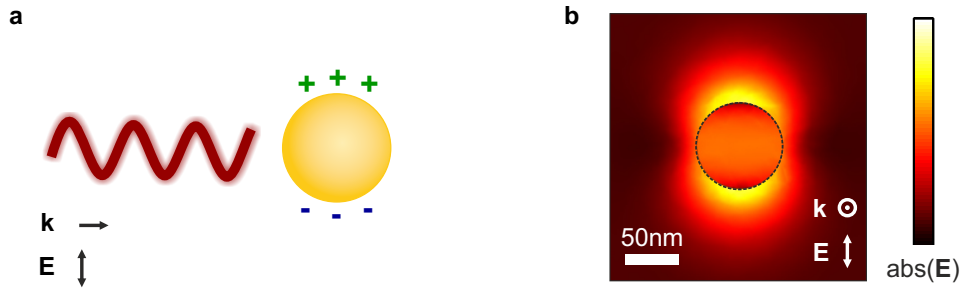


Figure 5.5: Excitation of a particle plasmon by an optical field with electric field vector \vec{E} and wavevector \vec{k} . **a)** Schematic illustration of the displacement of the electrons. The size of the nanoparticles is usually smaller than the excitation wavelength. **b)** Plasmonic hot-spots in the vicinity of the nanoparticle. Shown is the absolute value of the electric field calculated with a finite element method (at the plasmon resonance).

plasmon or particle plasmon, which we will restrict to in the following. Again, the correct name is particle plasmon polariton because of the coupling to the exciting electromagnetic field. We show below that this excitation is naturally associated with conducting nanoparticles. Accordingly, plasmonics usually refers to the optical properties of metal nanoparticles.

5.3.1 Plasmons in metal nanoparticles

When a nanoparticle is excited by an external light field as shown in figure 5.5a, the free electrons are displaced with respect to the positively charged ions of the lattice. For particle sizes smaller than the excitation wavelength, the confinement due to the particle boundaries leads to a quantization of the eigenenergies of the electron gas, in a first approximation corresponding to a harmonic potential. The quanta of the excitation are referred to as particle plasmon resonances. At a plasmon resonance, high field intensities can emerge in the vicinity of the particle, the so-called plasmonic hot-spots (see figure 5.5b). Relative to the electric field in free space, the near-fields can easily be enhanced by an order of magnitude [140, 3]. This effect is exploited using plasmonic particles as nanoantennas to enhance weak optical signals [141, 142].

As long as the particles are not too small (> 10 nm) so that quantum effects can be neglected [143], the interaction of nanoparticles with light is still governed by Maxwell's equations. Moreover, the particles are typically small compared to the wavelength of light $d \ll \lambda$. The phase of the electromagnetic field can then be assumed to be constant over the particle volume and retardation effects can

be neglected. In this quasi-static approximation, the particle interacts with an electrostatic field which simplifies the problem significantly.

To understand the origin of a plasmonic resonance, we first consider a spherical particle of radius a and dielectric constant ϵ in a medium with dielectric constant ϵ_m that is excited by a static electric field with amplitude E_0 . A full discussion of this problem is given for example by Maier [3]. Solving Maxwell's equations with the adequate boundary conditions, the potential outside of the particle evaluates to

$$\Phi_{\text{out}}(r, \theta) = -E_0 r \cos \theta + \frac{\epsilon - \epsilon_m}{\epsilon + 2\epsilon_m} E_0 a^3 \frac{\cos \theta}{r^2}. \quad (5.26)$$

This corresponds to a superposition of the applied field, described by the first term, and the field generated by the particle in the second term. Remarkably, the second field is equivalent to that of a dipole located at the particle center. The field hence induces a dipole moment

$$\vec{p} = 4\pi\epsilon_0\epsilon_m a^3 \frac{\epsilon - \epsilon_m}{\epsilon + 2\epsilon_m} \vec{E}_0, \quad (5.27)$$

in the sphere. Introducing a polarizability α defined by $\vec{p} = \epsilon_0\epsilon_m\alpha\vec{E}_0$ yields

$$\alpha = 4\pi a^3 \frac{\epsilon - \epsilon_m}{\epsilon + 2\epsilon_m}. \quad (5.28)$$

Evidently, the polarizability is maximized and a resonance occurs when $|\epsilon + 2\epsilon_m|$ is minimized. The resonance position depends strongly on the particle material as well as the refractive index of the surrounding medium. The electric field inside and outside the particle read as

$$\vec{E}_{\text{in}} = \frac{3\epsilon_m}{\epsilon + 2\epsilon_m} \vec{E}_0 \quad (5.29a)$$

$$\vec{E}_{\text{out}} = \vec{E}_0 + \frac{3\vec{n}(\vec{n} \cdot \vec{p}) - \vec{p}}{4\pi\epsilon_0\epsilon_m} \frac{1}{r^3} \quad (5.29b)$$

with the unit vector \vec{n} . The localized electric field around the nanoparticle hence shows a dipole-like distribution. As mentioned above, the fields inside and outside the particle are enhanced as the polarizability is minimized at the resonance. In optics, the efficiency with which an obstacle scatters or absorbs light is given by the cross sections C_{scat} and C_{abs} , respectively. These quantities describe how much energy is scattered/absorbed relative to the incident power. An enhancement of the polarizability of a small particle at a plasmon resonance leads also to increased scattering and absorption cross sections [144]:

$$C_{\text{scat}} = \frac{k^4}{6\pi} |\alpha|^2 = \frac{8\pi}{3} k^4 a^6 \left| \frac{3\epsilon_m}{\epsilon + 2\epsilon_m} \right|^2 \quad (5.30a)$$

$$C_{\text{abs}} = k\mathcal{J}[\alpha] = 4\pi k a^3 \mathcal{J} \left[\frac{3\epsilon_m}{\epsilon + 2\epsilon_m} \right]. \quad (5.30b)$$

\Im denotes the imaginary part of the function. Both interactions hence scale strongly with the particle radius. Unsurprisingly, the absorption scales with the particle volume a^3 .

We will now relax some of the approximations made above and discuss some more general cases.

When the particle is excited with an oscillating electromagnetic field $\vec{E}(t) = \vec{E}_0 e^{-i\omega t}$ instead of a static one, an oscillating dipole moment $\vec{p}(t) = \epsilon_0 \epsilon_m \alpha \vec{E}_0 e^{-i\omega t}$ is induced. This leads to scattering of the excitation wave and can be identified as radiation by a point dipole [3]. While the near field $kr \ll 1$ is the same as in the static case, spherical waves are now radiated into the far field $kr \gg 1$ [134].

For larger particles which are not small compared to the wavelength of light, the quasi-static approximation is not valid anymore and retardation effects come into play. However, the problem can still be solved analytically for spherical particles, as has been shown by Mie [145]. In this approach, the internal and scattered field are expanded into a set of normal modes. The solution to the scattering problem is then an infinite series of vector spherical harmonics. That way, in addition to the fundamental dipolar mode also higher order plasmon resonances emerge at higher energies. For silver spheres, the appearance of higher order plasmon resonances with increasing diameter is shown in figure 5.6. For gold spheres, this effect is less distinct due to the d-band absorption below 550 nm. Higher order modes can be modeled analytically also for nanorods, treating them as one dimensional cavities [146, 147]. In the rod, standing wave patterns are formed, resulting in fields and consequently a current density distributions

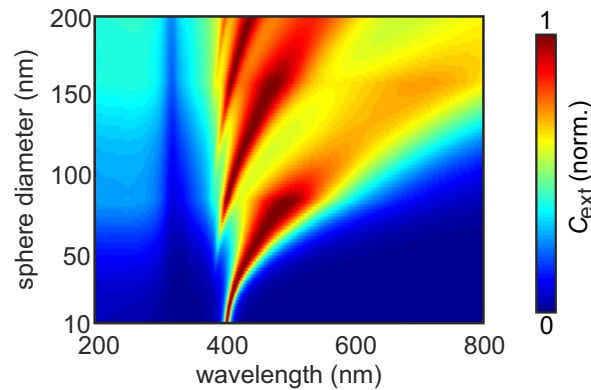


Figure 5.6: Mie theory: Normalized extinction cross section of silver spheres with diameters between 10 and 200 nm in a medium with refractive index $n = 1.5$. The dielectric constant of silver is chosen according to measured data [136]. With increasing diameter, higher order plasmon resonances appear.

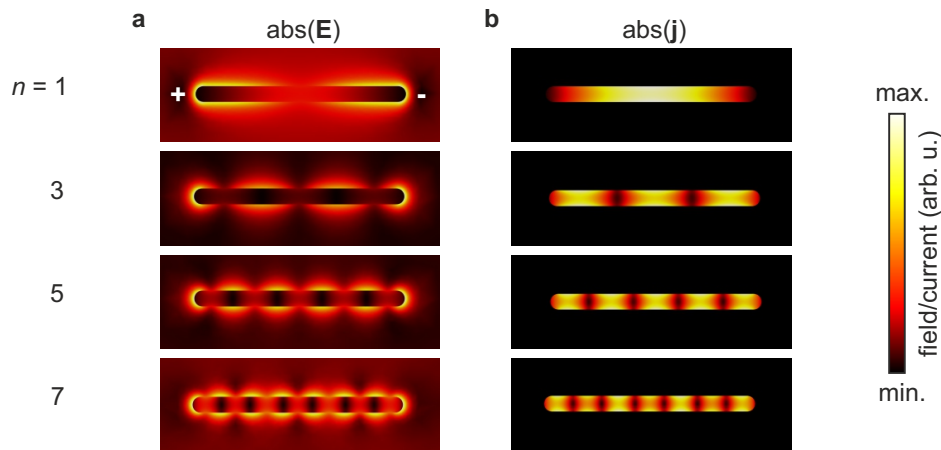


Figure 5.7: Higher order plasmon modes in an extended rod structure. Shown are the absolute values of the electric field (a) and the current (b) calculated with a finite element method.

in the rod as schematically illustrated in figure 5.7. The order n of the mode is given by the number of current density lobes. Due to symmetry of the rod and the excitation, only odd order modes are allowed. In contrast to the odd order modes, the even order modes have no net dipole moment and hence cannot be excited optically.

In conclusion, we have seen that a plasmon resonance can emerge when conducting nanoparticles are excited with light. The spectral position of the resonance depends on the particle material, its size, and the surrounding medium. For gold, the plasmon resonance is in the visible regime for particles of a few tens of nanometers in diameter. Unlike silver, it is also stable towards oxidation, and hence is the material of choice in plasmonics. When the particle geometry deviates from a sphere and the particle size is comparable to or larger than the wavelength, it is usually a demanding task to compute scattering and absorption cross sections, since there is no simple analytical solution. Therefore, these quantities are typically calculated using numerical methods, in our case a finite element method which is discussed in section 6.4.

5.3.2 Nonlinear plasmonics

The investigation of nonlinear optical effects in combination with plasmonics is interesting in many regards. A good overview of this topic is given by [26].

In addition to many other exceptional properties, metals exhibit strong optical nonlinearities with nonlinear susceptibilities comparable or even exceeding those of commonly used nonlinear crystals [148, 149]. On the nanoscale, metal structures thus become promising candidates for frequency conversion applications as they can couple very efficiently to light [148]. As mentioned in the last section, the efficiency of nonlinear signals can often be related to the linear response. Adding a perturbation term to the Lorentz oscillator model (see section 5.1) yields an anharmonic oscillator model, which is a simple but successful method to predict the spectral dependence [150] and efficiency [151] of nonlinear processes in plasmonic structures. As the (linear) plasmon resonance can be shaped via material, shape, size, etc. [11], this allows to optimize structures with respect to their nonlinear optical properties. In our numerical calculations, we also take advantage of the relation between linear and nonlinear response (see section 6.4).

Besides the nonlinear optical properties of the plasmonic structures themselves, nonlinear plasmonics also investigates the modification of the nonlinear response from a surrounding medium due to the interaction with plasmonic structures. Many studies have focused on the enhancement of nonlinear processes by plasmonic structures. Here, the plasmonic structure typically acts as a nanoantenna, boosting a nonlinear response via the enhanced local fields [152, 153].

METHODS

In this chapter, we give an overview of the techniques needed and used for the experimental and theoretical investigation of the nonlinear emission properties of nanostructures. The field of nano-optics emerged from advances in fabrication techniques including lithography and thin-film technology, which is still a very active area of research and development. In the following, we first give a short summary of the fabrication process of metal nanostructures with electron beam lithography in section 6.1. In order to measure the optical properties especially of individual nanoscopic systems, powerful microscopes and sensitive detection schemes are indispensable. In our measurements, we combine a nonlinear transmission setup with back focal plane imaging to fully capture the emission properties of the plasmonic structures. The experimental setup is described in section 6.2. In addition to the experimental methods, simulation techniques are essential to interpret and optimize the investigated structures. To simulate the spatial emission characteristics of the nanostructures, we developed a code based on the problem of a dipole at an interface which is presented in section 6.3. A finite element method is used to calculate the linear and nonlinear local fields of the nanostructures (see section 6.4).

6.1 NANOFABRICATION: ELECTRON BEAM LITHOGRAPHY

In the following, we give a short introduction to the standard nanofabrication process with electron beam lithography as illustrated in figure 6.1. This process is very versatile and allows the fabrication of nanostructures of nearly arbitrary shape and arrangement in two dimensions. The samples investigated in this thesis have been fabricated in the cleanroom of the Max Planck Institute for Solid State Research in Stuttgart.

All samples are fabricated on 170 μm thick glass cover slips, which is adapted to the correction of the immersion objective used in the transmission measurement. After cleaning the substrate, a double layer of resist (PMMA (poly methylmethacrylate), 250k/2.5% and 950k/1.5%, Allresist) is spin coated (5 s at 3000 rpm and 30 s at 8000 rpm). Each layer is baked for 5 min at 160°C on a

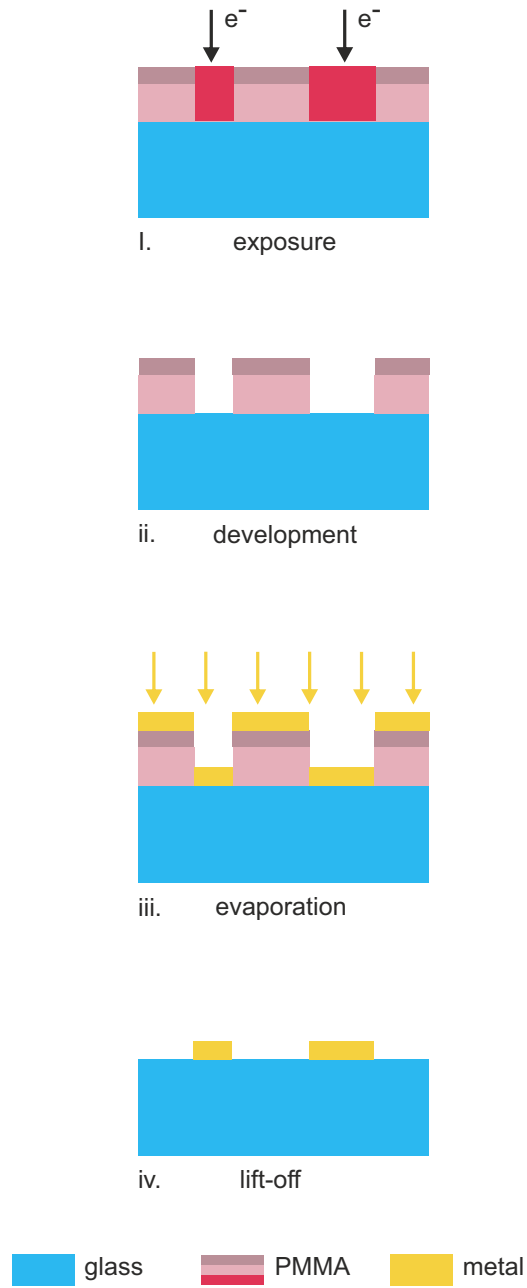


Figure 6.1: Main steps of the electron beam lithography process.

hotplate. While the ~ 50 nm thick, high chain-length top layer guarantees high resolution, the ~ 150 nm thick layer with lower chain-length facilitates the lift-off process. Finally, a water-soluble conductive polymer (espacer, Showa Denko) is spin coated (60 s at 4000 rpm, no baking) to avoid charging of the sample. Alternatively, a few nanometers of chromium can be evaporated to provide conductivity. The sample is then exposed with a beam of electrons (Raith eline, 20 kV acceleration voltage, 20 μm aperture yielding ~ 150 pA beam current). The exact exposure parameters depend on the desired structure size, density, and quality, see table 6.1 for typical values. After exposure, the conductive layer is washed off with distilled water (alternatively, the chromium layer is removed with a commercially available chromium etchant). The resist is developed for 90 s in a 1:3 mixture of MIBK (methylisobutylketone) and isopropanol and development is stopped in a pure isopropanol bath (30 s). The metal layers are evaporated thermally (Oerlikon–Leybold Univex). A 2 – 3 nm thick chromium (or titanium) layer provides adhesion of the gold film to the glass substrate. The height of the evaporated layer depends on the desired structure and is typically ~ 30 nm. In the lift-off step, the remaining resist film with the excess metal is removed from the sample (remover based on NEP (N-ethyl-2-pyrrolidone), Allresist, at 65°C for 2 h).

After fabrication, a bright- and dark-field capable microscope gives a first impression of the sample quality (see figure 6.2a,b). Here, we see if the lift-off was successful and the structures exist. However, only a scanning electron microscope (SEM) can resolve nanometer size substructures. It is hence an indispensable tool to check the sample quality and measure structure sizes (see figure 6.2c). Due to contamination of the sample under the SEM, all optical measurements must be finished before this final characterization.

write field size	100 x 100 μm^2
acceleration voltage	20 kV
aperture	20 μm
beam current	~ 150 pA
settling time	1 ms
area/curved elements dose	325 $\mu\text{C}/\text{cm}^2$
area/curved elements step size	4 nm
line dose	1300 pC/cm
line step size	2 nm

Table 6.1: Exposure parameters of a typical electron beam lithography process.

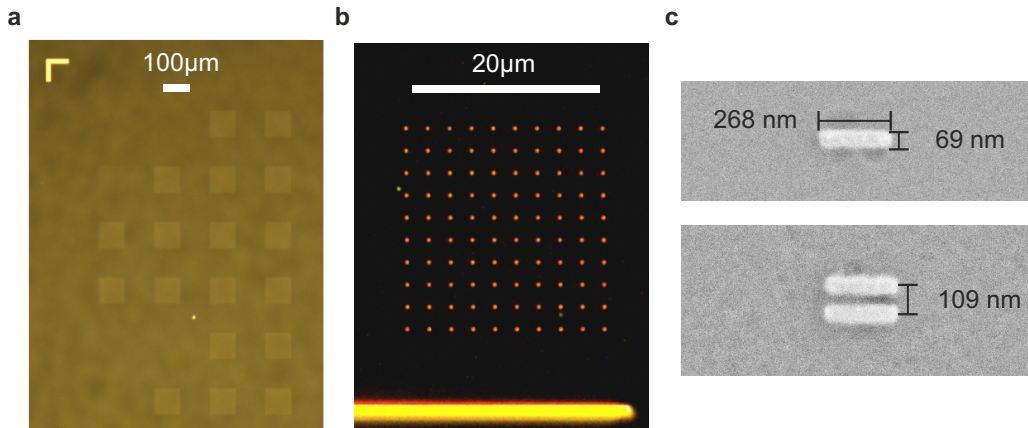


Figure 6.2: Characterization of the nanostructures. **a)** Bright-field microscope image of a sample consisting of different $100 \times 100 \mu\text{m}^2$ fields with dense nanostructures and a gold marker structure. Objective magnification is $5\times$. **b)** Dark-field microscope image resolving single nanostructures with $2.5 \mu\text{m}$ spacing. Objective magnification is $100\times$. **c)** SEM images of a gold nanorod and a nanorod pair. Magnification is $50,000\times$.

6.2 EXPERIMENTAL REALIZATION: NONLINEAR TRANSMISSION SETUP AND BACK FOCAL PLANE IMAGING

A schematic sketch of the nonlinear transmission setup is shown in figure 6.3. A frequency-doubled Nd:YVO₄ laser (Coherent Verdi G18, 532 nm, 18 W CW) pumps a high-power titanium-sapphire oscillator operated at 800 nm (Coherent MIRA, 76 MHz, ~ 150 fs, 4 W). Part of the pulsed output light is guided to an optical parametric oscillator (Coherent MIRA-OPO) which is used in the linear cavity configuration. It provides infrared pulses (76 MHz, ~ 180 fs) which are tunable in the wavelength regime 1050–1500 nm with few hundred mW output power. Using a half-wave plate, the linear polarization of the infrared light can be rotated. The excitation power is adjusted to the desired value with neutral density filters. A 1000 nm longpass filter transmits the infrared light only. In the microscope unit, an infrared lens (NA 0.6) focuses the light to a spot size of $\sim 1.5 \mu\text{m}$ on the sample. The sample is mounted on a 3D piezo stage and can hence be scanned in the laser focus. The transmitted light as well as the generated nonlinear signals are collected with a high NA oil immersion objective ($60\times$, NA 1.35). A Schott KG5 glass is used to remove the infrared excitation light. Instead of or in combination with the Schott glass, longpass and bandpass filters allow the investigation of signal contributions at specific wavelengths. The light is then guided to the monochromator (Princeton Instruments Isoplan SCT 320)

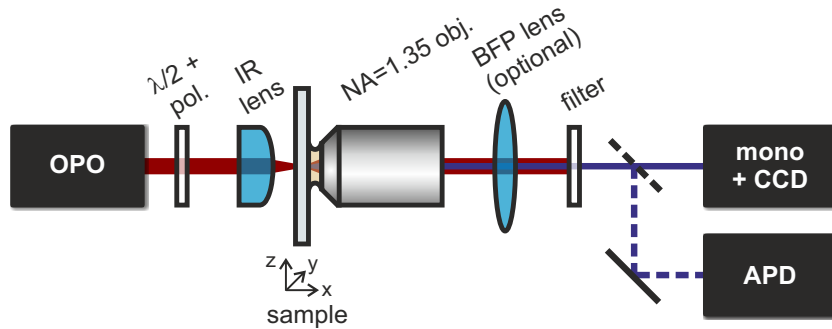


Figure 6.3: Sketch of the nonlinear transmission setup.

equipped with a CCD camera (Princeton Instruments Pixis 400), allowing both imaging of the sample with a mirror and spectral analysis of the signal with a grating. Alternatively, the structures can be mapped and localized on the sample with a single photon counting avalanche photo diode (APD). With an APD and a spectrometer, nanostructures can hence be localized on the sample and information about emission intensities as well as spectra can be obtained.

A slight modification of the experimental setup allows to obtain even more details about the light emission from the nanostructures by imaging the back focal plane of the microscope objective. To explain the underlying method, we consider a sample that emits plane waves in the focus of a lens – in our case the oil immersion objective – as schematically shown in figure 6.4a. Following the

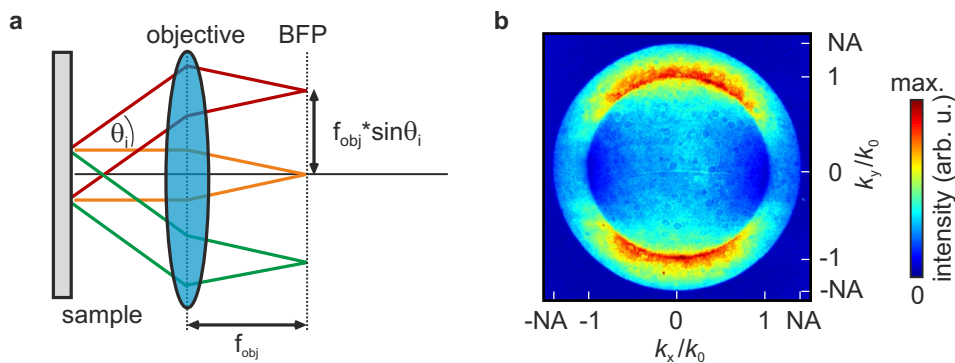


Figure 6.4: **a)** Principle of back focal plane (BFP) imaging. Rays leaving the light under the same angle are focused into one point in the BFP. **b)** Measured BFP image of a 270 nm long gold nanorod.

principles of ray optics, all light rays that leave the sample under a certain tilt angle θ_i will be focused into one single point at a distance $r_i = f_{\text{obj}} \sin \theta_i$ from the optical axis, here shown in 2D. In 3D, this point corresponds to a ring with radius r_i . For any angle θ_i , the so-called back focal point (or ring) is found in the same plane perpendicular to the optical axis. This plane is called back focal plane (BFP) and contains information about the spatial emission properties of the sample, i. e. how much light is emitted into which direction. In other words, the Fourier transform of the emitting object is found in the back focal plane, which is therefore sometimes also referred to as Fourier plane. Hence, by imaging the back focal plane of the microscope objective, the Fourier image of the sample in k space is acquired instead of the real space image. This can be achieved by placing an additional lens, the so-called Bertrand lens, in the optical path such that its focus coincides with the BFP. In our case, a lens with focal length 300 mm leads to a good image quality and size on the CCD camera.

Figure 6.4b shows an example of a measured BFP image. The expected ring structure is clearly visible. Obviously, the image shows an outer limit which corresponds to the maximum angle α collected by the lens/objective and is hence given by its numerical aperture (here $\text{NA} = n \sin \alpha = 1.35$ with the refractive index of the substrate $n = 1.5$). Moreover, most light is radiated under high angles. For this reason, it is most important to use a high-NA oil immersion objective. In the next section, we present a simple model to calculate the radiation patterns of a nanoparticle on a substrate. In the course of this discussion, also the intensity distribution in the pattern will be elucidated.

6.3 CALCULATION OF RADIATION PATTERNS: DIPOLES AT AN INTERFACE

In the experiment, we measure the light that is emitted from nanostructures excited at the plasmon resonance. As discussed in section 5.3, the radiated fields in the quasi-static approximation then correspond to those of a point dipole. In free space, the radiation pattern of a dipole is characterized simply by a $\sin^2 \theta$ distribution with the angle θ between dipole axis and observation direction [134]. However, the structures are fabricated on a substrate which scatters light. Dipole emission near a planar interface is a typical problem in nanooptics as it is relevant for many studies including for example single molecule and surface enhanced spectroscopy. A comprehensive analysis can therefore be found in many textbooks. We would like to restrict to a qualitative discussion of the key steps and refer to [148] for a detailed derivation.

Starting from a dipole with dipole moment \vec{p} in free space, the electric field is first decomposed into the s- and the p-polarized part for the components parallel and perpendicular to the interface, respectively. In general, the light emitted from the dipole is refracted and partially reflected at the interface. This is taken into account by applying the Fresnel coefficients for reflection r_s, r_p and transmission t_s, t_p to the s- and p-polarized components of the field. For a single interface as in our case, the field in the upper half-space is then the superposition of the primary dipole field and the reflected field. The field in lower half-space is given by the transmitted field. When the signals are observed in the far-field zone as in our experiments, the asymptotic form of the fields needs to be derived. Finally, in the coordinate system depicted in figure 6.5, the fields read as [148, 154]

$$\vec{E}_p = c_1(\theta) \cos \Theta \sin \theta + c_2(\theta) \sin \Theta \cos \theta \cos(\varphi - \Phi) \quad (6.1a)$$

$$\vec{E}_s = c_3(\theta) \sin \Theta \sin(\varphi - \Phi). \quad (6.1b)$$

with their complex conjugates \vec{E}_p^* and \vec{E}_s^* . For radiation into upper half-space, here air with $n_1 = 1$, the coefficients are

$$c_1^\uparrow = \frac{1}{\Pi(\theta)} + r_p \Pi(\theta) \quad (6.2a)$$

$$c_2^\uparrow = \frac{1}{\Pi(\theta)} - r_p \Pi(\theta) \quad (6.2b)$$

$$c_3^\uparrow = -\frac{1}{\Pi(\theta)} + r_s \Pi(\theta) \quad (6.2c)$$

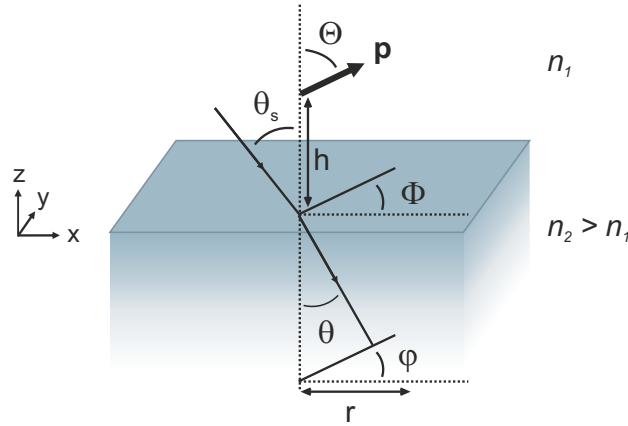


Figure 6.5: Coordinate system of the calculations for a dipole with dipole moment \vec{p} near an interface. A photon is emitted at a polar angle θ and azimuthal angle φ to the optical axis. Θ is the polar angle and Φ the azimuthal angle of the dipole axis.

where

$$\Pi(\theta) = e^{-ikn_2 \cos \theta h} \quad (6.3)$$

with the vacuum wavevector $k = 2\pi/\lambda$ and the z coordinate h of the dipole above the interface. For radiation into lower half-space, in our case glass with $n_2 = 1.5$, the coefficients emerge as

$$c_1^\downarrow = n^2 \frac{\cos \theta}{\cos \theta_s} t_p \Pi_s(\theta_s) \quad (6.4a)$$

$$c_2^\downarrow = n t_p \Pi_s(\theta_s) \quad (6.4b)$$

$$c_3^\downarrow = -n \frac{\cos \theta}{\cos \theta_s} t_s \Pi_s(\theta_s) \quad (6.4c)$$

where $n = n_2/n_1$ is the relative index of refraction and

$$\Pi_s(\theta_s) = e^{ikn_1 \cos \theta_s h}. \quad (6.5)$$

θ_s is linked to θ by Snellius' law

$$\frac{\sin \theta_s}{\sin \theta} = \frac{n_2}{n_1}. \quad (6.6)$$

The Fresnel coefficients for reflection and transmission in non-magnetic media are given by [72]

$$r_p = \frac{n_2 \cos \theta_s - n_1 \cos \theta}{n_1 \cos \theta + n_2 \cos \theta_s} \quad (6.7a)$$

$$r_s = \frac{n_1 \cos \theta - n_2 \cos \theta_s}{n_1 \cos \theta + n_2 \cos \theta_s} \quad (6.7b)$$

$$t_p = \frac{2n_1 \cos \theta_s}{n_1 \cos \theta + n_2 \cos \theta_s} \quad (6.7c)$$

$$t_s = \frac{2n_1 \cos \theta_s}{n_1 \cos \theta_s + n_2 \cos \theta}. \quad (6.7d)$$

The powers radiated into air (\uparrow) and the substrate (\downarrow) are then given by

$$P^\uparrow(\varphi, \Theta, \Phi) \propto \vec{E}_p^\uparrow \vec{E}_p^{\uparrow*} + \vec{E}_s^\uparrow \vec{E}_s^{\uparrow*} \quad (6.8a)$$

$$P^\downarrow(\varphi, \Theta, \Phi) \propto \vec{E}_p^\downarrow \vec{E}_p^{\downarrow*} + \vec{E}_s^\downarrow \vec{E}_s^{\downarrow*}. \quad (6.8b)$$

In our experiment, the intensity distribution is imaged in the back focal plane of a $f = 300$ mm lens. This yields $\sin \theta = r/f$ for the radial distance r from the optical axis. To obtain the intensity distribution as observed in an experiment from equation 6.8, an apodization factor $1/\cos \theta$ needs to be added for energy conservation [154]:

$$P(r, \varphi, \Theta, \Phi) \propto \frac{1}{\cos \theta} \left(\vec{E}_p \vec{E}_p^* + \vec{E}_s \vec{E}_s^* \right). \quad (6.9)$$

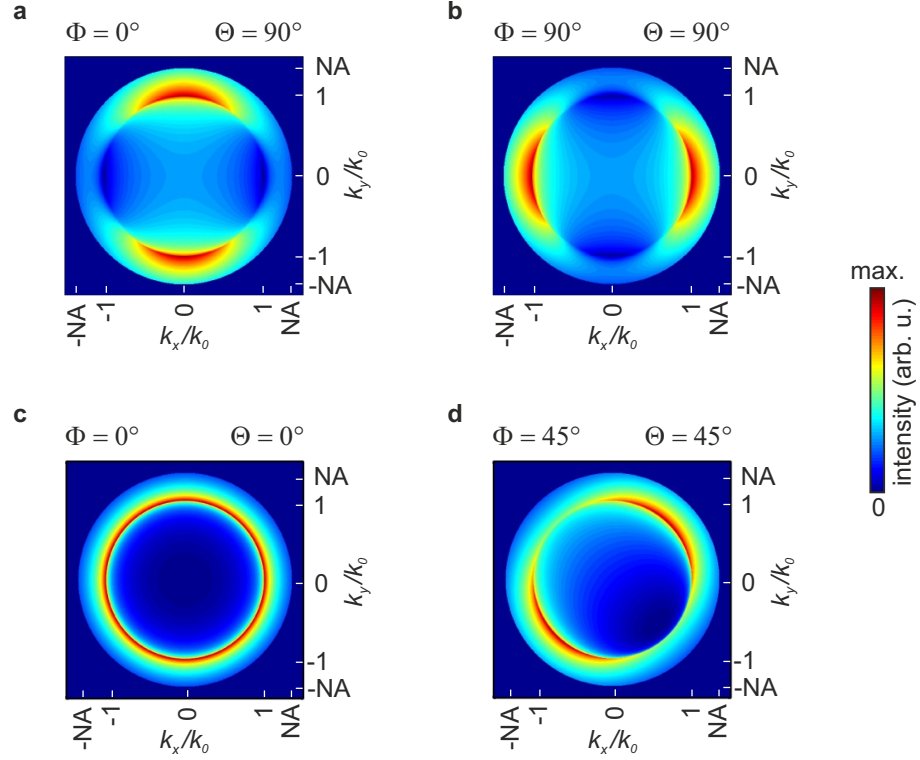


Figure 6.6: Normalized radiation patterns of a dipole at an interface oriented **a)** horizontal along x , **b)** horizontal along y , **c)** vertical along z , and **d)** tilted. Emission wavelength is $\lambda = 400$ nm and dipole height $d = 15$ nm. The maximum k vector is given by $\text{NA} = 1.35$.

For different dipole orientations, the resulting radiation patterns as calculated from the above relations are shown in figure 6.6. The dipole orientation is clearly reflected in the intensity distribution within the pattern. For example, from the two horizontal dipole orientations in figure 6.6a and b, one sees that most of the light is radiated into two lobes perpendicular to the dipole axis. In return, conclusions about the dipole orientation can be drawn from measured emission patterns. The apparent discontinuity in the pattern at $\text{NA} = 1$ corresponds to the critical angle $\theta_c = \arcsin(n_1/n_2)$ of total internal reflection at the interface. The intensity at angles larger than the critical angle arises from the excitation of propagating waves in the substrate by evanescent fields of the dipole, which is called forbidden light [148]. The efficiency of this conversion decreases exponentially with increasing distance of the dipole from the interface. In our case, the particle, i. e. the dipole, is located almost directly at the interface so that even most of the light is radiated at supercritical angles $\theta > \theta_c$ beyond

$NA = 1$. Note that this results in complex-valued θ_s according to Snellius' law. According to the height of the nanostructures $h = 30$ nm, all patterns in this thesis are calculated for dipoles at a distance of 15 nm to the interface, corresponding to emission from the center of the structure.

Regarding our work, we have extended the above method to include a finite number of dipoles. They are defined by their relative position as well as their orientation and dipole moment. If more than one dipole is considered, first the fields radiated from the individual dipoles are computed according to equation 6.1. Here, only the dipole orientation and distance to the interface is relevant. In a second step, the fields are weighted by the corresponding dipole moment and shifted to the position of the respective dipole before adding up the individual fields to the total fields \vec{E}_p and \vec{E}_s . A position shift results in a relative phase factor $e^{-i\vec{k}\Delta\vec{r}}$. As the phase is accounted for throughout the calculation, the fields from the individual dipoles can interfere on the nanoscale. Finally, the intensity distribution is computed according to equation 6.9 from the total fields. No example is shown here as this topic is discussed in detail in section 7.2.

6.4 FINITE ELEMENT METHOD CALCULATION OF THE NONLINEAR RESPONSE

As discussed in section 5.3, there are analytical solutions to Maxwell's equations for the interaction of light with nanoparticles. However, these are limited to few special cases, such as spherical particles and homogeneous environments. To calculate the optical response or the electromagnetic fields for a wide range of nanostructures, numerical methods need to be considered. Amongst a variety of different techniques, a finite element method (FEM) is well suited for our applications.

In brief, in the finite element method a system is subdivided into smaller parts, the finite elements, which are flexible in size. Solutions to the problem are then found by solving the boundary value problem for partial differential equations for these elements. All models and simulations presented in the following and in chapter 7 have been developed and carried out by Thorsten Schumacher with the commercial software package 'Comsol Multiphysics'. Detailed information about the FEM method can be found in his dissertation [155].

In our simulations, we would like to calculate the nonlinear electric fields of individual gold nanoparticles. As dielectric function of gold, we rely on the data reported by Johnson and Christy [136].

We compute the solutions to Maxwell's equations in frequency domain and under plane wave excitation to obtain the electric field at a certain frequency ω_0 as superposition of incident and scattered field. The electric field is related to the linear polarization, given by

$$\vec{p}^{(1)}(\vec{r}, \omega_0) = \epsilon_0 \chi^{(1)} \vec{E}(\vec{r}, \omega_0) \quad (6.10)$$

$$= \epsilon_0 \chi^{(1)} \vec{E}(\vec{r}) e^{i\omega_0 t}. \quad (6.11)$$

On a microscopic scale, each volume element can be interpreted as a dipolar scatterer which carries a dipole moment scaling with the local electric field. The linear polarization is then simply the average dipole moment per unit volume. Based on the anharmonic oscillator model used in previous work [151, 150], each dipole serves as nonlinear oscillator and generates nonlinear polarization [155]. Consequently, the third-order polarization $\vec{p}^{(3)}$ can be calculated from the linear polarization as

$$\vec{p}^{(3)} \propto \left(\vec{p}^{(1)}\right)^3 \propto \left(\chi^{(1)}\right)^3 \vec{E}^3(\vec{r}) e^{i3\omega_0 t}. \quad (6.12)$$

$\vec{p}^{(3)}$ is a complex vector carrying amplitude and phase, and oscillates with $3\omega_0$. This third-harmonic polarization corresponds to a nonlinear field inside the material and is the source of third-harmonic generation [155, 156]. Note that we assume a flat dispersion of the susceptibility $\chi^{(3)}$ and consider materials with no second-order processes. To account for varying efficiencies of the third-order process at different frequencies, usually a normalization factor is included in equation 6.12. However, frequency dependencies and total amplitudes of the third-harmonic generation are not relevant for our investigations, so that this normalization can safely be neglected.

While the method gives out the linear field around the structure, the nonlinear field, i. e. the field generated by the nonlinear polarization, cannot be straightforwardly computed. To simulate the nonlinear field outside the structure, the third-harmonic polarization in the structure is set as boundary value for a new calculation, solving the system at $3\omega_0$.

As an example, the simulated linear and nonlinear fields of a resonantly excited gold nanostructure are shown in figure 6.7. Throughout this thesis, all field plots show a cut through the structure at $z = 15$ nm. Moreover, we use different colormaps to clearly distinguish between the linear and nonlinear fields. As we always consider field distributions and not absolute values of the fields,

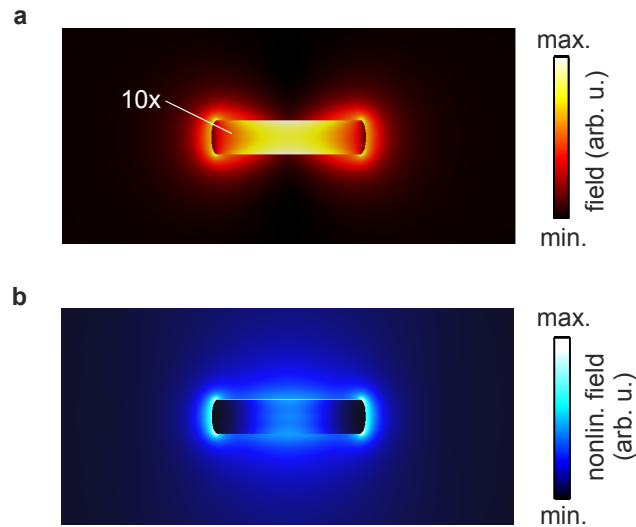


Figure 6.7: Finite element method simulation for a 270 nm long gold nanoparticle on a glass substrate, excited at the fundamental plasmon resonance. Shown are the computed a) linear response and b) nonlinear response at the third harmonic. The linear field inside the particle is scaled up by a factor of ten for better visibility.

the colorbars will be omitted in the next chapter. In figure 6.7, the nonlinear field inside the particle corresponds to the linear field cubed whereas the nonlinear field outside the particle is the result of a separate calculation at $3\omega_0$. For the simple case shown here, the distribution of the nonlinear field is similar to the linear one, which, however, is not always true. This gives new opportunities to shape nonlinear fields on the nanoscale, as discussed in section 7.5.

This chapter is based on our publication *Shaping the nonlinear near field* in Nature Communications (2016) [33].

Light scattering at plasmonic nanoparticles and their assemblies has led to a wealth of applications in metamaterials [4, 5] and nano-optics [133, 157]. While the focus of most studies still lies on the linear optical properties of the nanostructures, the field of nonlinear plasmonics which was introduced in section 5.3 is still growing. Many very interesting aspects of the nonlinear processes in plasmonic nanostructures were studied during the last years [26]. Especially the spectral dependence [158, 151] and the enhancement of the nonlinear signals [152, 153] has been investigated in detail. Although shaping of linear as well as nonlinear fields around nanostructures is widely studied [13, 159, 160, 161, 149], the influence of the field inside the nanostructures is often overlooked. In this chapter, we present a new approach to nanoscale field shaping based on higher harmonics generation in single elongated structures taking into account higher order plasmonic modes.

We now have the theoretical background and relevant methods at hand to start a detailed investigation of the nonlinear properties of plasmonic nanostructures. After introducing the experimental technique, essential results regarding single resonant nanorods are presented in section 7.1. These particles form the building blocks of the nonlinear plasmonic double slit experiment (see section 7.2) where, in analogy to classical diffraction experiments, interference between different emitting centers is observed. That way, it constitutes a very sensitive tool to measure the separation between the emitters. As a side effect, this method allows us to precisely determine the spatial origin of the nonlinear signals. The quality of our calculations with respect to the experimental resolution is discussed in section 7.3. Finally, we show in section 7.4 that the third-harmonic emission from an individual extended nanostructure can be switched between different configurations. Due to the higher order process, the concomitant nonlinear near fields switch accordingly, offering great potential to control field distributions from a single nanostructure alone (see section 7.5).

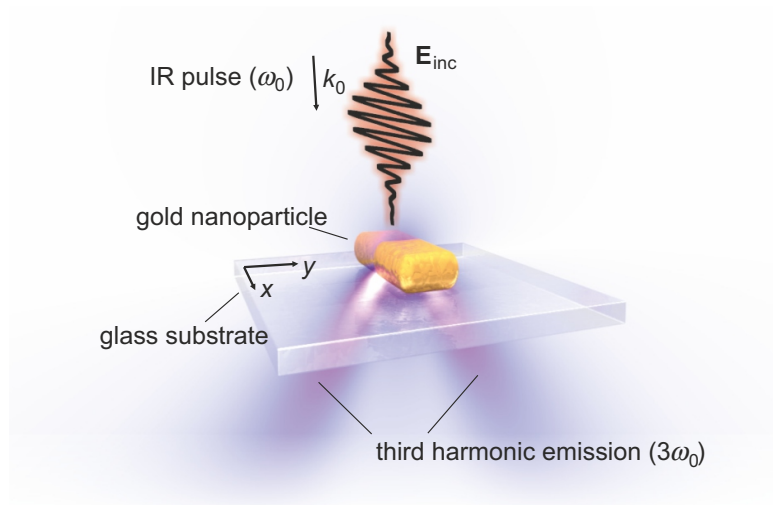


Figure 7.1: Schematic illustration of the experiment.

7.1 NONLINEAR EMISSION PROPERTIES OF A SINGLE PARTICLE

The basic working principle of our experiments is shown schematically in figure 7.1. The nanostructures are fabricated on a glass substrate using electron beam lithography. In a first step, we consider 270 nm long nanorods with 60 nm width and 30 nm height. The sample is excited with a focused beam of infrared pulses. Here, the excitation wavelength is fixed at 1170 nm. The polarization of the excitation is chosen parallel to the long axis of the nanorods, excitation power is ≈ 2.5 mW unless otherwise stated. The generated nonlinear radiation is emitted into the substrate and collected with a high-NA objective.

7.1.1 Spectrum: contributions and power dependence

An SEM image of the investigated rod structure is shown in figure 7.2a. The dimensions agree well with the nominal values. The fundamental dipolar plasmon resonance is excited resonantly in the rod at an excitation wavelength of 1170 nm, as can be seen in the calculated field distribution.

The measured spectrum in the visible wavelength regime is shown in figure 7.2b. We can identify three contributions in the nonlinear signal. The narrow peaks at half (585 nm) and one third (390 nm) of the excitation wavelength correspond to second and third harmonic generation, respectively. This manifests in the expected square and cubic dependence of the signals on the excitation power (see figure 7.3). Although gold as well as the structure itself is centrosymmetric and hence should not exhibit a signal at the second harmonic, we see a distinct SHG

peak. We attribute this to the fabrication process which inevitably leads to surface roughness and irregularities in shape. This is confirmed by a strong variation in the SHG signal from nominally equivalent particles. Due to the higher efficiency of the second order process, the SHG signal can be comparable to the signal at the third harmonic. In fact, symmetry-forbidden SHG from gold nanostructures has been observed in quite a number of studies, see for example [162, 163, 164]. Apart from fabrication inaccuracies, it is also attributed to the near field around the nanostructures, allowing for contributions from actually symmetry-forbidden tensor components [165]. However, the origin of these signals is still under debate. In addition to the higher harmonics generation, the spectrum shows a broad luminescence background. Due to the low energy of the excitation photons, this response must arise from a multiphoton process. As the signal extends down to the third harmonic wavelength, we suggest that the luminescence is induced by absorption of three photons, resulting in a three photon photoluminescence (3PPL) signal [166, 167]. Looking at the power dependence of the signal in figure 7.3b, indeed a cubic law shows a good agreement with the measured data. At low powers, the signal vanishes in the noise. Also the non-linear luminescence response varies between individual particles and is strongly influenced by the nanoscopic geometry of the structures [167, 168].

In conclusion, we have seen that both SHG and the observed multiphoton luminescence seem to be determined by surface effects and fabrication inaccuracies and therefore do not fall within the scope of our investigations. Hence, we will focus on the THG signal which is symmetry-allowed and very homogeneous.

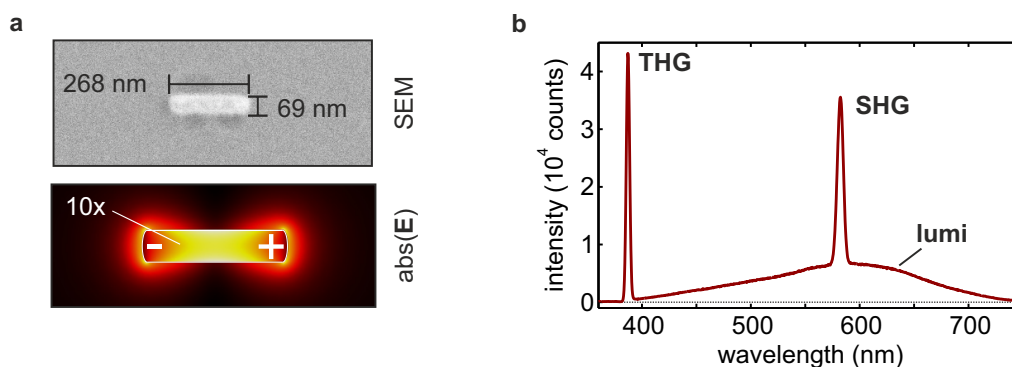


Figure 7.2: **a)** SEM image of the investigated structure and FEM calculation of the electric field around an equivalent structure excited at the fundamental plasmon resonance. The field inside the structure is scaled up by a factor of ten for better visibility. **b)** Measured spectrum of the 270 nm long rod at 1170 nm excitation, showing the main contributions to the nonlinear signal.

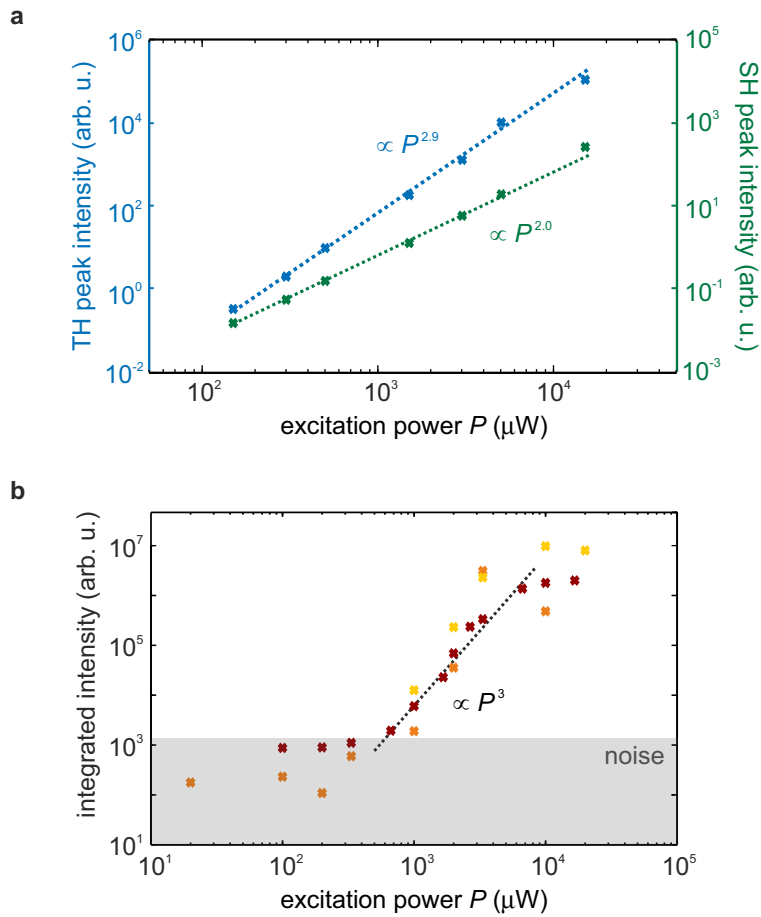


Figure 7.3: Power dependence of the signals. **a)** THG and SHG: plotted are the peak values extracted from a Lorentzian fit. Dotted lines are power law fits. **b)** Luminescence: plotted is the integrated intensity between 420 and 750 nm after subtraction of the SHG peak. The colors represent three nominally equivalent particles. Dotted line is a guide to the eye.

7.1.2 Emission properties – back focal plane images

Regarding the emission properties of the single nanorod, we use a narrow band-pass filter (center 390 nm, width 18 nm) to investigate the third-harmonic light only. The radiation patterns are acquired using the spectrograph with a mirror instead of a grating.

The measured back focal plane image of an individual nanorod excited at the fundamental dipolar plasmon resonance is shown in figure 7.4a. Note that all measured and calculated emission patterns in this chapter are normalized to their maximum since we are interested in the intensity distribution within the pattern only. The colorbars as well as the axis labeling will therefore be omitted in the following. As discussed in the methods section, most of the light is radiated into the substrate under supercritical angles beyond $NA = 1$ (see section 6.3). The two lobes in k_y direction hint at an orientation of the radiating dipole moment along the x axis, coinciding with the orientation of the rod and the excitation polarization. Figure 7.4b shows the emission pattern calculated for a single dipole 15 nm above the air-glass interface. Obviously, the simple case of a single dipole yields very good agreement with the measured pattern. To understand this, we consider the calculated linear field of the nanorod as shown in figure 7.4b. At the plasmon resonance, the linear field outside the particle peaks

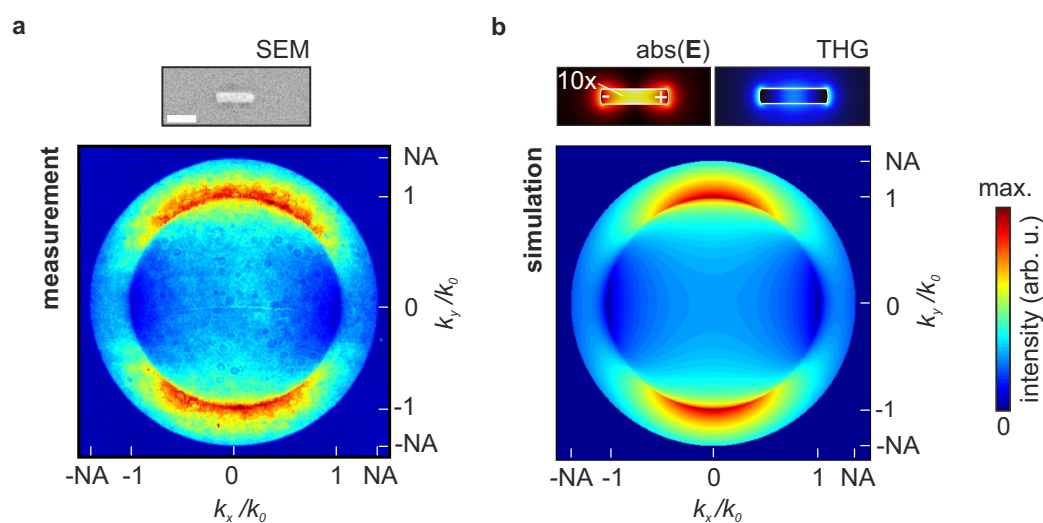


Figure 7.4: Nonlinear plasmonic analog of a single slit. **a)** Back focal plane image of the third harmonic light of a 270 nm long gold nanorod for an excitation wavelength of 1170 nm. Scale bar in the SEM image is 200 nm. **b)** Emission pattern of a dipole at an interface for 390 nm emission wavelength. Shown are also the calculated linear and nonlinear fields.

at the ends of the rod, forming hot spots. However, the field inside the particle is the crucial parameter for nonlinear effects. In stark contrast to the external field, it is highest in the center of the rod. Consequently, also the third-order polarization which scales with the third power of the field is enhanced in the center. The simulation hence predicts the nonlinear light to be emitted from the center region of the rod. Since this region is small compared to the emission wavelength, the good agreement with a single dipole calculation is not surprising.

We therefore conclude that it is the high field inside the gold structure that causes third-harmonic generation. The emission properties of a single resonantly excited nanorod can simply be described by a single dipole oriented parallel to an interface.

7.2 NONLINEAR PLASMONIC ANALOGUE OF YOUNG'S DOUBLE SLIT

As discussed in section 5.2, higher harmonics generation is a coherent process so that the third harmonic light is coherent with the exciting laser light. The coherence manifests impressively when a nanorod pair as shown in the SEM image in figure 7.5a is considered.

The observed back focal plane image is now distinctly altered: evidently, a pattern of dark and bright stripes is superimposed onto the two-lobed dipolar pattern. In the simulation, the nanorod pair corresponds to two dipoles with a distance equivalent to the particle separation. Since the rods are excited coherently by the same laser focus and hence emit coherently, the dipoles oscillate in phase and have the same orientation and dipole moment. As shown in figure 7.5, the calculated emission pattern is in good agreement with the measurement regarding the position of the extrema as well as the intensity distribution within the pattern.

Comparing our experiments to classical diffraction experiments, we see that an individual nanorod acts similar to a single slit or even a point source of third harmonic light. Consequently, a nanorod pair combines two emitting centers and constitutes the nonlinear plasmonic analogue of Young's double slit. In this classical experiment, the coherent emission from two slits interferes due to the wave nature of light and a characteristic pattern of dark and bright stripes can be observed in the far field. The emerging Fraunhofer diffraction pattern corresponds to the Fourier transform of the apertures [169]. The shape and intensity distribution of the interference pattern in the far field is thus uniquely related to both width and separation of the slits as well as their relative phase.

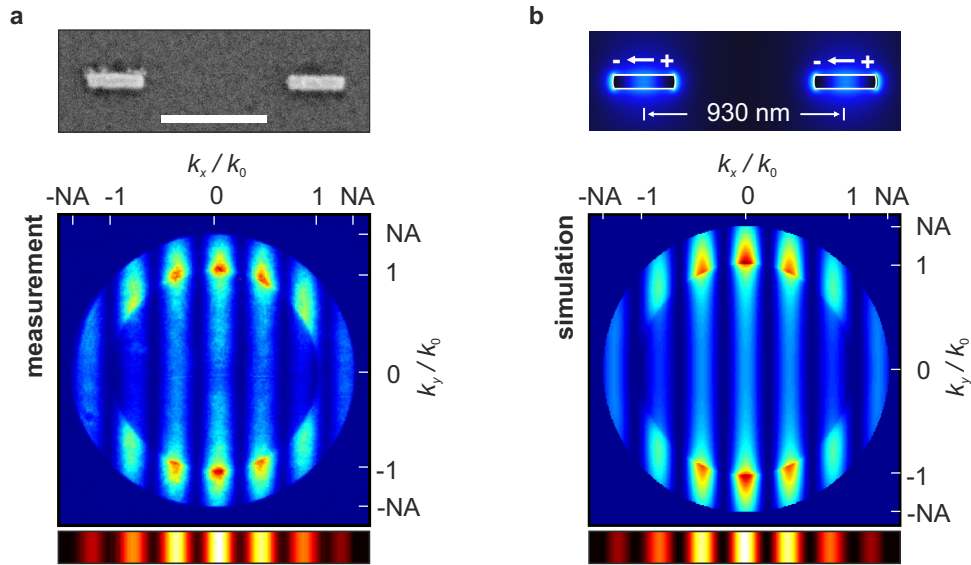


Figure 7.5: Interference in the emission pattern of a pair of nanorods. Distance is 930 nm. a) Measured back focal plane image. Scale bar in the SEM image is 500 nm. b) Calculated radiation pattern for two dipoles oscillating in phase.

In our double slit analogue, we cannot straightforwardly vary all parameters. The slit width as well as the emission wavelength is determined by the plasmon mode. A relative phase between the two rods could be induced by a more complex excitation geometry, for example using the steep curvature of the wavefronts near the focal plane of a tightly focused laser beam [170]. Here we are limited by the low NA of our excitation lens which does not allow for noticeable phase differences. However, the nanorod separation can easily be varied with electron beam lithography, simply by fabricating a series of pairs of identical particles with increasing separation. The lower limit of the separation is given by the rod dimension and a minimum gap of 60 nm to avoid plasmon coupling. The maximum separation is determined by the size of the laser spot. Hence, we can safely vary the nanorod separation between 330 nm and 930 nm. The full series of measured and calculated emission patterns is shown in figure 7.6.

For a more detailed analysis, we condense the information contained in the emission patterns by studying the projection of the patterns onto the k_x axis as shown in the bottom row of figure 7.5. All information about the interference process and hence the changes related to the distance variation is contained in the x direction whereas the y direction only displays the two-lobed dipolar pattern. Hence, no relevant information is lost due to the projection. The resulting inten-

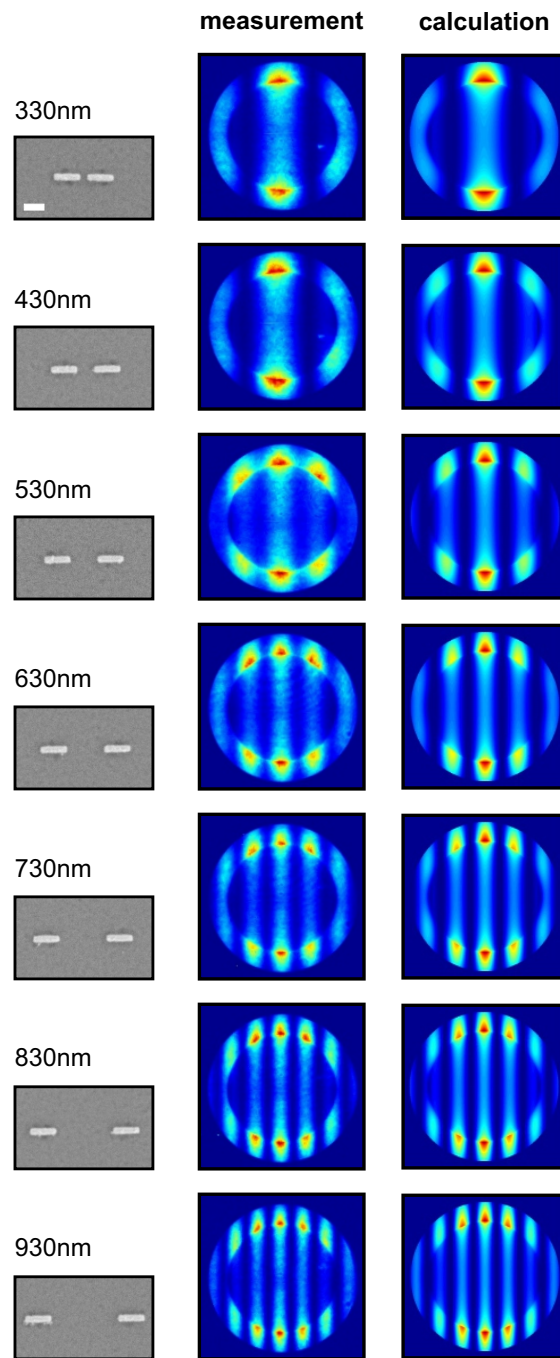


Figure 7.6: Full series of measured and calculated emission patterns for the plasmonic double slit analogue in a side-by-side arrangement. Scale bar is 200 nm.

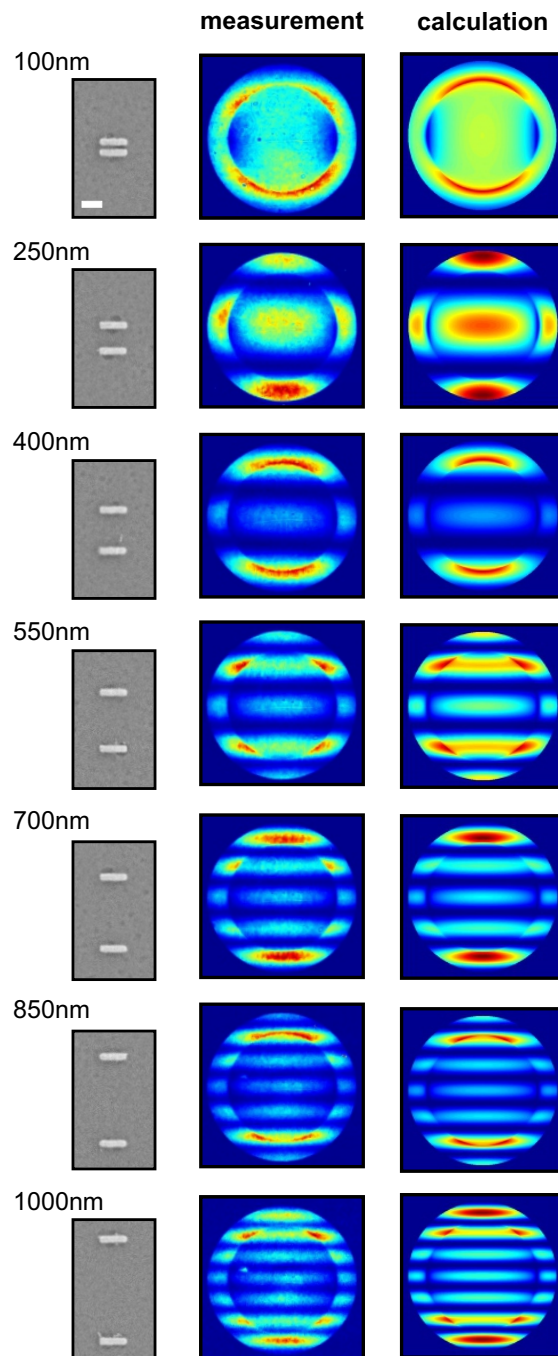


Figure 7.7: Full series of measured and calculated emission patterns for the plasmonic double slit analogue in a stacked arrangement. Scale bar is 200 nm.

sity profiles for the smallest and the largest rod distance are shown in figure 7.8a. In these intensity profiles, the correspondence to the classical experiments becomes even more apparent. The agreement between the intensity profiles from experiment and theory is convincing. In the radiation patterns as well as the intensity profiles, we see that with increasing nanorod separation, the number of side maxima and hence also the number of minima increases. Apart from the number, especially the exact position of the minima depends strongly on the separation of the emitting centers. As shown in figure 7.8b, there is a good agreement regarding number and position of the minima between measurements and simulations for rod pairs of all distances between 330 and 930 nm. The careful analysis of the interference pattern thus allows us to accurately measure emitter distances which are smaller than the diffraction limit of the excitation light. That way, the double slit analogue experiment further confirms the centers of the rods as sources of the nonlinear signal. This issue will be further discussed in the next section.

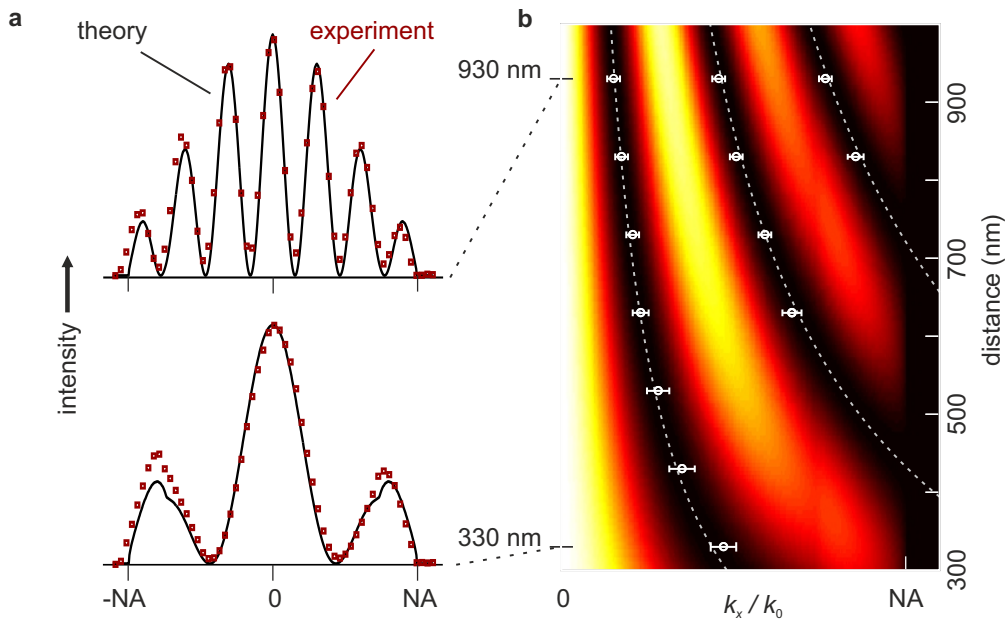


Figure 7.8: Distance dependence of the nonlinear plasmonic double slit. **a)** Measured (red squares) and calculated (black lines) intensity profiles for 330 and 930 nm distance, corresponding to cuts through the distance dependent intensity projection shown in **b)**. The squares and dashed lines indicate the positions of the minima from measurement and calculation, respectively. The error bars correspond to an increase to three times the noise level above the minimum.

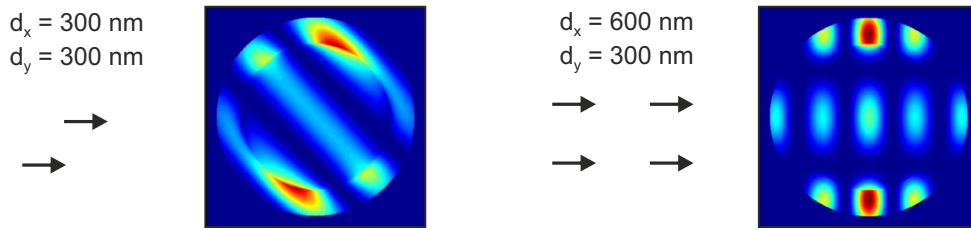


Figure 7.9: Nonlinear plasmonic ruler: calculated radiation patterns for two dipoles (left) as well as an array of four dipoles (right) with distances in x and y direction as indicated. Emission wavelength is 390 nm.

As an additional degree of freedom in our experiment, we can modify the spatial arrangement of the nanorods from side-by-side to stacked as shown in the SEM images in figure 7.7. Again, an interference pattern is superimposed onto the two-lobed dipole pattern. However, now the interference process takes place along the y direction so that the pattern of dark and bright stripes is rotated by 90° compared to figure 7.6. The sensitivity of the interference process towards the arrangement of the emitters can be exploited to determine not only distances but also the direction of the displacement as is demonstrated by the two exemplary cases in figure 7.9. That way, our method constitutes a nonlinear plasmonic ruler allowing to measure distances and angles between nonlinear emitters on the nanoscale.

Finally, we would like to emphasize that the observed interference effects rely fundamentally on the coherent nature of the higher harmonics light. Interference can also be observed in the SHG signal, however, less pronounced due to the higher wavelength and unclear origin of the signal. In contrast, the luminescence light is not coherent, leading to a homogeneous intensity distribution in the radiation pattern independent of the considered structure, as shown in figure 7.10.

7.3 LOCALIZING THE SPATIAL ORIGIN OF THG

7.3.1 *Surface versus volume effects*

As mentioned in section 7.1, the origin of the higher harmonics signals, especially that of SHG, is still under debate. Many plasmonic effects and applications are related to the strong local field enhancement in the vicinity of the nanostructures. These hot spots are also observed for our nanorod geometry as shown in figure 7.2a. Although both our experiments as well as the calculations sug-

gest the high internal fields and hence the particle volume as origin of the third harmonic signal, we would like to exclude possible contributions from surface effects at the ends of the nanorods.

To clarify this point, the measured radiation patterns are compared to different simulations, shown in figure 7.11. Obviously, the patterns agree best when assuming a dipole in the center of each nanorod, corresponding to emission from the particle volume. Emission from the ends of the particle is simulated by two dipoles for each rod, with a separation equivalent to the rod length. In case of the single rod structure, this yields two interference minima which are clearly not observed in the experiment. For the double slit analogue, the minima arising from the particle size are superimposed onto the interference pattern arising from the particle separation. This is in analogy to the influence of the slit width in the classical double slit experiment, where the double slit interference pattern is modulated by the single slit function. However, also here the intensity distribution within the pattern is best reproduced assuming emission from the centers, which was also reflected in the very good overlap between the intensity profiles from theory and experiment (see figure 7.8a). Overall, these simple considerations allows us to exclude contributions to the TH signal due to surface effects at the particle ends.

7.3.2 Narrowing down the spatial extent of the emission centers

To further elaborate on the spatial origin of the signal, we consider not only emission from the center and the ends of a rod, but vary the distance d of two dipoles between 0 nm (corresponding to emission from the center) and 270 nm (corresponding to the particle size) as shown in figure 7.12. That way, the sensitivity of our method towards the spatial extent of the emitting center can be estimated.

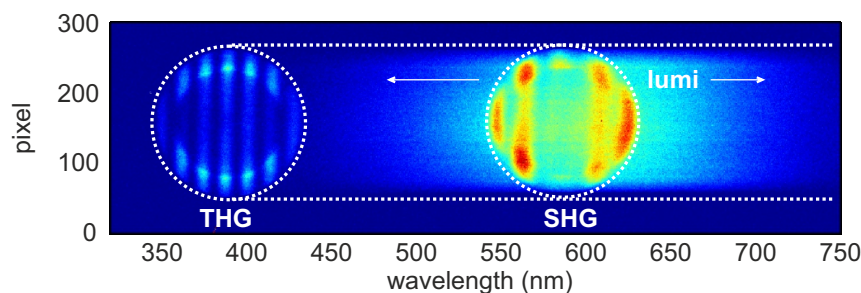


Figure 7.10: Nonlinear signal of a rod pair with 930 nm separation for 1170 nm excitation, resolved with a 150 grooves/mm grating. While interference effects are observed in the patterns at the TH and SH wavelengths, the luminescence leads to a broad, homogeneous background.

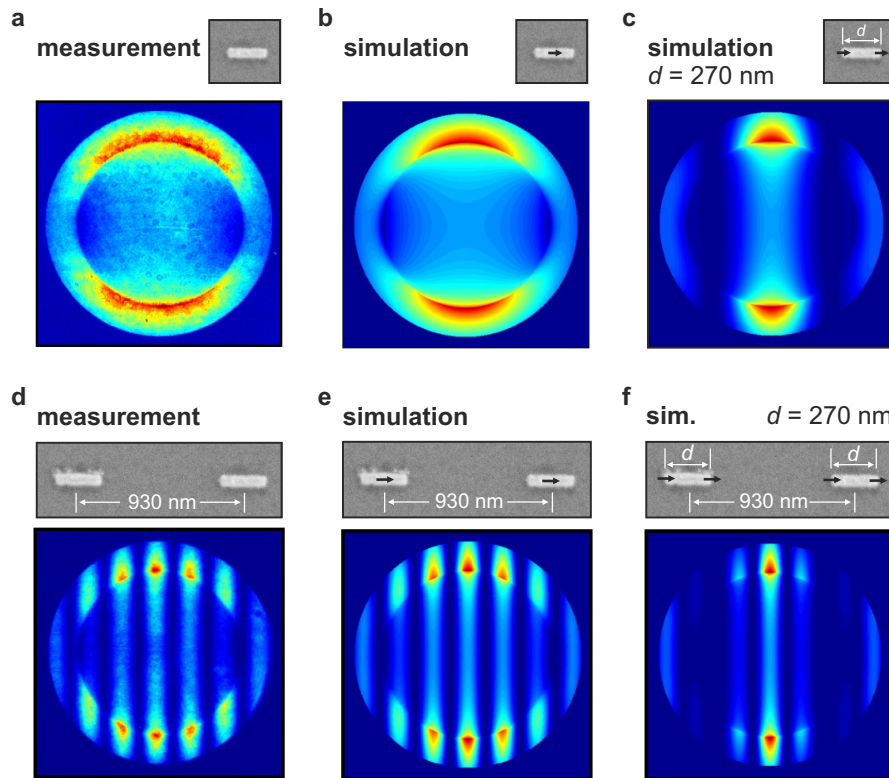


Figure 7.11: Ends vs center: full emission patterns of measurement and simulations with one and with two dipoles for the single 270 nm long rod in a)-c) and the double rod structure with a particle separation of 930 nm in d)-f).

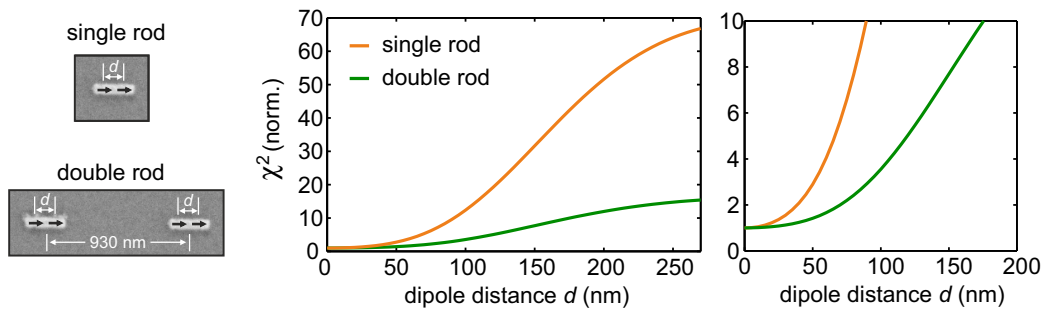


Figure 7.12: χ^2 deviation of the measured and calculated intensity profiles for the single (orange line) and the double rod structure with 930 nm separation (green line). Each rod is represented by two dipoles with varying distance between 0 nm and 270 nm. Intensity profiles are normalized before comparing data and calculation. χ^2 is normalized such that $\chi^2 = 1$ at $d = 0$ nm.

This study is analogous to a variation of the slit width in the classical diffraction experiments.

For the single and the double rod structure, we compare the measured intensity profiles with those obtained for the distance dependent calculation. As argued above, it is sufficient to consider the intensity profiles since all information about the interference process is retained in the projection onto the k_x axis. To quantify the agreement between the curves, the χ^2 deviation is evaluated. It is defined as

$$\chi^2 = \sum (I_c - I_m)^2$$

where I_c are the data points of the calculated profile and I_m the data points from the measurement. The intensity profiles I_c and I_m are normalized, so that χ^2 compares the shape of the profiles only. In the resulting curves shown in figure 7.12, χ^2 for the two different structures is normalized to the center emission case, so that $\chi^2 = 1$ for $d = 0$ nm. Consequently, the deviation quantifies the agreement of the profiles relative to the center emission case. This approach is justified as the unnormalized and hence also the normalized χ^2 for both structures reach the absolute minimum at $d = 0$ nm. Obviously, the deviation quickly increases with increasing dipole distance. Especially the close-up view on the right shows large deviations for dipole distances even below 100 nm. This behavior is more pronounced for the single rod structure, in accordance with the above reasoning regarding figure 7.11. Supporting this point, the χ^2 study clearly excludes emission from the ends of the rods. Furthermore, it allows us narrow down the spatial extent of the emitting center that can be resolved with our experiment to a value far below 100 nm.

7.3.3 *Quality of the single dipole approximation*

In fact, the size of the emitting centers is revealed in the finite element calculations of the nonlinear polarization in the nanorods, as shown in figure 7.4b and 7.5b. The nonlinear polarization is not a discrete function but is distributed over the particle, which strictly speaking rules out the definition of a spatial extent of the emission center. In this context, it is an intriguing question if our experiment is able to distinguish between a point-like emitter and a smeared out emission center with a finite extent. Completing the previous study, we now would like to estimate the quality of the individual dipole approximation by varying the dipole number in the calculation.

Figure 7.13 shows once more calculated radiation patterns, this time comparing the results obtained from single dipoles to that from an array of many dipoles. In figure 7.13b and e, the amplitudes and phases of the individual dipoles in the grid are chosen according to the FEM calculation of the nonlinear polarization

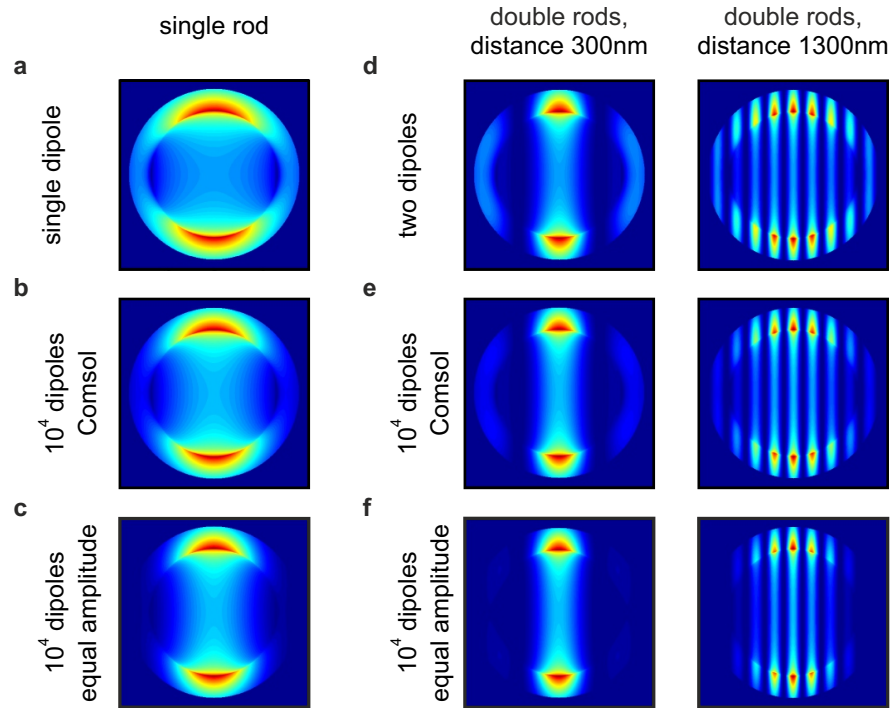


Figure 7.13: Influence of the dipole number. a), d) Calculated emission patterns from a single dipole and two dipoles corresponding to a single and two double rod structures with different separation, respectively. Calculated emission patterns from 10^4 dipoles arranged in a 1 nm grid where amplitude and phase of the dipoles b), e) corresponds to the nonlinear polarization calculated with FEM or c), f) is constant, simulating homogeneous emission from the whole rod.

in the nanorods (see figure 7.4b and 7.5b). The difference between the patterns obtained with the single dipoles and the array with this "real" distribution of dipole moment is marginal. For comparison, figure 7.13c and f show the emission patterns assuming homogeneous emission from the whole volume of the rod. This is in analogy to a finite slit width which results in an envelope function for the interference pattern, as discussed above. Overall, increasing the number of dipoles considered in the calculation does not yield an improvement and the measured emission patterns are reproduced best by single dipoles.

In summary, we conclude that our assumption of single point-like dipoles yields very good results regarding the calculation of radiation patterns as the finite extent of the emitting spots is not resolved in our measurements. This allows us to refrain from FEM simulations and minimizes the computational effort.

7.4 SWITCHING THE EMISSION PROPERTIES OF A LONG ROD

In this section, we extend the scope of our investigation of the nonlinear emission characteristics of nanostructures beyond small rods and turn our attention towards elongated structures. Within the wavelength regime accessible in our experiments, these structures are not excited resonantly at the fundamental plasmon mode anymore, so that we deal with an unknown number and distribution of emitting centers. Whereas the experiments so far were restricted to excitation at 1170 nm, the excitation wavelength will be varied in the following. The bandpass filter is now removed and a grating disperses the light in the spectrometer. The convolution of spatial pattern and emission spectrum has little influence on the observed radiation patterns, as the emission spectrum at the third harmonic is very peaked.

Figure 7.14 summarizes the measurements of a 925 nm long gold rod. The angular emission pattern of the extended rod at an excitation wavelength of 1320 nm clearly displays the characteristic interference pattern of a double slit where both apertures emit in phase (see figure 7.14a). With the nonlinear ruler method presented above, the separation of the emitting centers can be determined according to the number and position of the minima in the interference pattern. This analysis hints at two emitting centers in a distance of approximately 600 nm, as indicated in the SEM image. When the fundamental wavelength is tuned to 1420 nm, we obtain an angular pattern that deviates only slightly from a single dipole, implying a dominant emission from the center of the rod (see figure 7.14c). Both conclusions are confirmed by numerical simulations of equivalent rod structures as shown in figure 7.14a and c.

Additional measurements were performed, covering the wavelength range 1170 – 1420 nm. To gain an understanding of the wavelength dependent behavior, we take the profiles corresponding to the emission patterns at 490 nm and 425 nm TH wavelength as templates for the states $|1\rangle$ and $|2\rangle$, respectively. The intensity profiles at all other wavelengths are then fitted by a linear superposition of these two limiting cases:

$$I_{\text{tot}} = (1 - a)|1\rangle + a|2\rangle.$$

Here, $n = 1, 2$ gives the number of emitting centers in the corresponding state $|n\rangle$ and a is the weight ($0 \leq a \leq 1$). The weight a at all measured wavelengths is determined by fitting the linear superposition to the measured data using a nonlinear Levenberg-Marquardt algorithm. The uncertainty in the fit parameter a is estimated by the algorithm and given by the square root of the diagonal element of the covariance matrix. Three times this standard deviation is given as error bars in the plot. As the patterns at 490 nm and 425 nm were chosen as base func-

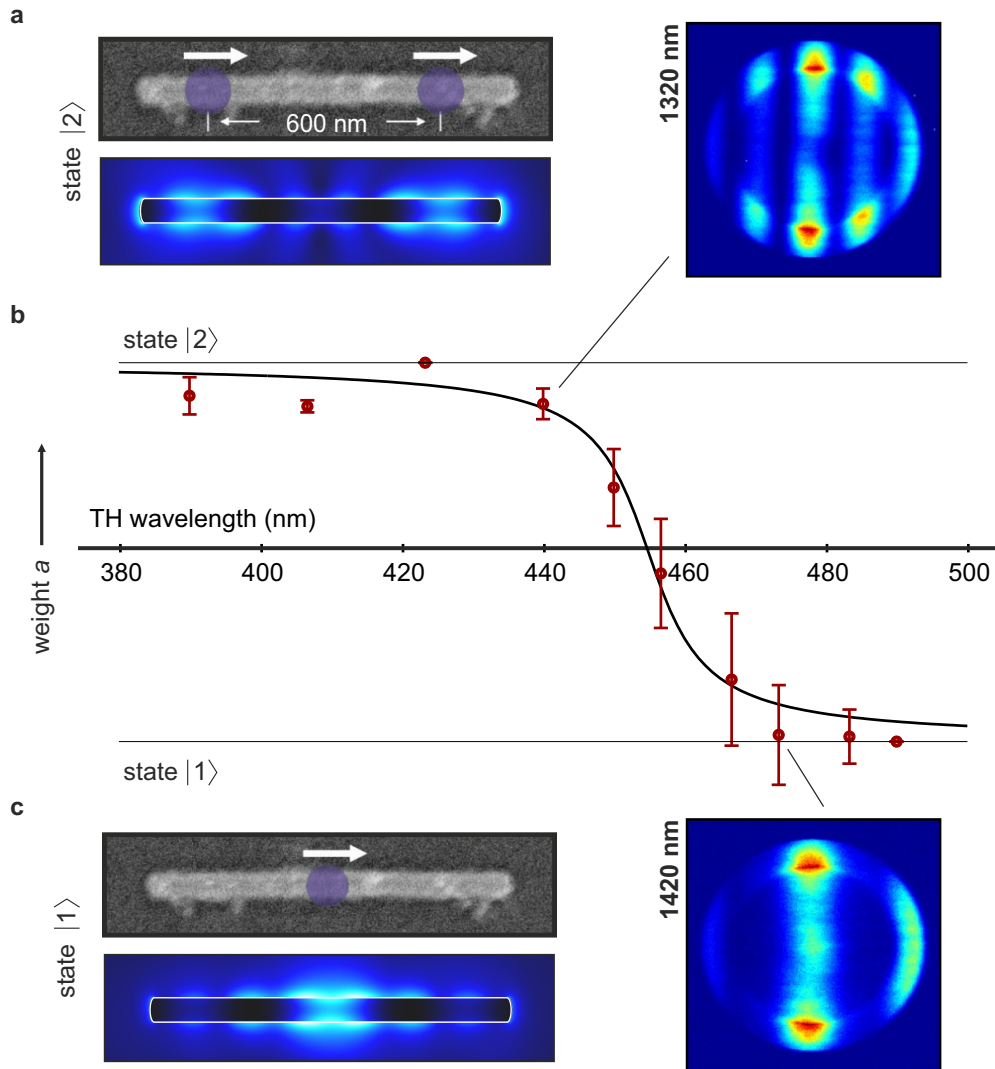


Figure 7.14: Switching of nonlinear emission. a), c) The emission pattern of a 925 nm long rod depends on the excitation wavelength. The two states $|1\rangle$ and $|2\rangle$ differ in the number of emitting spots, as indicated in the SEM images and the calculated TH fields. b) We observe a transition within a wavelength range of about 25 nm for the weight a of state $|1\rangle$ (red dots). The error bars are three times the standard deviation of the fit. The black line is a guide to the eye.

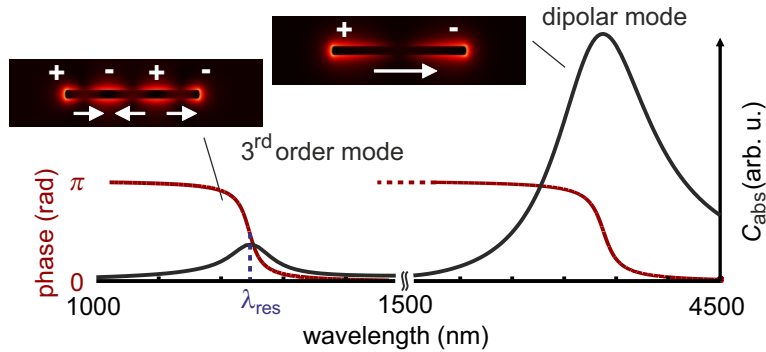


Figure 7.15: Calculated absorption cross section (black line) and phase of the third-order mode (red line) of a 925 nm long rod. The phase of the dipolar mode is not calculated but outlined for reference only. Insets: linear field distributions at the fundamental and the third-order resonance.

tions, the uncertainty vanishes at these wavelengths. As shown in figure 7.14b, the weight α obtained in this way displays a transition between a single emitting spot in the center (state $|1\rangle$) and two in-phase spots with well-defined separation (state $|2\rangle$). The transition is very steep, taking place within 25 nm at the third-harmonic wavelength. The full series of the measured emission patterns in dependence of the excitation wavelength is shown in figure 7.17b. The change of the interference pattern nicely displays the described switching from single to a double slit behavior, supporting our superposition ansatz.

To explain the switching of the emission pattern, we need to consider in more detail the modes of the fundamental field. We have discussed in section 5.3 that the modes of long nanorods resemble standing waves, where only odd modes can be excited optically in our configuration. As shown in figure 7.15, the dipolar mode is shifted far into the infrared, whereas the third-order mode shows a resonance in the wavelength regime where the experiments are carried out. When the excitation wavelength is tuned over a plasmon resonance, the phase of the mode changes by π . This behavior is in analogy to the phase change of a driven harmonic oscillator. In the vicinity of the third-order resonance, the third-order mode undergoes the phase change by π . In contrast, the phase of the fundamental dipolar mode is unaffected at wavelengths far away from the dipolar resonance. Tuning the excitation wavelength over the third-order resonance thus induces a relative phase of π between the two modes.

The field distribution at different wavelengths can be described with a simple dipole picture. We emphasize that this dipole picture used to describe the modes is different from the one considered for the calculation of the radiation pat-

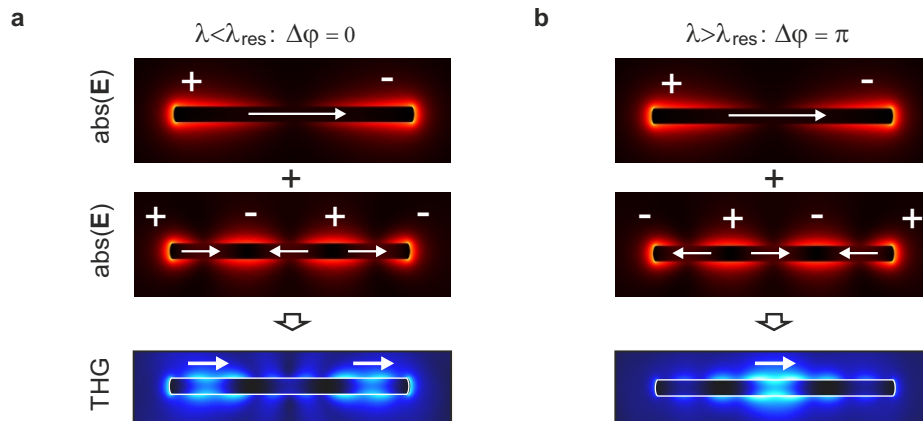


Figure 7.16: Illustration of the mode superposition in the long rod for excitation below (a) and above (b) the third-order resonance λ_{res} . Shown are the calculated linear field distributions at the dipolar and third-order resonance and the nonlinear fields at both sides of λ_{res} .

tern. Here, the dipoles indicate fields or current distributions in the rod, but are not automatically equivalent to emitting centers. The linear fields of the dipolar and the third-order mode then correspond to a single dipole and three counter-oscillating dipoles, respectively, as indicated in figure 7.15. In the considered wavelength regime, we always excite both modes with varying efficiency and observe their superposition. Figure 7.16 illustrates the situation at wavelengths below and above the third-order resonance. For wavelengths below the resonance, the overall phase between the modes vanishes. In the dipole picture, the single dipole and the inner dipole of the third-order mode oscillate against each other and cancel. As only the outer dipoles remain and generate a nonlinear signal, this corresponds to the double slit behavior. Above the resonance, the relative phase between the modes is π . Hence, the single dipole and the inner dipole of the third-order mode add up while the outer dipoles are weakened. The center dipole then dominates, which leads to the observed single spot emission pattern. In conclusion, the simple dipole picture fully describes the observed switching behavior. Both the relative amplitudes and the phase change around the higher order plasmon resonance must be taken into account to explain the experimental results.

Actually, the third-order plasmon resonance can be crossed in two ways as indicated by the dashed white lines in figure 7.17a: either by changing the excitation wavelength for a fixed rod length as discussed above or by changing the rod length for a fixed excitation wavelength. When tuning the plasmon resonance via the length of the nanorod, we observe the same transition of the

pattern from double to a single slit analogue as shown in figure 7.17c. This supports the explanation of the switching of the emission behavior of extended gold nanostructures by higher order plasmon modes. Moreover, the observed effects further prove that the high field regions in a plasmonic structure are the source of THG.

Finally, we note that the third-order resonance of the investigated structures is red-shifted compared to the calculation due to fabrication inaccuracies.

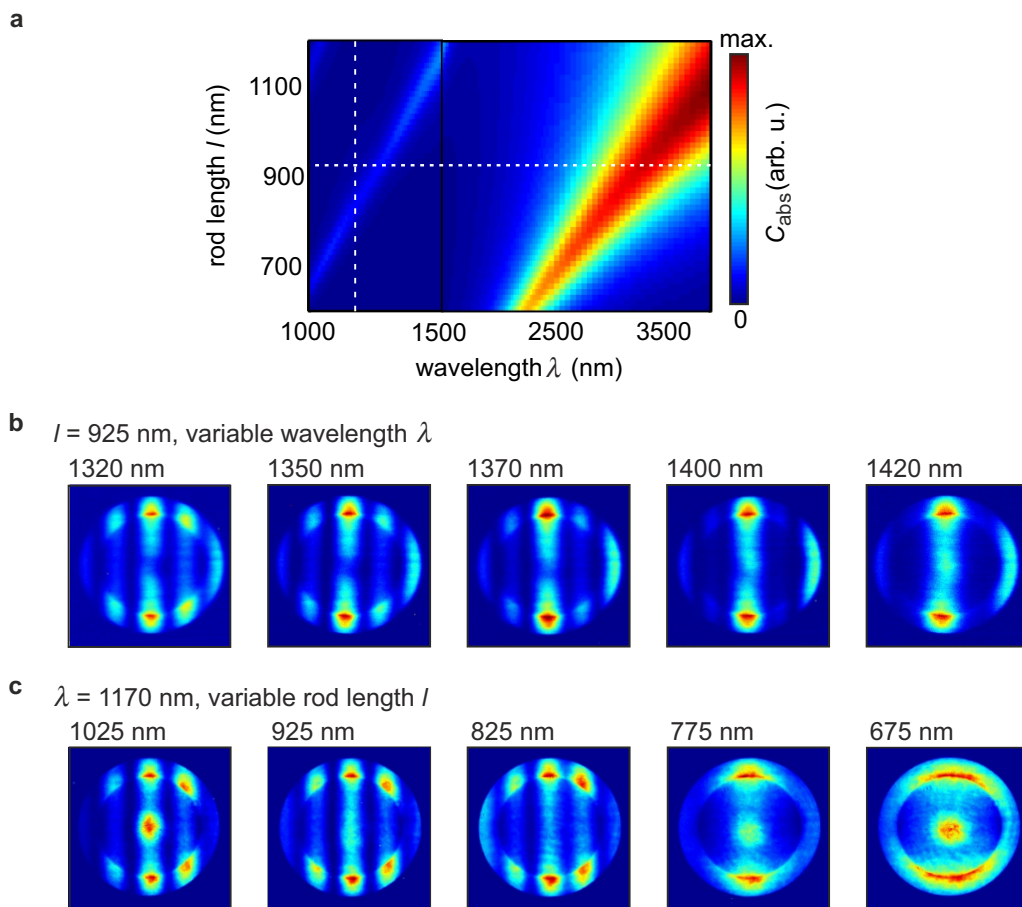


Figure 7.17: **a**) Calculated absorption cross section for different nanorod lengths. The wavelength regime has been divided into two parts with different resolution at 1500 nm, indicated by the solid black line. **b**) Radiation patterns measured at different wavelengths for a fixed rod length of 925 nm and **c**) at a fixed excitation wavelength of 1170 nm for different rod lengths.

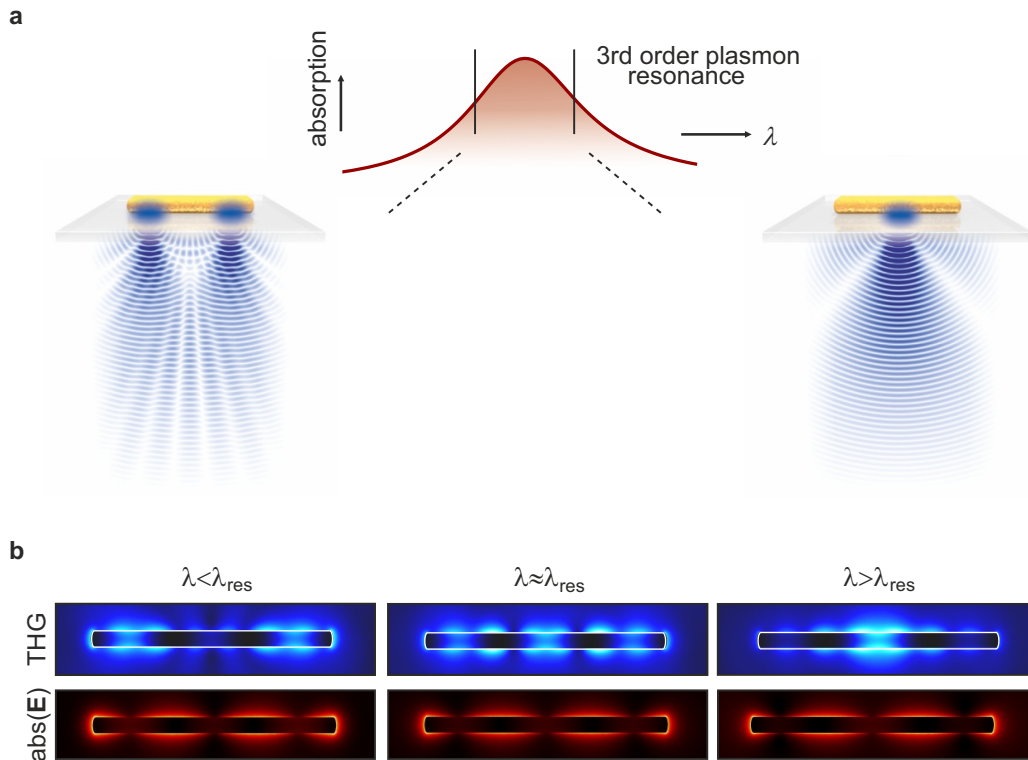


Figure 7.18: Nonlinear near-field and emission control. **a)** Slightly tuning the excitation wavelength over a plasmon resonance drastically changes the far-field response of a simple plasmonic structure. In our experiment, we switch between a configuration with one single and two separated emitting centers. **b)** While the linear fields are almost unaffected, the emitting centers and the concomitant nonlinear near-fields strongly depend on the excitation wavelength.

7.5 NONLINEAR NEAR-FIELD SHAPING

In the previous section, we have discussed how the nonlinear emission properties of an extended rod structure can be switched between different configurations by slightly varying the excitation wavelength. A summary of the experiment is given in figure 7.18a.

It is interesting to consider the behavior of the fields related to the response of the nanostructure. Figure 7.18b shows the linear field at the excitation wavelength as well as the fields at the third harmonic. These nonlinear fields are generated by the nonlinear polarization in the particle which calculates as the third power of the linear polarization in the material (see equation 6.12 and

section 6.4). Evidently, the distribution of the linear local field is hardly affected by the wavelength variation in the vicinity of the higher order resonance. However, the nonlinear third-order process of third-harmonic generation amplifies amplitude and phase differences of the fundamental field inside the rod. Although the differences are minor at the fundamental, the cubic dependence leads to drastic modifications in the distribution of the nonlinear polarization. Consequently, the third-harmonic emission properties and the concomitant near-fields at the third harmonic switch between different configurations as demonstrated by the numerical simulations shown in figure 7.18b.

Whereas the shaping of linear and nonlinear fields by complex assemblies of nanoparticles is common, our method enables field shaping with a single nanostructure alone by engineering distribution of the fundamental field inside the structure. It hence extends the range of well-established approaches in view of opportunities and potential applications in nanophotonics.

7.6 CONCLUSIONS AND OUTLOOK

In this chapter, we have presented an overview of our studies on the nonlinear emission properties of plasmonic nanostructures. Due to the coherent nature of the signals from different emitting centers, interference effects are observed in the far field. These can for example be exploited to localize the spatial origin of the nonlinear signals, that way gaining a deeper understanding of the physical processes in nonlinear plasmonics. Here, our experiments confirm the high internal fields as source of the nonlinear signals, which are well described by individual dipolar point emitters. Due to the high sensitivity of interference signals, our technique constitutes a nonlinear plasmonic ruler which allows to precisely measure distances, angles, and phases between emitting spots. In further experiments, we have shown that the emission properties of an elongated plasmonic structure can be switched between different configurations, in analogy to a light switch on the nanoscale. Of particular interesting here are the related nonlinear fields, which exhibit the same switching behavior. In addition to established methods based on assemblies of nanoparticles, nanoscale fields can hence be shaped with similar efficiency using a single nanostructure alone.

Our experiments open up a new direction for nanophotonics. We see a wide range of potential applications and intriguing opportunities for further studies. On the one hand, switchable light sources on the nanoscale can be used to

controllably excite other structures such as molecules or quantum dots in the vicinity of the nonlinear hot spots. In consequence, our approach would not be limited to the third harmonic wavelength anymore. In combination with waveguiding structures [171, 172], the generated light could be guided away from the switchable plasmonic structure, that way extending also the accessible spatial range. The coherence of the individual emitting centers allows to operate devices such as photonic beam splitters and paves the way towards optical circuits [173, 174, 1]. On the other hand, the concept of tailoring local field distributions is of great interest regarding the development and investigation of extended electronic states [175]. Here, a prominent example is the mapping of the spatial extent of delocalized excitonic states in multichromophoric systems, which is crucial regarding potential light harvesting applications [176, 177]. The near fields around a plasmonic structure offer the possibility to controllably excite and probe certain excitations in such delocalized states. In this context, a well-chosen and optimized switchable structure could provide a versatile and powerful tool to quantify quantum coherence on a nanometer scale.

CONCLUSION AND OUTLOOK

In this thesis, we have studied the optical properties of two prominent material systems in the field of nano-optics, aiming at a deeper understanding of the interaction of these nanoscopic structures with light.

The first part considered the linear optical response of graphene, from a general point of view as well as under the influence of strain. Using optical spectroscopy, one can get further insight into the electronic structure of graphene and the nature of the excited states. This is particularly interesting in the visible to ultraviolet wavelength regime, where graphene's extraordinary band structure exhibits a saddle point. Assuming an excitonic state in the vicinity of the saddle point, a simple Fano model can describe the absorbance spectrum in the visible and ultraviolet regime. The coupling of the discrete excitonic state to the continuum of states from the saddle point down to the Dirac point leads to an asymmetric peak. The measured data is in very good agreement with the model even down to infrared photon energies. We have discussed the properties of the excitonic resonance in graphene and graphene-related systems. Furthermore, we showed that the optical constants of graphene can be extracted from the Fano fit in combination with the Kramers-Kronig relations. After this overview of the general optical properties of graphene, we presented an investigation of the influence of strain on the Fano resonance. Strain causes intriguing effects as it breaks the symmetry in the crystal as well as the band structure, which is predicted to induce profound changes also in the optical spectra. In order to meet the requirements imposed by the experimental conditions, we have tested different substrate materials, especially with regard to the adhesion of the graphene flakes as well as the contrast in the reflectivity spectra. The strain sensitivity of graphene's Raman modes in combination with well-established reference measurement allows to reliably quantify the amount of strain applied to the samples. That way, we have shown that uniaxial strain of up to 1% can reproducibly be applied to graphene sheets on a PMMA substrate using a bending method. Moreover, we have successfully demonstrated that polarization-dependent Raman measurements allow us to determine the crystal orientation relative to the strain direction. While the Raman spectra unambiguously show that strain is applied, no effect in the reflectivity signal

of graphene was observed. Theoretical calculations suggest a splitting of the UV peak, however, the induced changes are subtle for strain values below 1%. Even a careful analysis of the measured spectra with a Fano fitting method in combination with statistical analysis did not reveal any deviations arising from the applied strain. We attribute this to the limited measurement accuracy of our experiment. Although this could be improved by an optimized fabrication process and the use of modulation techniques, the maximum achievable strain is evidently too small to cause distinct effects. As a consequence, other promising approaches such as clamping of graphene to piezoelectric substrates should be considered in future strain experiments. Overall, our investigations prove an astonishing robustness of the Fano resonance in the optical spectrum of graphene towards the influence of strain. This result is particularly interesting in view of potential applications of graphene in optoelectronic devices such as flexible and foldable displays. As strain hardly influences its optical properties, a stable appearance of graphene-based flexible devices can be anticipated.

In the second part, we have presented an investigation of the nonlinear emission properties of plasmonic gold nanostructures. While the linear interaction of plasmons with light is quite well understood, questions remain on the nonlinear behavior. So far, most studies focused on the enhancement of nonlinear processes and their spectral characteristics, whereas our experiments consider the spatial origin of the third-harmonic signals. After a general discussion of light-matter interaction on the nanoscale, we gave an overview of the necessary experimental and calculation methods. The working principle of our experiments was demonstrated at the example of very small rod structures. Here, we have shown that the emission properties of a structure excited at the fundamental plasmon resonance correspond to that of a dipole at an interface. Due to the coherence of the third-harmonic generation process, the light emitted from different, spatially separated rod structures interferes and characteristic patterns can be observed in the far field. In analogy to the classical double slit experiment, we demonstrated that two rods form a nonlinear plasmonic double slit, which allowed us to accurately determine the high fields inside the particles as source of the third-harmonic light. Moreover, higher order plasmonic modes in an elongated rod structure can be exploited to switch the emission properties between different configurations, similar to a light switch on the nanoscale. Varying the wavelength of the excitation light, we observed a transition between a configuration with two spatially separated emission centers and a configuration with dominant emission from the center of the rod. Due to the power dependence of the nonlinear process, the near-fields generated in the vicinity of the particle exhibit the same switching behavior. In addition to established methods based on assemblies of nanoparticles, nanoscale fields

can hence be shaped with similar efficiency using a single nanostructure alone. This approach opens up a new direction for nanophotonics. In combination with other nanoscale structures placed in the nonlinear hot-spots as well as waveguiding structures, the covered wavelength regime and the spatial range can be extended considerably. The coherence properties of the process allow for the development of operating nanophotonic devices such as beam splitters, paving the way towards optical circuits. In addition, the concept of tailoring local field distributions is highly interesting with regard to the investigation of delocalized electronic states found for example in multichromophoric systems. A well-designed switchable structure could provide a versatile and powerful tool to map quantum coherence on a nanometer scale.

A separate investigation of graphene and plasmonic nanostructures is undoubtedly of fundamental research interest. Besides gaining a deeper understanding of their properties, both material systems can be merged, that way adding a new playground to the field of nanophotonics. While graphene combines exceptional electronic conductivity with a stable optical response, plasmonic structures offer wide tunability together with opportunities to shape and enhance optical fields on the nanoscale. First experiments revealed the great potential of graphene–plasmonic hybrid systems for optoelectronic devices or sensor applications. Merging optical and electrical length scales, these hybrid systems moreover set the stage for electrically tunable integrated optical nanocircuits.

BIBLIOGRAPHY

- [1] Koenderink, A. F., Alù, A. & Polman, A. Nanophotonics: Shrinking light-based technology. *Science* **348**, 516–521 (2015).
- [2] Nature Milestones. Photons. URL <http://www.nature.com/milestones/milephotons/timeline.html>. Online (2010).
- [3] Maier, S. A. *Plasmonics: Fundamentals and Applications* (Springer, 2007).
- [4] Liu, N. *et al.* Three-dimensional photonic metamaterials at optical frequencies. *Nature Materials* **7**, 31–37 (2008).
- [5] Zheludev, N. I. & Kivshar, Y. S. From metamaterials to metadevices. *Nature Materials* **11**, 917–924 (2012).
- [6] Novoselov, K. S. *et al.* Electric field effect in atomically thin carbon films. *Science* **306**, 666–669 (2004).
- [7] Novoselov, K. S. *et al.* Two-dimensional atomic crystals. *Proceedings of the National Academy of Science* **102**, 10451–10453 (2005).
- [8] Koppens, F. H. L., Chang, D. E. & García de Abajo, F. J. Graphene plasmonics: A platform for strong light-matter interactions. *Nano Letters* **11**, 3370–3377 (2011).
- [9] Mak, K. F., Ju, L., Wang, F. & Heinz, T. F. Optical spectroscopy of graphene: from the far infrared to the ultraviolet. *Solid State Communications* **152**, 1341–1349 (2012).
- [10] Wang, Q. H., Kalantar-Zadeh, K., Kis, A., Coleman, J. N. & Strano, M. S. Electronics and optoelectronics of two-dimensional transition metal dichalcogenides. *Nature Nanotechnology* **7**, 699–712 (2012).
- [11] Kelly, K. L., Coronado, E., Zhao, L. L. & Schatz, G. C. The optical properties of metal nanoparticles: The influence of size, shape, and dielectric environment. *Journal of Physical Chemistry B* **107**, 668–677 (2003).
- [12] Thongrattanasiri, S., Koppens, F. H. & García de Abajo, F. J. Complete optical absorption in periodically patterned graphene. *Physical Review Letters* **108**, 047401 (2011).

- [13] Prodan, E., Radloff, C., Halas, N. J. & Nordlander, P. A hybridization model for the plasmon resonance of complex nanostructures. *Science* **302**, 419–422 (2003).
- [14] Geim, A. K. & Grigorieva, I. V. Van der Waals heterostructures. *Nature* **499**, 419–425 (2013).
- [15] Geim, A. K. Graphene: Status and prospects. *Science* **324**, 1530–1534 (2009).
- [16] Castro Neto, A. H., Guinea, F., Peres, N. M. R., Novoselov, K. S. & Geim, A. K. The electronic properties of graphene. *Review of Modern Physics* **81**, 109–162 (2009).
- [17] Bonaccorso, F., Sun, Z., Hasan, T. & Ferrari, A. C. Graphene photonics and optoelectronics. *Nature Photonics* **4**, 611–622 (2010).
- [18] Bao, Q. & Loh, K. P. Graphene photonics, plasmonics, and broadband optoelectronic devices. *ACS nano* **6**, 3677–3694 (2012).
- [19] Anker, J. N., Hall, W. P., Nilam, C., Zhao, J. & Van, P. Biosensing with plasmonic nanosensors. *Nature Materials* **7**, 442–453 (2008).
- [20] Liu, N., Tang, M. L., Hentschel, M., Giessen, H. & Alivisatos, A. P. Nanoantenna-enhanced gas sensing in a single tailored nanofocus. *Nature Materials* **10**, 631–636 (2011).
- [21] Soukoulis, C. M., Linden, S. & Wegener, M. Negative refractive index at optical wavelengths. *Science* **315**, 47–50 (2007).
- [22] Shalaev, V. M. Optical negative-index metamaterials. *Nature Photonics* **6**, 41–48 (2007).
- [23] Cai, W., Chettiar, U. K., Kildishev, A. V. & Shalaev, V. M. Optical cloaking with metamaterials. *Nature Photonics* **1**, 224–227 (2007).
- [24] Ergin, T., Stenger, N., Brenner, P., Pendry, J. B. & Wegener, M. Three-dimensional invisibility cloak at optical wavelengths. *Science* **328**, 337–339 (2010).
- [25] Boyd, R. W. *Nonlinear Optics* (Academic Press, 2003), 2nd edn.
- [26] Kauranen, M. & Zayats, A. V. Nonlinear Plasmonics. *Nature Photonics* **6**, 737–748 (2012).
- [27] Echtermeyer, T. J. *et al.* Strong plasmonic enhancement of photovoltage in graphene. *Nature Communications* **2**:458 (2011).

- [28] Ansell, D. *et al.* Hybrid graphene plasmonic waveguide modulators. *Nature Communications* **6**:8846 (2015).
- [29] Kravets, V. G. *et al.* Singular phase nano-optics in plasmonic metamaterials for label-free single-molecule detection. *Nature Materials* **12**, 304–309 (2013).
- [30] Vakil, A. & Engheta, N. Transformation optics using graphene. *Science* **332**, 1291–1294 (2011).
- [31] Chae, D.-H. *et al.* Excitonic Fano resonance in free-standing graphene. *Nano Letters* **11**, 1379–1382 (2011).
- [32] Wolf, D. *et al.* Spectroscopy of graphene at the saddle point. In Binder, R. (ed.) *Optical properties of graphene* (World Scientific, 2016).
- [33] Wolf, D., Schumacher, T. & Lippitz, M. Shaping the nonlinear near field. *Nature Communications* **7**:10361 (2016).
- [34] Geim, A. K. & Novoselov, K. S. The rise of graphene. *Nature Materials* **6**, 183–191 (2007).
- [35] Wallace, P. R. The band theory of graphite. *Physical Review* **71**, 622–634 (1947).
- [36] McClure, J. W. Diamagnetism of graphite. *Physical Review* **104**, 666–671 (1956).
- [37] Slonczewski, J. & Weiss, P. Band structure of graphite. *Physical Review* **109**, 272–279 (1958).
- [38] Peierls, R. E. Quelques propriétés typiques des corps solides. *Annales de l'Institut Henri Poincaré* **5**, 177–222 (1935).
- [39] Landau, L. D. Zur Theorie der Phasenumwandlungen II. *Physikalische Zeitschrift der Sowjetunion* **11**, 26–35 (1937).
- [40] Landau, L. D. & Lifshitz, E. M. *Statistical Physics, Part I* (Pergamon, Oxford, 1980).
- [41] Mermin, N. D. Crystalline order in two dimensions. *Physical Review* **176**, 250–254 (1968).
- [42] Fradkin, E. Critical behavior of disordered degenerate semiconductors. *Physical Review B* **33**, 3263–3268 (1986).
- [43] Meyer, J. C. *et al.* The structure of suspended graphene sheets. *Nature* **446**, 60–63 (2007).

- [44] Lee, C., Wei, X., Kysar, J. W. & Hone, J. Measurement of the elastic properties and intrinsic strength of monolayer graphene. *Science* **321**, 385–388 (2008).
- [45] Balandin, A. A. *et al.* Superior thermal conductivity of single-layer graphene. *Nano Letters* **8**, 902–907 (2008).
- [46] Novoselov, K. S. *et al.* Two-dimensional gas of massless Dirac fermions in graphene. *Nature* **438**, 197–200 (2005).
- [47] Focus issue: graphene applications. *Nature Nanotechnology* **9** (October 2014).
- [48] Bonaccorso, F. *et al.* Graphene, related two-dimensional crystals, and hybrid systems for energy conversion and storage. *Science* **347**, 1246501 (2015).
- [49] Gusynin, V. P., Sharapov, S. G. & Carbotte, J. P. Unusual microwave response of Dirac quasiparticles in graphene. *Physical Review Letters* **96**, 256802 (2006).
- [50] Peres, N. M. R. *Colloquium* : The transport properties of graphene: An introduction. *Review of Modern Physics* **82**, 2673–2700 (2010).
- [51] Ando, T., Zheng, Y. & Suzuura, H. Dynamical conductivity and zero-mode anomaly in honeycomb lattices. *Journal of the Physical Society of Japan* **71**, 1318–1324 (2002).
- [52] Kuzmenko, A. B., van Heumen, E., Carbone, F. & van der Marel, D. Universal optical conductance of graphite. *Physical Review Letters* **100**, 117401 (2008).
- [53] Nair, R. R. *et al.* Fine structure constant defines visual transparency of graphene. *Science* **320**, 1308 (2008).
- [54] Mak, K. F. *et al.* Measurement of the optical conductivity of graphene. *Physical Review Letters* **101**, 196405 (2008).
- [55] Horng, J. *et al.* Drude conductivity of Dirac fermions in graphene. *Physical Review B* **83**, 165113 (2011).
- [56] Ziegler, K. Minimal conductivity of graphene: Nonuniversal values from the Kubo formula. *Physical Review B* **75**, 233407 (2007).
- [57] Hwang, E. H. & Das Sarma, S. Dielectric function, screening, and plasmons in two-dimensional graphene. *Physical Review B* **75**, 205418 (2007).

- [58] Efetov, D. K. & Kim, P. Controlling electron-phonon interactions in graphene at ultrahigh carrier densities. *Physical Review Letters* **105**, 256805 (2010).
- [59] Fei, Z. *et al.* Gate-tuning of graphene plasmons revealed by infrared nano-imaging. *Nature* **487**, 82–85 (2012).
- [60] Chen, J. *et al.* Optical nano-imaging of gate-tunable graphene plasmons. *Nature* **487**, 77–81 (2012).
- [61] Ju, L. *et al.* Graphene plasmonics for tunable terahertz metamaterials. *Nature Nanotechnology* **6**, 630–634 (2011).
- [62] Minkel, J. R. D.I.Y. graphene: How to make one-atom-thick carbon layers with sticky tape. URL <http://www.scientificamerican.com/article/diy-graphene-how-to-make-carbon-layers-with-sticky-tape>. Online (03/20/2008).
- [63] Blake, P. *et al.* Making graphene visible. *Applied Physics Letters* **91**, 063124 (2007).
- [64] Ferrari, A. C. *et al.* Raman spectrum of graphene and graphene layers. *Physical Review Letters* **97**, 187401 (2006).
- [65] Ferrari, A. C. & Basko, D. M. Raman spectroscopy as a versatile tool for studying the properties of graphene. *Nature Nanotechnology* **8**, 235–246 (2013).
- [66] van Hove, L. The occurrence of singularities in the elastic frequency distribution of a crystal. *Physical Review* **56**, 1189–1193 (1953).
- [67] Yu, P. Y. & Cardona, M. *Fundamentals of Semiconductors* (Springer, 2005), 3rd edn.
- [68] Fox, M. A. *Optical Properties of Solids* (Oxford University Press, 2001).
- [69] Wooten, F. *Optical Properties of Solids* (Academic Press, 1972).
- [70] Mak, K. F., Shan, J. & Heinz, T. F. Seeing many-body effects in single- and few-layer graphene: Observation of two-dimensional saddle-point excitons. *Physical Review Letters* **106**, 046401 (2011).
- [71] Kravets, V. G. *et al.* Spectroscopic ellipsometry of graphene and an exciton-shifted van Hove peak in absorption. *Physical Review B* **81**, 155413 (2010).
- [72] Hecht, E. *Optics* (Addison-Wesley, Reading, MA, 1998).

- [73] Yang, L., Deslippe, J., Park, C.-H., Cohen, M. L. & Louie, S. G. Excitonic effects on the optical response of graphene and bilayer graphene. *Physical Review Letters* **103**, 186802 (2009).
- [74] Pétroff, Y. & Balkanski, M. Coulomb effects at saddle-type critical points in CdTe, ZnTe, ZnSe, and HgTe. *Physical Review B* **3**, 3299–3302 (1971).
- [75] Kane, E. O. Coulomb effects at saddle-type critical points. *Physical Review* **180**, 852–858 (1969).
- [76] Ashcroft, N. W. & Mermin, N. D. *Solid State Physics* (Thomas Learning, Toronto, 1976).
- [77] Wang, F. *et al.* Observation of excitons in one-dimensional metallic single-walled carbon nanotubes. *Physical Review Letters* **99**, 227401 (2007).
- [78] Phillips, J. C. Excitons. In Tauc, J. (ed.) *Optical properties of Solids* (Academic Press, London, 1966).
- [79] Fano, U. Effects of configuration interaction on intensities and phase shifts. *Physical Review* **124**, 1866–1878 (1965).
- [80] Mak, K. F. *et al.* Tuning many-body interactions in graphene: The effects of doping on excitons and carrier lifetimes. *Physical Review Letters* **112**, 207401 (2014).
- [81] Wang, F. *et al.* Gate-variable optical transitions in graphene. *Science* **320**, 206–209 (2008).
- [82] Grüneis, A. *et al.* Tight-binding description of the quasiparticle dispersion of graphite and few-layer graphene. *Physical Review B* **78**, 205425 (2008).
- [83] Klintenberg, M., Lebègue, S., Sanyal, B., Fransson, J. & Eriksson, O. Evolving properties of two-dimensional materials: from graphene to graphite. *Journal of Physics: Condensed Matter* **21**, 335502 (2009).
- [84] Taft, E. A. & Philipp, H. R. Optical properties of graphite. *Physical Review* **138**, 197–202 (1965).
- [85] Li, G. *et al.* Observation of van Hove singularities in twisted graphene layers. *Nature Physics* **6**, 109–113 (2009).
- [86] Havener, R. W., Liang, Y., Brown, L., Yang, L. & Park, J. Van Hove singularities and excitonic effects in the optical conductivity of twisted bilayer graphene. *Nano Letters* **14**, 3353–3357 (2014).

- [87] Yang, L., Cohen, M. L. & Louie, S. G. Excitonic effects in the optical spectra of graphene nanoribbons. *Nano Letters* **7**, 3312–3115 (2008).
- [88] Prezzi, D., Varsano, D., Ruini, A., Marini, A. & Molinari, E. Optical properties of graphene nanoribbons: The role of many-body effects. *Physical Review B* **77**, 041404(R) (2008).
- [89] Denk, R. *et al.* Exciton-dominated optical response of ultra-narrow graphene nanoribbons. *Nature Communications* **5**, 4253 (2014).
- [90] Spataru, C. D., Ismail-Beigi, S., Benedict, L. X. & Louie, S. G. Excitonic effects and optical spectra of single-walled carbon nanotubes. *Physical Review Letters* **92**, 077402 (2004).
- [91] Wang, F., Dukovic, G., Brus, L. E. & Heinz, T. F. The optical resonances in carbon nanotubes arise from excitons. *Science* **308**, 838–841 (2005).
- [92] Dresselhaus, M. S., Dresselhaus, G., Saito, R. & Jorio, A. Exciton photophysics of carbon nanotubes. *Annual Reviews of Physical Chemistry* **58**, 719–747 (2007).
- [93] Watanabe, K., Taniguchi, T. & Kanda, H. Direct-bandgap properties and evidence for ultraviolet lasing of hexagonal boron nitride single crystal. *Nature Materials* **3**, 404–409 (2004).
- [94] Arnaud, B., Lebègue, S., Rabiller, P. & Alouani, M. Huge excitonic effects in layered hexagonal boron nitride. *Physical Review Letters* **96**, 026402 (2006).
- [95] Mak, K. F. *et al.* Tightly bound trions in monolayer MoS₂. *Nature Materials* **12**, 207–211 (2013).
- [96] Kramers, H. A. La diffusion de la lumière par les atomes. In *Atti del Congresso Internazionale dei Fisici*, 545–557 (Zanichelli, Bologna, 1927).
- [97] Lucarini, V., Saarinen, J. J., Peiponen, K.-E. & Vartiainen, E. M. *Kramers-Kronig Relations in Optical Materials Research* (Springer, 2005).
- [98] Born, M. & Wolf, E. *Principles of Optics* (Pergamon Press, 1999), 7th edn.
- [99] Weber, J. W., Calado, V. E. & van de Sanden, M. C. M. Optical constants of graphene measured by spectroscopic ellipsometry. *Applied Physics Letters* **97**, 091904 (2010).
- [100] Greenaway, D. L., Harbeke, G., Bassani, F. & Tosatti, E. Anisotropy of the optical constants and the band structure of graphite. *Physical Review* **178**, 1340–1348 (1969).

- [101] Zhan, D. *et al.* Engineering the electronic structure of graphene. *Advanced Materials* **24**, 4055–4069 (2012).
- [102] Gui, G., Li, J. & Zhong, J. Band structure engineering of graphene by strain: First-principles calculations. *Physical Review B* **78**, 075435 (2008).
- [103] Ni, Z. H. *et al.* Uniaxial strain on graphene: Raman spectroscopy study and band-gap opening. *ACS nano* **2**, 2301–2305 (2008).
- [104] Pereira, V. M. & Castro Neto, A. H. Strain engineering of graphene's electronic structure. *Physical Review Letters* **103**, 046801 (2009).
- [105] Choi, S.-M., Jhi, S.-H. & Son, Y.-W. Effects of strain on electronic properties of graphene. *Physical Review B* **81**, 081407 (2010).
- [106] Guinea, F., Katsnelson, M. I. & Geim, A. K. Energy gaps and a zero-field quantum hall effect in graphene by strain engineering. *Nature Physics* **6**, 30–33 (2010).
- [107] Zhu, S., Stroschio, J. A. & Li, T. Programmable extreme pseudomagnetic fields in graphene by a uniaxial stretch. *Physical Review Letters* **115**, 245501 (2015).
- [108] Roy, B. & Juricic, V. Strain-induced time-reversal odd superconductivity in graphene. *Physical Review B* **90**, 041413 (2014).
- [109] Li, X. *et al.* Stretchable and highly sensitive graphene-on-polymer strain sensors. *Scientific Reports* **2**, 870 (2012).
- [110] Bae, S.-H. *et al.* Graphene-based transparent strain sensor. *Carbon* **51**, 236–242 (2013).
- [111] Cambridge Graphene Center and Plastic Logic. First graphene-based flexible display produced. URL <http://www.cam.ac.uk/research/news/first-graphene-based-flexible-display-produced>. Online (09/05/2014).
- [112] University of Cambridge and Novalia. New graphene based inks for high-speed manufacturing of printed electronics. URL <http://www.cam.ac.uk/research/news/new-graphene-based-inks-for-high-speed-manufacturing-of-printed-electronics>. Online (10/19/2015).
- [113] Liang, Y., Huang, S. & Yang, L. Many-electron effects on optical absorption spectra of strained graphene. *Journal of Materials Research* **27**, 403–409 (2012).

- [114] Pereira, V. M., Castro Neto, A. H. & Peres, N. M. R. Tight-binding approach to uniaxial strain in graphene. *Physical Review B* **80**, 045401 (2009).
- [115] Pellegrino, F. M., Angilella, G. G. N. & Pucci, R. Strain effect on the optical conductivity of graphene. *Physical Review B* **81**, 035411 (2010).
- [116] Mohiuddin, T. M. G. *et al.* Uniaxial strain in graphene by Raman spectroscopy: G peak splitting, Grüneisen parameters, and sample orientation. *Physical Review B* **79**, 205433 (2009).
- [117] Herlinger, P. *Optical spectroscopy of graphene* (2012). Diploma thesis.
- [118] Schmidt, U., Hild, S., Ibach, W. & Hollricher, O. Characterization of thin polymer films on the nanometer scale with confocal Raman AFM. *Macromolecular Symposia* **230**, 133–143 (2005).
- [119] Bucciarelli, L. L. *Engineering Mechanics for Structures, Chapter 7* (Dover, 2004).
- [120] Nelson, G. J., Matthewson, M. J. & Lin, B. A novel four-point bend test for strength measurements of optical fibers and thin beams – Part I: Bending analysis. *Journal of Lightwave Technology* **14**, 555–563 (1996).
- [121] Polyanskiy, M. N. Refractive index database. URL <http://refractiveindex.info>. Online (accessed 2012).
- [122] Schneider, F., Draheim, J., Kamberger, R. & Wallrabe, U. Process and material properties of polymethylsiloxane (PMDS) for optical MEMS. *Sensors and Actuators A: Physical* **151**, 95–99 (2009).
- [123] Huang, M., Yan, H., Chen, C., Heinz, T. F. & Hone, J. Phonon softening and crystallographic orientation of strained graphene studied by Raman spectroscopy. *Proceedings of the National Academy of Sciences* **106**, 7304–7308 (2009).
- [124] Grimvall, G. *Thermophysical Properties of Materials* (Holland, 1986).
- [125] Präzisions Glas & Optik. BK7 data sheet. URL <http://www.pgo-online.com/intl/katalog/BK7.html>. Online (accessed 2015).
- [126] Mark, J. E. *Polymer Data Handbook* (Oxford University Press, 1999).
- [127] Rohlfing, M. & Louie, S. G. Electron-hole excitations and optical spectra from first principles. *Physical Review B* **62**, 4927–4944 (2000).
- [128] Pereira, V. M., Ribeiro, R. M., Peres, N. M. R. & Castro Neto, A. H. Optical properties of strained graphene. *Europhysics Letters* **92**, 67001 (2010).

- [129] Levy, N. *et al.* Strain-induced pseudo-magnetic fields greater than 300 Tesla in graphene nanobubbles. *Science* **329**, 544–547 (2010).
- [130] Zabel, J. *et al.* Raman spectroscopy of graphene and bilayer under biaxial strain: Bubbles and balloons. *Nano Letters* **12**, 617–621 (2012).
- [131] Ding, F. *et al.* Stretchable graphene: A close look at fundamental parameters through biaxial straining. *Nano Letters* **10**, 3453–3458 (2010).
- [132] Shioya, H., Craciun, M. F., Russo, S., Yamamoto, M. & Tarucha, S. Straining graphene using thin film shrinkage methods. *Nano Letters* **14**, 1158–1163 (2014).
- [133] Lal, S., Link, S. & Halas, N. J. Nano-optics from sensing to waveguiding. *Nature Photonics* **1**, 641–648 (2007).
- [134] Jackson, J. D. *Classical Electrodynamics* (John Wiley & Sons, 1999), 3rd edn.
- [135] Ullrich, D. *Optimization of optical nanoantennas for nonlinear spectroscopy* (2011). Diploma thesis.
- [136] Johnson, P. B. & Christy, R. W. Optical constants of the noble metals. *Physical Review B* **6**, 4370–4379 (1972).
- [137] Zeman, E. J. & Schatz, G. C. An accurate electromagnetic theory study of surface enhancement factors for silver, gold, copper, lithium, sodium, aluminum, gallium, indium, zinc, and cadmium. *Journal of Physical Chemistry* **91**, 634–643 (1987).
- [138] Neumann, F. E. *Vorlesungen über die Theorie der Elastizität der festen Körper und des Lichtäthers* (B. G. Teubner Verlag, 1885).
- [139] Miller, R. C. Optical second harmonic generation in piezoelectric crystals. *Applied Physics Letters* **5**, 17–19 (1964).
- [140] Mühlischlegel, P., Eisler, H.-J., Martin, O. J. F., Hecht, B. & Pohl, D. W. Resonant optical antennas. *Science* **308**, 1607–1609F (2005).
- [141] Novotny, L. & van Hulst, N. Antennas for light. *Nature Photonics* **5**, 83–90 (2011).
- [142] Schumacher, T. *et al.* Nanoantenna-enhanced ultrafast nonlinear spectroscopy of a single gold nanoparticle. *Nature Communications* **2**:333 (2011).
- [143] Scholl, J. A., Koh, A. L. & Dionne, J. A. Quantum plasmon resonances of individual metallic nanoparticles. *Nature* **483**, 421–428 (2012).

- [144] Bohren, C. F. & Huffman, D. R. *Absorption and Scattering of Light by Small Particles* (Wiley-VCH, 1983).
- [145] Mie, G. Beiträge zur Optik trüber Medien, speziell kolloidaler Metallösungen. *Annalen der Physik* **330**, 377–445 (1908).
- [146] Taminiau, T. H., Stefani, F. D. & van Hulst, N. F. Optical nanorod antennas modeled as cavities for dipolar emitters: Evolution of sub- and super-radiant modes. *Nano Letters* **11**, 1020–1024 (2011).
- [147] Dorfmueller, J. *et al.* Plasmonic nanowire antennas: experiment, simulation, and theory. *Nano Letters* **10**, 3506–3603 (2010).
- [148] Novotny, L. & Hecht, B. *Principles of nano-optics* (Cambridge University Press, 2012), 2nd edn.
- [149] Utikal, T. *et al.* Towards the origin of the nonlinear response in hybrid plasmonic systems. *Physical Review Letters* **106**, 133901 (2011).
- [150] Metzger, B., Hentschel, M., Lippitz, M. & Giessen, H. Third-harmonic spectroscopy and modeling of the nonlinear response of plasmonic nanoantennas. *Optics Letters* **37**, 4741–3 (2012).
- [151] Hentschel, M., Utikal, T., Giessen, H. & Lippitz, M. Quantitative modeling of the third harmonic emission spectrum of plasmonic nanoantennas. *Nano Letters* **12**, 3778–3782 (2012).
- [152] Harutyunyan, H., Volpe, G., Quidant, R. & Novotny, L. Enhancing the nonlinear optical response using multifrequency gold-nanowire antennas. *Physical Review Letters* **108**, 217403 (2012).
- [153] Aouani, H., Rahmani, M., Navarro-Cía, M. & Maier, S. A. Third-harmonic-upconversion enhancement from a single semiconductor nanoparticle coupled to a plasmonic antenna. *Nature Nanotechnology* **9**, 1–5 (2014).
- [154] Lieb, M. A., Zavislan, J. M. & Novotny, L. Single-molecule orientations determined by direct emission pattern imaging. *J. Opt. Soc. Am. B* **21**, 1210–1215 (2004).
- [155] Schumacher, T. *Optical nanoantennas for ultrafast nonlinear spectroscopy of individual nanosystems* (2014). Dissertation.
- [156] Metzger, B., Schumacher, T., Hentschel, M., Lippitz, M. & Giessen, H. Third harmonic mechanism in complex plasmonic Fano structures. *ACS Photonics* 471–476 (2014).

- [157] Atwater, H. A. & Polman, A. Plasmonics for improved photovoltaic devices. *Nature Materials* **9**, 205–213 (2010).
- [158] Hanke, T. *et al.* Efficient nonlinear light emission of single gold optical antennas driven by few-cycle near-infrared pulses. *Physical Review Letters* **103**, 257404 (2009).
- [159] Schuller, J. A. *et al.* Plasmonics for extreme light concentration and manipulation. *Nature Materials* **9**, 193–204 (2010).
- [160] Luk'yanchuk, B. *et al.* The Fano resonance in plasmonic nanostructures and metamaterials. *Nature Materials* **9**, 707–715 (2010).
- [161] Valev, V. K. *et al.* Asymmetrical optical second-harmonic generation from chiral G-shaped gold nanostructures. *Physical Review Letters* **104**, 127401 (2010).
- [162] Niesler, F. B. P. *et al.* Second-harmonic generation from split-ring resonators on a GaAs substrate. *Optics Letters* **34**, 1997–1999 (2009).
- [163] Canfield, B. K., Kujala, S., Jefimovs, K. & Kauranen, M. Linear and nonlinear optical responses influenced by broken symmetry in an array of gold nanoparticles. *Optics Express* **12**, 419–423 (2004).
- [164] Canfield, B. K. *et al.* A macroscopic formalism to describe the second-order nonlinear optical response of nanostructures. *Journal of Optics A: Pure and Applied Optics* **8**, S278–S284 (2006).
- [165] Hentschel, M. *Complex 2D & 3D plasmonic nanostructures: Fano resonances, chirality, and nonlinearities* (2013). Dissertation.
- [166] Farrer, R. A., Butterfield, F. L., Chen, V. W. & Fourkas, J. T. Highly efficient multiphoton-absorption-induced luminescence from gold nanoparticles. *Nano Letters* **5**, 1139–1142 (2005).
- [167] Lippitz, M., Dijk, M. A. & Orrit, M. Third-harmonic generation from single gold nanoparticles. *Nano Letters* **5**, 799–802 (2005).
- [168] Knittel, V. *et al.* Nonlinear photoluminescence spectrum of single gold nanostructures. *ACS nano* **9**, 894–900 (2014).
- [169] Goodman, J. W. *Introduction to Fourier Optics* (McGraw-Hill, 2005), 3rd edn.
- [170] Drégely, D. *et al.* Imaging and steering an optical wireless nanoantenna link. *Nature Communications* **5**, 4354 (2014).

- [171] Barnes, W. L., Dereux, A. & Ebbesen, T. W. Surface plasmon subwavelength optics. *Nature* **424**, 824–830 (2003).
- [172] Gramotnev, D. K. & Bozhevolnyi, S. I. Plasmonics beyond the diffraction limit. *Nature Photonics* **4**, 83–91 (2010).
- [173] Ozbay, E. Plasmonics: Merging photonics and electronics at nanoscale dimensions. *Science* **311**, 189–193 (2006).
- [174] Engheta, N. Circuits with light at nanoscales: optical nanocircuits inspired by metamaterials. *Science* **317**, 1698–1702 (2007).
- [175] Dubin, F. *et al.* Macroscopic coherence of a single exciton state in a polydiacetylene organic quantum wire. *Nature Physics* **2**, 32–35 (2006).
- [176] Hildner, R., Brinks, D., Nieder, J. B., Cogdell, R. J. & van Hulst, N. Quantum coherent energy transfer over varying pathways in single light-harvesting complexes. *Science* **340**, 1448–1451 (2013).
- [177] Hädler, A. T. *et al.* Long-range energy transport in single supramolecular nanofibres at room temperature. *Nature* **523**, 196–199 (2015).

ERKLÄRUNG

Hiermit versichere ich an Eides statt, dass ich die vorliegende Arbeit selbstständig verfasst und keine anderen als die von mir angegebenen Quellen und Hilfsmittel verwendet habe.

Weiterhin erkläre ich, dass ich die Hilfe von gewerblichen Promotionsberatern bzw. -vermittlern oder ähnlichen Dienstleistern weder bisher in Anspruch genommen habe, noch künftig in Anspruch nehmen werde.

Zusätzlich erkläre ich hiermit, dass ich keinerlei frühere Promotionsversuche unternommen habe.

Bayreuth, März 2016

Daniela Wolf

CURRICULUM VITAE

PERSONAL INFORMATION

Name Daniela Christiane Wolf (née Ullrich)
Date of birth April 30, 1986
in Nürtingen, Germany
Address Beuthener Str. 14
70374 Stuttgart, Germany
Phone +49 711 25298091
Email daniela.wolf@uni-bayreuth.de

EDUCATION

since 11/2011 Ph.D. student in the group of Prof. Markus Lippitz,
University of Stuttgart, Max Planck Institute for Solid
State Research Stuttgart, and University of Bayreuth
09/2011 Diploma in Physics
09/2010–09/2011 Diploma Thesis in the group of Prof. Markus Lippitz
on "Optimization of Optical Nanoantennas
for Nonlinear Spectroscopy"
11/2009–07/2010 Research Assistant in the group of Prof. Markus Lippitz
08/2008–05/2009 Studies of physics at the University of Massachusetts,
Amherst (USA)
10/2005–09/2011 Studies of physics at the University of Stuttgart
Specialized courses in nuclear and elementary particle
physics, environmental and atmospheric physics
06/2005 Max-Planck-Gymnasium Nürtingen, Abitur

ACKNOWLEDGEMENTS

Although a PhD thesis is written by a single author, there are many people who contribute to its success. I would like to thank the following persons without whom this work would not have been possible:

- Prof. Markus Lippitz for giving me the opportunity to work in his group as well as for his continuous support, advice, insight and ideas
- my examination committee Prof. Stephan Kümmel, Prof. Jürgen Köhler, and apl. Prof. Lothar Kador for the interest in my work
- Thorsten Schumacher for sharing his knowledge and ideas with me and for the excellent team work
- Prof. Harald Giessen and all members of the 4th Physics Institute of the University of Stuttgart for the good collaboration
- Jurgen Smet and his team for the collaboration and support regarding the graphene project
- Klas Lindfors and Mario Hentschel for introducing me to nanofabrication and sharing their knowledge
- Dr. Jürgen Weis for granting me access to the cleanroom at the MPI, also after moving to Bayreuth, as well as the cleanroom team for their assistance
- Tristan Kolb, Martina Heider, Dr. Beate Förster, Klaus Müller, Frank Schirmer, and Werner Reichstein for help and support with sample fabrication at the University of Bayreuth
- all members of the Junior Research Group Ultrafast Nanooptics at the MPI for the nice and warm working atmosphere: Gelon Albrecht, Daniel Dregely, Mario Hentschel, Patrick Herlinger, Kai Kratzer, Klas Lindfors, Stefanie Neutzner, Markus Pfeiffer, Tobias Utikal, Siegfried Weisenburger, Christian Wolpert, Xiaofei Wu, Hongyi Zhang
- especially my office mates Matthias Brandstetter, Christian Dicken, and Thorsten Schumacher for the fun and the great time in Stuttgart and Bayreuth as well as for all scientific and non-scientific discussions

- all my coworkers at the Chair for Experimental Physics III in Bayreuth: Marvin Berger, Ping Jiang, Jessica Koller, Marco Klement, Laura Meißner, Alexander Neufeld, Julian Obermeier, Gerhard Schäfer, Christian Schörner, Christoph Soldner, Daniel Sommermann, Johannes Weißert, our technicians Patrick Knödler and Robert Weiner, as well as our secretaries Waltraud Rödel and Evi Barthmann
- my family and Stefan for their constant support through all ups and downs

COLOPHON

This document was typeset using the typographical look-and-feel classicthesis developed by André Miede. The style was inspired by Robert Bringhurst's seminal book on typography "*The Elements of Typographic Style*". classicthesis is available via CTAN.